

Nonequilibrium Radiative Heating Prediction Method for Aeroassist Flowfields with Coupling to Flowfield Solvers

by
Lin C. Hartung

A Thesis Submitted to the Graduate Faculty
of North Carolina State University
in Partial Fulfillment of the
Requirements for the Degree of
Doctor of Philosophy
Major Subject: Aerospace Engineering

Department of Mechanical and Aerospace Engineering

Raleigh

1991

Nonequilibrium Radiative Heating Prediction Method for Aeroassist Flowfields with Coupling to Flowfield Solvers

by
Lin C. Hartung

A Thesis Submitted to the Graduate Faculty
of North Carolina State University
in Partial Fulfillment of the
Requirements for the Degree of
Doctor of Philosophy
Major Subject: Aerospace Engineering

Department of Mechanical and Aerospace Engineering

Raleigh

1991

Approved by:

Chairman of Advisory Committee

Abstract

Hartung, Lin C. Nonequilibrium Radiative Heating Prediction Method for Aeroassist Flowfields with Coupling to Flowfield Solvers (Under the direction of Dr. F. R. DeJarnette)

A method for predicting radiation absorption and emission coefficients in thermochemical nonequilibrium flows is developed. The method is called LORAN: the Langley Optimized RAdiative Nonequilibrium code. It applies the smeared band approximation for molecular radiation to produce moderately detailed results and is intended to fill the gap between detailed but costly prediction methods, and very fast but highly approximate methods. The optimization of the method to provide efficient solutions allowing coupling to flowfield solvers is discussed. Representative results are obtained and compared to previous nonequilibrium radiation methods, as well as to ground- and flight-measured data. Reasonable agreement is found in all cases. A multi-dimensional radiative transport method is also developed for axisymmetric flows. Its predictions for wall radiative flux are 20 to 25 percent lower than those of the tangent slab transport method, as expected, though additional investigation of the symmetry and outflow boundary conditions is indicated. The method has been applied to the peak heating condition of the Aeroassist Flight Experiment (AFE) trajectory, with results comparable to predictions from other methods. The LORAN method has also been applied in conjunction with the computational fluid dynamics (CFD) code LAURA to study the sensitivity of the radiative heating prediction to various models used in nonequilibrium CFD. This study suggests that radiation measurements can provide diagnostic information about the detailed processes occurring in a nonequilibrium flowfield because radiation phenomena are very sensitive to these processes.

Acknowledgments

The assistance and suggestions of Dr. Hassan A. Hassan in developing the radiative transport solution method were most valuable, while the comments of Dr. Fred DeJarnette helped me to maintain my perspective on the problem at hand.

Thanks go to Drs. Peter Gnoffo and Robert Mitcheltree, of NASA Langley Research Center, for their patient answers to my many questions regarding numerical methods. In addition, Dr. Mitcheltree's assistance in coupling the LAURA and LORAN solution methods was invaluable. The support of my management at NASA Langley during this period of research was crucial to my success. Flowfield solutions for this study were provided by Robert Mitcheltree, Peter Gnoffo and Bob Greendyke. Special thanks go to Tad Guy for applying his considerable computer wizardry (and patience) to the sundry bugs and problems I encountered.

I would also like to thank Dr. Ann Carlson for her support and her example. I greatly appreciated the encouragement of soon-to-be Drs. Neil Cheatwood, Chris Riley and Tom Kashangaki. In addition, I want to acknowledge the many friends, acquaintances and family members who were interested enough to ask again and again over a period of years about the progress of my efforts.

The support and encouragement of my entire family, as well as some friendly competition with my brother Walter, was very valuable in helping me complete this work as quickly as possible.

Summary

When a spacecraft enters the atmosphere of a planet, it pushes some of the gas particles it encounters with it. As the atmosphere becomes thicker, the gas particles in this “shock layer” begin to collide with each other. This converts some of the energy of motion that these particles gained from the spacecraft into internal motions of the electrons and atoms inside the gas particles. When the gas density is high enough, this process reaches an equilibrium state and can be simply described. When the gas density is not so high, the transfer of energy proceeds slowly and remains out of equilibrium.

The internal changes in electron and atom energy can be accompanied by a photon of radiative energy being emitted or absorbed by a gas particle. Predicting the number and energy of these photons in a nonequilibrium gas is the problem to be solved here. These photons travel through the gas at the speed of light and may end up depositing their energy on the spacecraft surface, thus adding to the heating which exists because of gas friction. If enough energy is deposited the surface may begin to melt or burn. Heating predictions allow the spacecraft heatshield to be designed accordingly.

Table of Contents

| | |
|--|------------|
| List of Figures | vii |
| List of Tables | x |
| Nomenclature | xii |
| 1 Introduction | 1 |
| 2 Historical Review | 5 |
| 2.1 Topical and Literature Survey | 5 |
| 2.1.1 Nonequilibrium Absorption and Emission | 5 |
| 2.1.2 Nonequilibrium Excitation Processes | 8 |
| 2.1.3 Radiative Transport | 9 |
| 2.2 Computer Code Survey | 12 |
| 2.2.1 Equilibrium Radiation Codes | 12 |
| 2.2.2 Nonequilibrium Radiation Codes | 14 |
| 2.3 Survey of Experimental Results | 15 |
| 2.3.1 Ground-Based Data | 15 |
| 2.3.2 Flight Data | 16 |
| 3 Radiation Theory | 17 |

| | | |
|----------|--------------------------------------|-----------|
| 3.1 | Absorption | 17 |
| 3.1.1 | Atomic Mechanisms | 17 |
| 3.1.2 | Molecular Mechanisms | 22 |
| 3.2 | Emission | 34 |
| 3.2.1 | Atomic Mechanisms | 35 |
| 3.2.2 | Molecular Mechanisms | 38 |
| 3.3 | Induced Emission | 40 |
| 4 | Transport Theory | 42 |
| 4.1 | Flowfield Coupling | 43 |
| 4.2 | Plane-Parallel Medium | 43 |
| 4.2.1 | Transparent Gas | 44 |
| 4.2.2 | Absorbing Gas | 45 |
| 4.3 | Multi-Dimensional Medium | 47 |
| 5 | Implementation | 52 |
| 5.1 | Coding | 52 |
| 5.1.1 | Initial Setup | 52 |
| 5.1.2 | Nonequilibrium Excitation | 58 |
| 5.1.3 | Radiation Properties | 59 |
| 5.1.4 | Radiative Transport | 63 |
| 5.2 | Computational Optimization | 66 |
| 5.2.1 | Radiation Calculation | 67 |

| | | |
|----------|---|------------|
| 5.2.2 | Excitation Calculation | 68 |
| 5.2.3 | Radiation Subgrid | 70 |
| 5.3 | Flowfield Coupling | 73 |
| 6 | Results and Discussion | 76 |
| 6.1 | Comparison to Experiment | 76 |
| 6.1.1 | Ground-Based Data: AVCO Shock Tube | 76 |
| 6.1.2 | Flight Data: Project FIRE | 77 |
| 6.2 | Nonequilibrium Test Cases | 85 |
| 6.2.1 | Mars Return | 85 |
| 6.2.2 | Aeroassist Flight Experiment | 90 |
| 7 | Flowfield Model Studies | 95 |
| 7.1 | Baseline Models | 96 |
| 7.2 | Energy Relaxation | 97 |
| 7.2.1 | Dissociation Temperature | 98 |
| 7.2.2 | Vibrational-Translational Energy Exchange | 99 |
| 7.2.3 | Energy Exchange in Dissociation | 104 |
| 7.3 | Spectral Radiation Comparison | 108 |
| 7.4 | Nonequilibrium Chemistry | 112 |
| 7.5 | Nonequilibrium Temperature | 115 |
| 8 | Conclusions | 118 |

| | | |
|----------|---|------------|
| 8.1 | Accomplishments | 118 |
| 8.2 | Future Work | 119 |
| | References | 121 |
| A | Gaussian Units | 135 |
| B | Finite Volume Formulation of Radiative Transport | 136 |
| B.1 | Finite Volume Development | 136 |
| B.2 | Boundary Conditions | 147 |
| B.2.1 | Axis of Symmetry Boundary | 148 |
| B.2.2 | Freestream Boundary | 151 |
| B.2.3 | Outflow Boundary | 153 |
| B.2.4 | Wall Boundary | 154 |
| B.2.5 | Radiative Heat Flux to Wall | 155 |
| B.3 | Numerics and Convergence | 155 |
| B.3.1 | Convergence Criterion | 155 |
| B.3.2 | Selection of Relaxation Parameter | 157 |

List of Figures

| | | |
|-----|--|----|
| 3.1 | Distribution of Spectral Points for an Atomic Line | 18 |
| 4.1 | Shock Layer Geometry for Plane-Parallel Approximation | 44 |
| 5.1 | Example of Spectrum Optimization for Bound-Free Continuum | 55 |
| 5.2 | Example of Spectrum Optimization for a Vibrational Band | 57 |
| 5.3 | Occurrence of Negative κ'_ν in a Test Flowfield | 66 |
| 5.4 | Nonequilibrium Population of Excited States of O for Negative κ'_ν | 67 |
| 5.5 | Example of Radiation Subgrid Selection | 71 |
| 5.6 | Patchwork Grid Resulting from Application of Subgrid Algorithm Along Each Normal Line | 73 |
| 6.1 | Calculated Spectrum for the Peak Radiation Point of the AVCO Ex- periment | 78 |
| 6.2 | Measured Spectrum and NEQAIR Prediction for the Peak Radiation Point of the AVCO Experiment | 78 |
| 6.3 | Predicted FIRE II Stagnation Line Temperature Profiles - 1631 sec | 81 |
| 6.4 | Predicted FIRE II Stagnation Line Temperature Profiles - 1634 sec | 81 |
| 6.5 | Predicted FIRE II Stagnation Line Temperature Profiles - 1637.5 sec | 82 |
| 6.6 | Emission Profiles for FIRE II at 1634 sec with Comparison to NEQAIR | 83 |
| 6.7 | Emission Profiles for FIRE II at 1637.5 sec with Comparison to NEQAIR | 84 |

| | | |
|------|---|-----|
| 6.8 | Spectral Variation of Stagnation Point Radiative Heat Transfer for FIRE II | 86 |
| 6.9 | Spectral Variation of Stagnation Point Nitrogen Radiation for FIRE II | 86 |
| 6.10 | Wall Radiative Flux for Mars Return Case | 88 |
| 6.11 | Radiative Flux Divergence for Mars Return Case with Tangent Slab Transport | 89 |
| 6.12 | Radiative Flux Divergence for Mars Return Case with MDA Transport | 89 |
| 6.13 | Wall Radiative Flux for AFE | 91 |
| 6.14 | Radiative Flux Divergence for AFE with Tangent Slab Transport . . | 93 |
| 6.15 | Radiative Flux Divergence for AFE with MDA Transport | 93 |
| 6.16 | Spectral Distribution of AFE Wall Radiative Flux | 94 |
| 7.1 | Effect of T_d Models on Molecular Dissociation - 1631 sec | 100 |
| 7.2 | Effect of T_d Models on Temperature Profiles - 1631 sec | 101 |
| 7.3 | Effect of T_d Models on Radiative Emission Profiles - 1631 sec | 101 |
| 7.4 | Effect of σ_v Models on Temperature Profiles - 1631 sec | 103 |
| 7.5 | Effect of σ_v Models on Radiative Emission Profiles - 1631 sec | 104 |
| 7.6 | Effect of ΔE_v Models on Temperature Profiles - 1634 sec | 106 |
| 7.7 | Effect of ΔE_v Models on Radiative Emission Profiles - 1634 sec . . . | 107 |
| 7.8 | Predicted Radiation Spectrum - 1631 sec | 110 |
| 7.9 | Measured Radiation Spectrum - 1631.3 sec | 110 |
| 7.10 | Predicted Radiation Spectra - 1634 sec | 111 |

| | |
|---|---------|
| 7.11 Measured Radiation Spectrum - 1634.43 sec | 111 |
| 7.12 Predicted Radiation Spectra - 1637.5 sec | 113 |
| 7.13 Measured Radiation Spectrum - 1636.43 sec | 113 |
| 7.14 Effect of Chemical Kinetics Model on Temperature Profiles - 1634 sec | 114 |
| B.1 Variation of $\bar{\kappa}_\nu$ and \bar{j}_ν for a Mars Return Flowfield | 139 |
| B.2 Essential Features of Axisymmetric Radiation Grid | 148 |
| B.3 Top View of Axisymmetric Radiation Grid | 149 |
| B.4 Typical Convergence History for MDA Solution | 157 |

List of Tables

| | | |
|-----|--|-----|
| 5.1 | Computational Optimization - FIRE II at 1631 sec | 69 |
| 5.2 | Computational Optimization - FIRE II at 1634 sec | 69 |
| 5.3 | Computational Optimization - FIRE II at 1637.5 sec | 69 |
| 5.4 | Effect of Radiation Subgrid Algorithm | 72 |
| 6.1 | Selected FIRE II Flight Conditions | 80 |
| 6.2 | Radiative Heat Flux Predictions for FIRE II | 85 |
| 7.1 | Effect of Energy Exchange Models for FIRE II at 1631 sec | 116 |
| 7.2 | Effect of Energy Exchange Models for FIRE II at 1634 sec | 116 |
| 7.3 | Effect of Energy Exchange Models for FIRE II at 1637.5 sec | 117 |

Nomenclature

| | |
|----------|---|
| a | Grid cell surface area (cm ²) |
| a_0 | Bohr radius (cm) |
| A | Transition probability (/sec) |
| AFE | Aeroassist Flight Experiment |
| ASTV | Aeroassist Space Transfer Vehicle |
| b | Normalized line shape (sec) |
| B_{lu} | Einstein coefficient for absorption |
| B | Rotational constant (eV) |
| B_ν | Radiosity (W/cm ² -sec ⁻¹) |
| c | Speed of light (cm/sec) |
| CFD | Computational Fluid Dynamics |
| d | Coefficients in Gauss-Seidel formulation |
| D_v | 2nd rotational constant (eV) |
| D_{el} | Matrix element (statcoul-cm) |
| D | Dissociation energy from ground state (eV) |
| DSMC | Direct Simulation Monte Carlo |
| e | Electron charge (statcoul) |
| E | Energy or energy level (eV) |
| f | Distribution function |
| f_{lu} | Oscillator strength for line transitions |

| | |
|-----------|---|
| F | Normalized line shape |
| g | Degeneracy |
| G_ν | Incident spectral radiative intensity (W/cm ² -sec ⁻¹) |
| h | Planck's constant (eV-sec or erg-sec) |
| $h\nu$ | Energy (eV) |
| I | Ionization potential of ground state (eV) |
| I_ν | Radiative intensity (W/cm ² -sec ⁻¹ -ster) |
| j_ν^e | Emission coefficient (W/cm ³ -sec ⁻¹ -ster) |
| J^e | Total line emission |
| J | Rotational quantum number |
| \hat{J} | Jacobian for transformation from physical to computational coordinates |
| k | Boltzmann's constant (eV/K or erg/K) |
| L | Local error in Gauss-Seidel iteration |
| LAURA | Langley Aerothermodynamic Upwind Relaxation Algorithm |
| LORAN | Langley Optimized RAdiative Nonequilibrium |
| m | Mass (g) |
| MDA | Modified Differential Approximation |
| n | Principal quantum number |
| \hat{n} | Surface unit normal |
| N | Number density (cm ⁻³) |
| NASA | National Aeronautics and Space Administration |

| | |
|-------------|--|
| NBS | National Bureau of Standards |
| p | Rotational transition probability |
| \hat{p} | Scattering phase function |
| q | Franck-Condon factor |
| \vec{q}_R | Radiative flux (W/cm ²) |
| Q | Partition function |
| QSS | Quasi-steady-state |
| r | Relaxation parameter |
| \vec{r} | Position vector |
| RIFSP | Radiating Inviscid Flow Stagnation Point |
| s | Path variable (cm) |
| S | Radiative source function (W/cm ² -sec ⁻¹ -ster) |
| t | Time (sec) |
| T | Temperature (K) |
| v | Speed (cm/sec) |
| v | Vibrational quantum number |
| V | Volume of grid cell (cm ³) |
| W | Weighting factor in subgrid algorithm |
| x | Cartesian coordinate (cm) |
| x_e | Spectroscopic constant (eV) |
| y | Cartesian coordinate (cm) |

| | |
|---------------|--|
| y_e | Spectroscopic constant (eV) |
| z | Cartesian coordinate (cm) |
| z_e | Spectroscopic constant (eV) |
| Z | Ion charge number |
| Z_k | Radiation subgrid weighting function |
| α | Correction to rotational constant (eV) |
| β | Correction to 2nd rotational constant (eV) |
| γ | Line (half) half width (1/sec) |
| γ^s | Scattering coefficient (1/cm) |
| $,$ | Computational variable for incident intensity |
| Δr | Normal distance from wall to center of first grid cell (cm) |
| ε | Surface emissivity |
| ζ | Third computational coordinate direction |
| η | Second computational coordinate direction |
| θ | Angle subtended by axisymmetric grid (radians) |
| κ | Absorption coefficient (1/cm) |
| κ' | Absorption coefficient corrected for induced emission (1/cm) |
| λ | Wavelength (cm) |
| ν | Frequency (1/sec) |
| ξ | First computational coordinate direction |
| σ | Cross-section (cm ²) |

| | |
|----------------|-----------------------------------|
| Σ | Molecular state designator |
| τ | Optical variable |
| τ_v | Vibrational relaxation time (sec) |
| ω | Solid angle (radians) |
| ω_e | Spectroscopic constant (eV) |
| $\hat{\Omega}$ | Direction vector |

Subscripts:

| | |
|------|----------------------------------|
| a | perturbing atoms |
| A | lower electronic state |
| B | upper electronic state |
| c | capture |
| CL | line center |
| d | dissociation |
| e | electron |
| el | electronic |
| ex | excitation |
| f | freestream cell face |
| F | freestream cell center |
| i | grid index in x-direction |
| I | cell center index in x-direction |
| j | grid index in y-direction |

| | |
|------------|---------------------------------------|
| J | cell center index in y-direction |
| J^u, J^l | rotational quantum number |
| k | grid index in z-direction |
| K | cell center index in z-direction |
| l | lower state of radiative transition |
| m | medium |
| n | index of electronic level |
| p | Planck |
| P | $\Delta J = -1$ rotational transition |
| Q | $\Delta J = 0$ rotational transition |
| r | rotational |
| R | $\Delta J = 1$ rotational transition |
| R | radiative |
| s | species index |
| t | translational |
| tot | total |
| u | upper state of radiative transition |
| v | vibrational |
| w | wall |
| x | x component or derivative |
| y | y component or derivative |

| | |
|-------|---------------------------|
| z | z component or derivative |
| 0 | reference |
| ν | frequency |
| + | ion |

Superscripts:

| | |
|------|---------------------------------|
| B | upper electronic state |
| D | Doppler |
| e | emission |
| J | rotational quantum number |
| MW | Millikan-White |
| n | index of time step in iteration |
| P | Park |
| R | resonance |
| s | scattering |
| S | Stark |
| v | vibrational quantum number |
| * | photoionization threshold |
| ' | integration dummy variable |
| — | negative y direction |
| + | positive y direction |

1 Introduction

A significant portion of the heating experienced by a blunt spacecraft encountering a planetary atmosphere at high speed can be due to radiation. The radiative heating can therefore be a strong driver on the design of a spacecraft heatshield. In the past, most spacecraft encountering planetary atmospheres were on entry trajectories descending rapidly into the dense lower layers of the atmosphere. The heat load they experienced could therefore be accurately calculated using equilibrium methods. Mission scenarios currently under study, such as Aeroassist Space Transfer Vehicles (ASTV) designed to rendez-vous with the International Space Station Freedom, and aerobrakes used for orbit insertion in planetary exploration, present a different situation. Walberg [1] provides a summary of such missions. These vehicles use the upper atmosphere to obtain the necessary velocity change for orbit transfer and may spend significant amounts of time in low density regions where nonequilibrium conditions prevail.

Numerous Computational Fluid Dynamics (CFD) codes are being developed to solve the Navier Stokes equations for this nonequilibrium regime. These codes predict the convective heating rates for ASTVs. A few studies of the nonequilibrium radiative heating problem have also been made [2, 3, 4]. Nelson [5] discusses some of the problems and preliminary results from nonequilibrium radiative heating analyses. However there remains a need for a relatively fast and accurate method which can

be coupled to a flowfield solution in cases of heavy radiation, or used uncoupled in cases with less significant radiation. There has also been some evidence in recent years [4] that the one-dimensional tangent slab approximation, which is standard in computing radiative transport, may not be adequate for some of the vehicle shapes and applications under consideration. It will certainly not suffice to compute radiative transport in the wake region of such vehicles where payloads will generally be located.

The objective of the present work is to develop an accurate, efficient method for calculating radiative heat transfer under nonequilibrium conditions, to initiate the development of a multi-dimensional transport algorithm for such radiative transfer, and to present some initial results.

To develop a method for calculating nonequilibrium radiation, the necessary radiation property models were first derived for a nonequilibrium gas. In nonequilibrium, expressions for both absorption and emission are required since the equilibrium relationship between the two does not apply. This theoretical development is presented in Ch. 3. These nonequilibrium radiation models were then implemented in a computer code dubbed LORAN: the Langley Optimized RAdiative Nonequilibrium code. As its name suggests, this code is optimized to provide radiation predictions efficiently, by a judicious selection of spectral points determined from the distribution of radiative transitions. Parametric studies were then performed to determine the minimum set of optimized spectral points which would provide accurate radiative heat flux predictions. This process and its results are described in Ch. 5. The optimized method

is compared to flight- and ground-based measurements, and to other nonequilibrium radiation methods, in Ch. 6. The agreement is generally good.

To compute radiation transport without applying the tangent slab (1-D) approximation, a full 3-D modified differential approximation (MDA) was adopted. The derivation of this method in nonequilibrium is summarized in Ch. 4, while the numerical details of its implementation are presented in App. B. This method is currently limited to axisymmetric flowfields, though the extension to 3-D flows should be straightforward. The method has been demonstrated for two nonequilibrium flight conditions and compared to results from the tangent slab approximation in Ch. 6. The predicted wall radiative heating is 20 to 25 percent lower than the tangent slab result, in line with what would be expected. There are, however, indications that the boundary conditions of the MDA method can be improved. The radiative coupling term, $\nabla \cdot \vec{q}_R$, varies much more smoothly in the MDA solution than in the tangent slab prediction, suggesting that the MDA method may enhance the stability of coupled solutions.

Chapter 7 applies the LORAN radiation model to a study of the sensitivity of radiative heating predictions. Semi-empirical models for the rate controlling temperature in dissociation reactions, the cross section for vibrational to translational energy exchange, and the amount of energy exchange in dissociation, as well as various chemical kinetics models used in nonequilibrium CFD were varied and the effect on the predicted radiative heating levels was examined. The results show that radiation is

very sensitive to these models through their influence on the vibrational temperature. Studies of radiative heating may therefore provide additional insight into the validity of the semi-empirical models which have been developed for nonequilibrium CFD codes.

The nonequilibrium radiation and transport methods developed for this work predict radiative heating to aeroassist vehicles with accuracy similar to that of detailed codes. The computer time and storage requirements are significantly reduced, however. The LORAN method is therefore suitable for use in parametric studies and for coupled solutions with nonequilibrium Navier Stokes codes. Further work on these models is expected to speed up solutions still more.

2 Historical Review

2.1 Topical and Literature Survey

The previous work which has relevance to this problem can be subdivided into several subject areas: nonequilibrium absorption and emission in individual radiating mechanisms, nonequilibrium excitation processes, and transport models.

2.1.1 Nonequilibrium Absorption and Emission

Emission and absorption of radiation in a gas result from transitions between energy levels. In atomic species, all electronic energy levels as well as free electrons may be involved in radiative transitions. For molecules, radiation also occurs due to transitions between rotational and vibrational energy levels. Atomic radiation arises from bound-bound transitions (atomic lines), bound-free transitions (photoionization or radiative deionization), and free-free transitions (Bremsstrahlung radiation). Here “bound” and “free” refer to the state of the electrons involved in the radiation-inducing transition. Molecular radiation is more complex because of the large number of energy levels available for transitions. The resulting structure of closely-spaced lines is referred to as a molecular band system.

The complete spectral variation of emission and absorption is contained in the absorption coefficient, κ_ν , and the emission coefficient, j_ν^e . The absorption coefficient is obtained from the product of the population, N_n , of an energy level and its radiative

absorption cross section, $\sigma_{\nu n}$, summed over all the energy levels available:

$$\kappa_{\nu} = \sum_{\text{energy levels } n} N_n \sigma_{\nu n} \quad (2.1)$$

The emission coefficient is found from a similar expression, in which the amount of energy emitted, $h\nu_{nn'}$ also appears, and the absorption cross section is replaced by the transition probability for emission, $A_{nn'}$:

$$J^e = \sum_{\text{energy levels } n} N_n \sum_{n' < n} h\nu_{nn'} A_{nn'} \quad (2.2)$$

In equilibrium, the electronic energy level populations are determined as a function of temperature according to a Boltzmann distribution. The rotational and vibrational energy levels of each electronic state of a molecule are populated according to the equilibrium partition function. Species concentrations in equilibrium are related by Saha's equation. These equilibrium relations allow radiative properties to be referenced to temperature and the concentrations of a few major species, allowing the development of simple radiation step models. Also, under equilibrium conditions the absorption and emission coefficient are related according to Kirchhoff's law, so that Eq. 2.2 is not needed.

In nonequilibrium, these simple relations for the energy state populations and species concentrations no longer apply. The problem is now to determine the nonequilibrium energy level populations. The rotational and vibrational states in a molecule may be assumed to be populated according to distinct rotational and vibrational temperatures, respectively, if the nonequilibrium is not too severe. The electronic states,

however, equilibrate more slowly so that a single electronic temperature cannot be defined. In this situation, the energy level populations in the absorption and emission coefficients must be calculated individually at every point where they are needed according to the specific local conditions. In addition, the emission coefficient cannot be calculated by Kirchhoff's law. The radiative cross sections, however, depend only on the configuration of an individual atom or molecule. They are the same for equilibrium and nonequilibrium conditions.

A number of sources present expressions for the equilibrium absorption and/or emission coefficients of the individual radiating mechanisms. For example, Zel'dovich and Raizer [6], provide a comprehensive classical development with discussion and references to quantum corrections. Other classic texts present similar results [7]. Armaty [8] provides practical expressions for the continuum absorption coefficients of atoms and ions, following the method of Biberman and Norman [9]; which itself follows their earlier work [10] and that with Ulyanov [11]. The latter work is an attempt to correct the classical hydrogenic model of the atom to account for the actual configuration of a radiating species and its influence on the absorption coefficient. Jones et al. [12] provide a critical review of many of the important radiating mechanisms and species.

A number of other researchers have also considered the contributions of various parts of the spectrum in a more qualitative sense for conditions of interest in re-entry studies. Horton [13] has studied the importance of the ultraviolet portion of the

spectrum as a contributor to the radiative heating of re-entry bodies. He has also studied the potential impact of nonequilibrium on the radiative heating [14].

Only two approaches to absorption and emission in nonequilibrium have been identified. The correction factor method, developed by Clarke and Ferrari [15] and Chapin [2], and now in use by L. A. Carlson and others [16, 17, 18], incorporates a simple equilibrium step model for absorption with correction factors to account for the nonequilibrium of the excited state populations. The detailed line by line method developed by Whiting et al. [19] and implemented for nonequilibrium only in Park's NEQAIR code [20] treats individual rotational lines in the molecular band spectrum as well as individual atomic lines and atomic continuum processes. In this method the nonequilibrium absorption coefficient is obtained by solving for the nonequilibrium populations of the energy levels using the quasi-steady-state (QSS) method described in the next section. The nonequilibrium emission is obtained by calculating a quasi-equilibrium or excitation temperature for each radiative process, allowing the use of Kirchhoff's law.

2.1.2 Nonequilibrium Excitation Processes

To calculate the nonequilibrium populations appearing in the absorption coefficient, the rates of population and depopulation of energy levels must be known or assumptions must be made about how the states are populated. Excitation rate data are not widely available because of the experimental difficulties involved in obtaining them. In the future, computational chemistry may be applied to predict these

rates, but such calculations are costly and therefore computer- and time-limited. Park [3, 20] has collected a set of rates for the principal transitions involved in air radiation and incorporated them into a quasi-steady-state (QSS) model of electronic excitation. The QSS model assumes that the rates of population and depopulation of an energy level are much larger than the net rate of change of the level's population. This allows the excitation calculation to be uncoupled from the flowfield solution. In flow regions with strong gradients (such as inside captured shocks and in boundary layers) this approximation loses accuracy because it neglects the excitation history.

2.1.3 Radiative Transport

The problem of radiative transport is well-known. It requires solving an integro-differential equation for each frequency and for each direction in the flowfield. This complexity arises because unlike a temperature field in conduction problems, the radiation intensity in any direction is independent of that in any other direction; and that at a given frequency (energy) is separate from that at any other frequency. The complete equation of radiative transport has been derived in many sources, including Zel'dovich and Raizer [6], Ozisik [21], and Vincenti and Kruger [22]. Using Ozisik's notation, the governing equation for the spectral radiative intensity, I_ν , in a participating medium is

$$\begin{aligned} \frac{1}{c} \frac{\partial I_\nu(s, \hat{\Omega}, t)}{\partial t} + \frac{\partial I_\nu(s, \hat{\Omega}, t)}{\partial s} + [\kappa'_\nu(s) + \gamma^s_\nu(s)] I_\nu(s, \hat{\Omega}, t) \\ = j^e_\nu(s, t) + \frac{1}{4\pi} \gamma^s_\nu(s) \int_{\Omega'=4\pi} \hat{p}(\hat{\Omega}' \cdot \hat{\Omega}) I_\nu(s, \hat{\Omega}', t) d\Omega' \end{aligned} \quad (2.3)$$

where κ'_ν is the absorption coefficient corrected for induced emission.

The first term on the left-hand-side is immediately omitted in most radiative heat transfer studies because the speed of light, c , is large and the time derivative of intensity is small in most applications of interest. The scattering terms (containing γ_ν^s and \hat{p}) can also be neglected, since the emphasis of the present study is on non-ablating, low-density flows. In such flows there is almost nothing to induce radiation scattering, and $\gamma_\nu^s \approx 0$. With these two simplifications, the transport equation reduces to:

$$\frac{\partial I_\nu(s, \hat{\Omega}, t)}{\partial s} + \kappa'_\nu(s) I_\nu(s, \hat{\Omega}, t) = j_\nu^e(s, t) \quad (2.4)$$

where t is now a parameter. This equation can be solved numerically with the assumption of a one-dimensional medium. For multi-dimensional radiation transport, additional simplifications will be necessary. The most common radiative transport models used to date are the optically thin model and the tangent slab model. The first assumes a transparent gas, so that the transport problem reduces to a simple summation across the region of interest. The second assumes that all properties vary in only one direction, so that the radiative transport equation is reduced to a one-dimensional integro-differential equation. A typical discussion of the tangent slab method can be found in Ozisik [21] or in Nicolet [23, 24]. An extension of Nicolet's method is given by Bolz [25].

Several other approximate methods for the solution of the radiative transport problem have been developed. The optically thick approximation assumes that emit-

ted radiation is reabsorbed within a very small distance from the point of emission [21, Sec. 9.2]. This is not the case for blunt body flowfields, except perhaps at the centers of very strong atomic line transitions, so this method is not applicable to the current problem. Another series of methods, known variously as moment methods, discrete ordinate methods, or spherical harmonics methods, obtain solutions by approximating the radiative intensity with a series of functions of increasing order [21, Sec. 9.8].

Multi-dimensional solutions to the transport problem have been developed by Truelove [26] and Modest [27], but these assume equilibrium flow and the validity of Kirchhoff's law. In addition, Truelove assumes a gray gas, in which the absorption does not vary with wavelength. Cheng and Ozisik [28] have developed a three-dimensional algorithm for stagnation flows, but it uses the diffusion approximation for radiative transfer which is valid only in highly absorbing flows. No multi-dimensional transport algorithm currently in use for flowfield solutions has been identified, though an effort toward this end is underway by Edwards et al. [29].

Equally important to the development of radiative transport algorithms may be the formulation of rules governing the intervals at which radiation must be computed. Especially in a coupled solution, it is preferable to minimize the number of times the costly radiation model is invoked. Bolz [30] has developed an algorithm for selecting a radiation transport subgrid in an equilibrium flowfield by evaluating a weighted average of the derivatives of important flow variables. This avoids calculating radiation

at every grid point in a flowfield region where all the properties are changing very slowly.

2.2 Computer Code Survey

A large number of computer codes for radiation prediction have been developed over the years. Unfortunately, many of these codes fell into disuse during the 1970's when hypersonic research was limited. As a result, most are no longer available for current study without extensive redevelopment. This survey, therefore, will consider only those codes known to be available with minimal reconstruction required.

2.2.1 Equilibrium Radiation Codes

Gray gas

Gray gas models are the simplest of all radiation models, assuming that emission and absorption do not vary with frequency. This assumption is violated for blunt body flowfields, so these models have been rejected as candidates for the current effort and will not be discussed further.

Step models

A number of researchers have developed step models, in which the absorption coefficient is considered constant in several wavelength intervals. Olstad [31] has developed an eight step model, while Zoby et al. [32] used a 58-step model to study outer planet entry. These step models depend on the assumption of equilibrium.

They make extensive use of curve-fits and refer radiation mechanisms to a ground state in order to obtain the desired simplicity.

The eight-step model developed by Olstad [31] is still available. This model makes use of curve-fits for the radiative cross sections assuming equilibrium conditions. It requires input of the concentrations of five species (N, O, N₂, O₂, and e⁻), and uses these to infer the concentrations of minor species, again assuming equilibrium. The details of this model can be found in the reference.

Step models for radiation emphasize simplicity and speed at the expense of accuracy. This trade-off is often acceptable for engineering methods which provide estimates of the radiative heat load. These simple models are ill-suited to nonequilibrium, however, where properties are no longer simple functions of temperature and pressure but depend also on the concentrations of the various species. In that situation, the simple relationships used to develop step models no longer hold.

RAD/EQUIL

The RAD/EQUIL code developed by Nicolet [23, 33] is still in use in its original form. It also serves as the basis for at least two coupled equilibrium inviscid flow codes: RIFSP, which computes a stagnation line for a blunt body; and RAIF, which computes a complete blunt forebody [34]. This method is a hybrid between the step models and detailed models. It computes continuum processes from curve-fits for equilibrium, and reports the results at a finite number of points (generally 20-40). The line radiation is computed in greater detail, with each line considered being

represented by fifteen spectral points. However, these detailed results are integrated by the code, and presented at a small number of intervals (detailed output can also be obtained, but is not the default). This process provides results of good accuracy and allows concise reporting.

2.2.2 Nonequilibrium Radiation Codes

RADMC

This nonequilibrium correction factor method is currently being developed by a number of researchers [16, 17, 18, 35]. It will be referred to collectively as the RADMC method. In this method, the eight-step model for absorption developed by Olstad [31] is adopted to describe the radiation spectrum. Approximate correction factors for nonequilibrium energy level populations are then developed. These depend on modeling the excitation with a small number of energy levels. The result is a very fast but approximate nonequilibrium radiation model.

NEQAIR

The detailed line-by-line approach developed by Whiting et al. [19] is implemented for nonequilibrium in the NEQAIR code of Park [20]. This method includes detailed descriptions of the radiative transitions, computing each individually. The nonequilibrium electronic state populations are calculated using the QSS approximation. This is a very detailed but computationally costly model for nonequilibrium radiation. Typical calculations require on the order of 10^5 to 10^6 spectral points [29, 36].

Direct Simulation Monte Carlo

An emerging method models radiation in a Direct Simulation Monte Carlo (DSMC) flowfield solution. The radiation modeling for DSMC is still being refined but has great potential, particularly for nonequilibrium low density flows. The power of DSMC lies in its direct modeling of the physical processes involved, and therefore suffers most from uncertainties in what these models and their parameters should be. It also requires large amounts of computer time, though advancements are reducing this considerably. The computer time required is proportional to the flow density, however, restricting the usefulness of DSMC for lower altitudes. Moss and Price give some initial results for the Aeroassist Flight Experiment (AFE) vehicle in both forebody and wake regions [37] using a method developed by Bird [38]. A. B. Carlson [39, 40] has also studied a shock tube condition with a DSMC method including radiation.

2.3 Survey of Experimental Results

2.3.1 Ground-Based Data

The principal source of ground-based data is a series of shock tube experiments performed by the Avco-Everett Research Laboratory around the early 1960's. These results are reported in a number of sources, including Teare et al., [41], Allen et al. [42, 43, 44, 45], and Kivel [46]. The conditions tested include velocities between 6 and 10 km/sec. Only the high end of this range is of interest for the current problem.

Experiments were also performed by Page [47, 48, 49] and Nerem et al. [50, 51, 52, 53, 54, 55, 56, 57, 58, 59, 60]. These shock tube results are difficult to use because the data were reinterpreted in the years following the experiments. No attempt will therefore be made to match this data here.

2.3.2 Flight Data

Project FIRE

The FIRE flight project of the mid-1960's was conducted to determine the heat load on an Apollo-type vehicle entering Earth's atmosphere at 11.4 km/sec [61, 62]. It is one of the only sources of flight radiative heating data applicable to the present area of study and will therefore be emphasized in verifying the development of this radiative heating prediction method.

Future Flight Projects

Looking to the future, NASA's Aeroassist Flight Experiment is anticipated to provide radiative heating data for a blunt body on an aerobraking trajectory in the earth's atmosphere. The heat shield design is non-ablating, and both the forebody and wake regions are planned to be instrumented. The data from this project should provide a valuable verification set for radiation prediction methods.

3 Radiation Theory

Absorption and emission coefficients describing the radiation phenomena occurring in a blunt body flowfield can be developed under conditions of thermochemical nonequilibrium for each participating transition between energy levels. The development for the absorption coefficient corresponding to each type of transition is presented below. A similar development for the emission coefficients is given in Sec. 3.2.

3.1 Absorption

3.1.1 Atomic Mechanisms

Bound-Bound Transitions

The model for radiation absorption in bound-bound transitions used in the present study is that developed by Nicolet [23] for the RAD/EQUIL code. This model resolves a line by distributing about 15 spectral points starting from the line center as shown in Fig. 3.1. It has been modified as required for nonequilibrium. Following Nicolet's development, the absorption coefficient in a line is given by

$$\kappa_\nu = \frac{\pi e^2}{mc} f_{lu} N_l b(\nu, N_e, T_t, T_e \dots) \quad (3.1)$$

where f_{lu} is the oscillator strength of the transition, N_l is the nonequilibrium population of the lower state of the transition, and b is the line shape function which may depend on a large number of variables. The constants e , m , and c are the electron charge, electron mass, and speed of light, respectively.

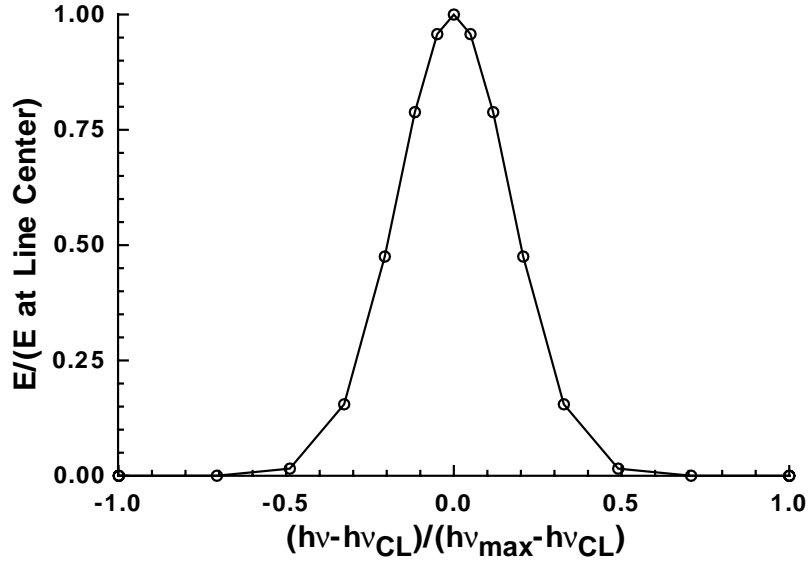


Figure 3.1. Distribution of Spectral Points for an Atomic Line

The line shape is a normalized function which can be described by one of a number of theoretical models depending on the predominant broadening mechanism. Two such line shapes are considered here. The Lorentz shape describes lines in which Stark broadening by electron impact dominates, as is the case for heavy atomic species. This line shape is given as

$$b_\nu = \frac{\gamma^S / \pi}{(\nu - \nu_{CL})^2 + (\gamma^S)^2} \quad (3.2)$$

where the dependence of b on the gas conditions has been omitted. Here γ^S is the Stark (half) half width, and ν_{CL} is the frequency of the line center. The (half) half width is the half-width of the line at half its height, and is a common descriptor for line shapes.

The (half) half widths have been calculated by a number of authors, most notably

Griem [63]. Page et al. [64] have noted that these line widths vary with a power n of temperature T as

$$\gamma^S(T) \approx \left(\frac{T}{T_0}\right)^n \gamma^S(T_0) \quad (3.3)$$

thus allowing use of a single input reference at the reference temperature T_0 for Stark broadening. In nonequilibrium, the temperature in this equation should be the electron temperature T_e .

The mechanism of resonance broadening (also called collision or pressure broadening) yields Lorentz line shapes as well. This mechanism may exceed Stark broadening for situations with low ionization. Nicolet [23] gives the approximate (half) half width as

$$\gamma^R \approx 3\pi \left(\frac{g_l}{g_u}\right) \left[\frac{e^2 f^R}{2\pi m \nu^R}\right] N_a \quad (3.4)$$

where N_a is the number of perturbing atoms per unit volume, and g_l and g_u are the degeneracies of the upper and lower states, respectively. The effective Lorentz line width is then the sum of γ^S and γ^R .

The second type of line shape is the Doppler profile, which describes line broadening due to thermal motion of the atoms. This Gaussian line shape is given as

$$b_\nu = \frac{1}{\gamma^D} \sqrt{\frac{\ln 2}{\pi}} \exp \left[-\frac{(\nu - \nu_{CL})^2 \ln 2}{(\gamma^D)^2} \right] \quad (3.5)$$

The Doppler (half) half width is given by

$$\gamma^D = \frac{\nu_{CL}}{c} \sqrt{\frac{2kT_t \ln 2}{m_s}} \quad (3.6)$$

where k is Boltzmann's constant and m_s is the mass of the radiating particle of species s . The temperature is the heavy particle translational temperature, since the effect is due to the thermal motion of the atoms.

The Lorentz and Doppler line shapes can be combined into a single curve known as the Voigt line shape which requires significantly more computation. Under the conditions of interest in this study, the two (half) half-widths have been found to be of different orders of magnitude. Therefore, it is felt that the use of one or the other of the simpler line shapes should be adequate. Once the choice is made for each given condition, the absorption coefficient in a line can be computed from Eq. 3.1, using input data for the oscillator strength and the line width and predicted nonequilibrium energy level populations.

Bound-Free Transitions

A model for bound-free transitions can be developed assuming a hydrogen-like atom. A good source of such a development for an equilibrium gas is Zel'dovich and Raizer [6, Sec.5.5]. The radiative cross sections developed there apply also to nonequilibrium since the configuration of an individual atom is unchanged. From that reference therefore the cross section for an atomic energy level n is:

$$\sigma_{\nu n} = \frac{1}{\sqrt{3}} \frac{64\pi^4 m Z^4 e^{10}}{3\nu^3 c h^6 n^5} \quad (3.7)$$

where Z is the charge number ($Z = 1$ for neutral species) and h is Planck's constant.

Once the cross section is known it is a simple matter to compute the spectral ab-

sorption coefficient for the bound-free process, given the nonequilibrium populations of the electronic energy levels of the atom. The relation is

$$\kappa_\nu = \sum_{n^*}^{\infty} N_n \sigma_{\nu n} \quad (3.8)$$

The lower limit n^* indicates the photoionization threshold. This is the lowest atomic energy level from which a photon of frequency ν can detach an electron. The upper limit in practice has a finite value corresponding to ionization of the atom.

While quite accurate, Eq. 3.7 can still be improved. In particular, a quantum correction [6, p. 266] may be applied to it. However, as stated in the reference, the impact of this correction is negligible for most cases of practical interest. More significant is the error in this expression for low quantum states near the ground atomic state. For these states, the hydrogen-like assumption may induce considerable error. For many atoms, the cross section of the ground state is well known from experimental data. This information can be used for transitions involving the ground state instead of the value predicted by Eq. 3.7.

Free-Free Transitions

A model for free-free transitions can be developed using similar semi-classical methods. Only transitions due to the proximity of an atomic ion are considered. Free-free transitions caused by the presence of neutral atoms and molecules are assumed to be negligible. Zel'dovich and Raizer [6, Ch. 5.3] is again a good source. Their result can be rederived without using equilibrium assumptions except for a

Maxwell distribution of the energies of the free electrons at the electron translational temperature T_e . In this case, the only change in the result is that T_e replaces T_t . The equation for the free-free absorption coefficient can therefore be written as

$$\kappa_\nu = \frac{4}{3} \left(\frac{2\pi}{3mkT_e} \right)^{1/2} \frac{Z^2 e^6}{hcm\nu^3} N_+ N_e \quad (3.9)$$

where N_+ and N_e are the concentrations of the appropriate ion and of electrons, respectively.

This result could also be modified by a quantum correction, but again the effect is minimal for the conditions of interest here.

3.1.2 Molecular Mechanisms

The treatment of molecular radiation requires consideration of vibrational and rotational transitions within the molecule, as well as electronic transitions; and combinations of the different types of transition. Each such transition contributes a discrete line to the radiation spectrum, whose line center frequency is determined by the energy differential of the transition. While a line-by-line calculation of molecular radiation is possible, it does not fit the requirements of the present study for a relatively rapid calculation method which can be coupled to a flowfield code. As an alternative, therefore, the “smeared band” model of molecular radiation will be adopted here. In this model, the rotational line structure of the molecular radiation is smoothed to provide a continuous variation of the absorption coefficient. Because the rotational energy levels are so closely spaced, the lines resulting from rotational

transitions are nearly overlapping except in very rarefied conditions. The error introduced by this approximation should therefore be acceptable under most conditions of interest.

The basic development of the “smeared band” model can be found in a number of sources. The development given below is an enhancement of that found in Zel’dovich and Raizer [6, Sec. 5.3]. It incorporates higher order expressions for the molecular energy levels from Herzberg [65], while eliminating equilibrium assumptions. In what follows ZR will refer to the text by Zel’dovich and Raizer. Herzberg will refer to the just-quoted reference.

The energy differentials for the molecular transitions will be established first. For electronic transitions, the energy levels are given by E_e , the electron energy of a particular energy level measured from the ground state. For vibrational transitions, the energy levels are obtained from the fourth order expression given by Herzberg

$$E_v = hc \left[\omega_e \left(v + \frac{1}{2} \right) - \omega_e x_e \left(v + \frac{1}{2} \right)^2 + \omega_e y_e \left(v + \frac{1}{2} \right)^3 + \omega_e z_e \left(v + \frac{1}{2} \right)^4 \right] \quad (3.10)$$

which includes a correction for the anharmonicity of the vibrational energy potential. The vibrational levels range from the zero-point energy at $v = 0$ to some maximum v determined by the dissociation of the molecule. The coefficients in the above expression are spectroscopic constants which are available from a number of sources. The energy levels for the rotational transitions, including a correction for non-rigid oscillators, are

$$E_r = hc \left[B_v J(J+1) - D_v J^2(J+1)^2 \right] \quad (3.11)$$

where the spectroscopic constant B_v has been corrected for rotational effects as

$$B_v = B_e - \alpha_e \left(v + \frac{1}{2} \right) \quad (3.12)$$

and the second rotational spectroscopic constant D_v is

$$D_v = D_e + \beta_e \left(v + \frac{1}{2} \right) \approx D_e = \frac{4B_e^3}{\omega_e^2} \quad (3.13)$$

These levels range from zero energy at $J = 0$ to some maximum J again determined by dissociation of the molecule for each vibrational level.

The complete molecular energy level is

$$E_{tot} = E_e + E_v + E_r \quad (3.14)$$

where the individual energy contributions are given by Eqs. 3.10 and 3.11 above.

Designating the upper level by the superscript u and the lower level by l the wave number (inverse wavelength) of a particular transition is

$$\frac{1}{\lambda} = \frac{E_{tot}^u - E_{tot}^l}{hc} \quad (3.15)$$

For convenience in manipulating these expressions one special wave number is defined. This is the wave number with zero rotational quantum number and arbitrary vibrational quantum numbers:

$$\frac{1}{\lambda_{v^u v^l}} = \frac{E_e^u - E_e^l}{hc} + \frac{E_v^u - E_v^l}{hc} \quad (3.16)$$

The formidable expression for the wave number of an individual transition is simplified by the selection rules for rotation. These rules are discussed in various

sources including ZR and Herzberg, and result in the requirement that $\Delta J = J^u - J^l = 0, +1, \text{ or } -1$. In addition, the 0-0 rotational transition is forbidden and in the case of transitions between certain molecular states denoted by Σ all $\Delta J = 0$ transitions are forbidden. A detailed discussion of these selection rules and of the designation of molecular states is outside the scope of the present work. Nevertheless, these rules allow the development of three specific wave numbers for the $\Delta J = -1, 0, 1$ transitions, which are denoted P, Q, and R respectively.

$$\begin{aligned} \frac{1}{\lambda_P} = & \frac{1}{\lambda_{v^u v^l}} + J^{l^4} (D_e^l - D_e^u) + J^{l^3} (2D_e^l + 2D_e^u) \\ & + J^{l^2} (D_e^l - B_v^l - D_e^u + B_v^u) + J^l (-B_v^u - B_v^l) \end{aligned} \quad (3.17)$$

$$\begin{aligned} \frac{1}{\lambda_Q} = & \frac{1}{\lambda_{v^u v^l}} + J^{l^4} (D_e^l - D_e^u) + J^{l^3} (2D_e^l - 2D_e^u) \\ & + J^{l^2} (D_e^l - B_v^l - D_e^u + B_v^u) + J^l (B_v^u - B_v^l) \end{aligned} \quad (3.18)$$

$$\begin{aligned} \frac{1}{\lambda_R} = & \frac{1}{\lambda_{v^u v^l}} + J^{l^4} (D_e^l - D_e^u) + J^{l^3} (2D_e^l - 6D_e^u) + \\ & J^{l^2} (D_e^l - B_v^l - 13D_e^u + B_v^u) + J^l (3B_v^u - 12D_e^u - B_v^l) + 2B_v^u - 4D_e^u \end{aligned} \quad (3.19)$$

Once the molecular band spectra are thus determined, it is necessary to evaluate the probability of a transition between levels in order to obtain an expression for the absorption coefficient. This probability is obtained from a quantum mechanical analysis. The resulting expression for the transition probability is given for instance in ZR:

$$A_{ul} = A_{Av^l J^l}^{Bv^u J^u} = \frac{64\pi^4}{3hc^3} \nu_{Bv^u J^u, Av^l J^l}^3 D_{elBA}^2 q_{v^u v^l} p_{J^u J^l} \quad (3.20)$$

where $q_{v^u v^l}$ is the Franck-Condon factor for the probability of a vibrational transition, and $p_{J^u J^l}$ is the probability of a rotational transition. D_{elBA}^2 is the square of the matrix element¹ arising from the wave function in the quantum mechanical analysis. A is the Einstein coefficient for spontaneous emission, while super- and subscripts A and B denote the lower and upper electronic levels, respectively. Using the principle of detailed balancing leads to the well-known relationship between the Einstein coefficients for emission and absorption (see for instance [66] or ZR)

$$B_{lu} = \frac{c^2}{8\pi h \nu_{ul}^3} \frac{g_u}{g_l} A_{ul} \quad (3.21)$$

Note that if this relationship is expressed for energy states rather than energy levels the degeneracies g_u and g_l are identically one, by definition. As a practical matter the use of energy levels, which may be degenerate, is preferred because it reduces the bookkeeping required.

The absorption coefficient, κ_{lu} , is related to the Einstein coefficient for absorption, B_{lu} , by [22]

$$\kappa_{lu} = n_l B_{lu} h \nu_{lu} \quad (3.22)$$

Substituting Eqs. 3.20 and 3.21 in this last expression yields the desired expression for the spectral absorption coefficient:

$$\kappa_{\nu_{Av^l J^l, Bv^u J^u}} = \frac{g_{Bv^u J^u}}{g_{Av^l J^l}} \frac{8\pi^3}{3hc} N_{Av^l J^l} \nu_{Av^l J^l, Bv^u J^u} D_{elBA}^2 q_{v^u v^l} p_{J^u J^l} F(\nu) \quad (3.23)$$

where $F(\nu)$ is a normalized line shape. This expression must be evaluated for each A,

¹*sr2*, used by Park in NEQAIR, is the nondimensional value, which is divided by $(a_0 e)^2$, the squared product of the Bohr radius and the charge of an electron.

B, v^u, v^l, J^u, J^l in order to obtain the complete absorption spectrum of a molecular species. The “smeared band” model averages out the rotational line structure. This is done by summing Eq. 3.23 over J^u , and introducing an average frequency, $\overline{\nu}_{Bv^u, Av^l}$, for the rotational lines. The result is:

$$\kappa_{\nu_{Av^l J^l, Bv^u}} = \frac{8\pi^3}{3hc} \frac{g_B}{g_A} N_{Av^l J^l} D_{elBA}^2 q_{v^u v^l} F(\nu) \overline{\nu}_{Bv^u, Av^l} \quad (3.24)$$

where use has been made of the relation $\sum_{J^u}^{\infty} p_{J^u J^l} = 1$ which expresses the fact that all transitions occur between two levels of the molecule. The degeneracy has been expanded into its components:

$$g_{AvJ} = g_A g_v g_J \quad (3.25)$$

where

$$g_v = 1 \quad (3.26)$$

since there are no degenerate vibrational levels, and

$$g_J = 2J + 1 \quad (3.27)$$

For the vast majority of rotational lines, $J \gg 1$, and the ratio of rotational degeneracies in Eq. 3.23 is approximately equal to one. This approximation has been used even for transitions with small J . While the error introduced in a single transition with a low rotational quantum number can be as much as 300 percent, only a few transitions have low J so the effect on the overall absorption coefficient is small. The error incurred by introducing the average frequency $\overline{\nu}_{Bv^u, Av^l}$ for all rotational lines in the $v^l - v^u$ band is minimal, on the order of one to seven percent.

Proceeding towards the complete absorption coefficient, Eq. 3.24 is now summed over the final vibrational level v^u . This yields

$$\kappa_{\nu_{Av^l J^l, B}} = \frac{8\pi^3 g_B}{3hc g_A} N_{Av^l J^l} D_{elBA}^2 F(\nu) \sum_{v^u}^{\infty} q_{v^u v^l} \bar{\nu}_{Bv^u, Av^l} \quad (3.28)$$

Here the frequency remains inside the summation and is not averaged, as the variation involved can be large.

The mean value theorem is then used to define an average absorption coefficient for a line, by integrating over one line width:

$$\int_{line} \kappa_{\nu_{Av^l J^l, B}} d\nu = \frac{8\pi^3 g_B}{3hc g_A} N_{Av^l J^l} D_{elBA}^2 \sum_{v^u}^{\infty} q_{v^u v^l} \bar{\nu}_{Bv^u, Av^l} = \bar{\kappa}_{\nu_{Av^l J^l, B}} \Delta\nu \quad (3.29)$$

where $\Delta\nu$ is the line width.

Equation 3.29 is then solved for $\bar{\kappa}_{\nu}$ and summed over the initial rotational and vibrational levels.

$$\bar{\kappa}_{\nu_{AB}} = \frac{8\pi^3 g_B}{3hc g_A} D_{elBA}^2 \sum_{v^l}^{\infty} \sum_{v^u}^{\infty} q_{v^u v^l} \bar{\nu}_{Bv^u, Av^l} \sum_{J^l}^{\infty} \frac{N_{Av^l J^l}}{\Delta\nu} \quad (3.30)$$

where the sum term is zero for any transition which does not absorb radiation in the frequency interval under consideration.

Equation 3.30 is the complete formula for the “smeared band” absorption coefficient for a molecular species. In this form it contains two approximations: the use of an average frequency for the rotational lines in a vibrational band, and the averaging over a single line. In order to use this expression in a radiation model, its various parts must now be amplified in terms of known quantities.

Under conditions of nonequilibrium, the number density in a particular energy level is given by the following expression, where the existence of rotational and vibrational temperatures has been assumed.

$$N_{Av^lJ^l} = N_A \frac{\exp(-E_{v^l}/kT_v)}{Q_v(T_v)} \frac{g_{J^l} \exp(-E_{J^l}/kT_r)}{Q_r(T_r)} \quad (3.31)$$

Q_v and Q_r are the vibrational and rotational partition functions, respectively. The population of the electronic energy level N_A must be obtained from some nonequilibrium excitation calculation. In the present work, Park's quasi-steady-state (QSS) method [67] has been used. The partition functions are obtained from their definition:

$$Q_x(T_x) = \sum_{x=0}^{\infty} \exp(-E_x/kT_x) \quad (3.32)$$

In practice the upper limit of this summation is imposed either by predissociation in the rotational case or by numerical limits arising from inaccuracies in the higher order coefficients of Eq. 3.10 for the vibrational case. The rotational case will be discussed in a separate section below. For the vibrational case, the sum may be terminated when the contribution of the next term is less than some threshold percentage of the partition function. It is also necessary to monitor the size of each term to detect the onset of significant inaccuracies in Eq. 3.10. These occur at a high enough vibrational quantum number that the sum for the partition function can be truncated at that point.

The next term to be examined in Eq. 3.30 is the $\Delta\nu$ term. This term introduces another approximation of the “smeared band” model. The line width $\Delta\nu$ is assumed

to be approximately equal to an average line spacing. To evaluate the line spacing, consider the three expressions for the line centers, Eqs. 3.17 to 3.19. If the D_e terms are neglected compared to the B_v terms, since they are much smaller, the equations reduce to:

$$\frac{1}{\lambda_P} = \frac{1}{\lambda_{v^u v^l}} + J^{l^2} (B_v^u - B_v^l) + J^l (-B_v^u - B_v^l) \quad (3.33)$$

$$\frac{1}{\lambda_Q} = \frac{1}{\lambda_{v^u v^l}} + J^{l^2} (B_v^u - B_v^l) + J^l (B_v^u - B_v^l) \quad (3.34)$$

$$\frac{1}{\lambda_R} = \frac{1}{\lambda_{v^u v^l}} + J^{l^2} (B_v^u - B_v^l) + J^l (3B_v^u - B_v^l) + 2B_v^u \quad (3.35)$$

For a line with $J^l \gg 1$, which is the case for most lines, these three expressions collapse into the single form:

$$\frac{1}{\lambda} = \frac{\nu}{c} \simeq \frac{1}{\lambda_{v^u v^l}} + J^{l^2} (B_v^u - B_v^l) \quad (3.36)$$

Solving for ν and taking the derivative with respect to J , remembering that $\Delta J = 1$ for adjacent lines, gives

$$\Delta\nu = 2cJ^l |B_{v^u} - B_{v^l}| \quad (3.37)$$

where the absolute value is taken to ensure that the average spacing is positive. Equation 3.36 also yields an approximate expression for J^l in terms of the wavelength or wave number:

$$J^{l^2} \simeq \left(\frac{1}{\lambda} - \frac{1}{\lambda_{v^u v^l}} \right) \frac{1}{B_{v^u} - B_{v^l}} \quad (3.38)$$

Note that since $J^{l^2} > 0$, the right-hand-side of this equation must also be positive. This implies for $B_{v^u} > B_{v^l}$ that $\lambda_{v^u v^l} > \lambda$, and for $B_{v^u} < B_{v^l}$ that $\lambda_{v^u v^l} < \lambda$. These requirements are the mathematical statement of the fact that each vibrational band

absorbs in only a portion of the spectrum. In evaluating the absorption coefficient for a particular band, the wavelength or frequency under consideration must be checked against the above conditions to avoid adding superfluous contributions.

Returning now to Eq. 3.11 for the rotational energy levels, the assumption of $J^l \gg 1$ is again made. This allows the replacements $J^l + 1 \approx J^l$ and $2J^l + 1 \approx 2J^l$. Equation 3.38 can then be substituted in Eq. 3.11, with the result:

$$E_r \simeq hc \left\{ \left[B_e^l - \alpha_e^l \left(v^l + \frac{1}{2} \right) \right] \left(\frac{1}{\lambda} - \frac{1}{\lambda_{v^u v^l}} \right) \frac{1}{B_{v^u} - B_{v^l}} - \frac{4B_e^{l^3}}{\omega_e^{l^2}} \left(\frac{1}{\lambda} - \frac{1}{\lambda_{v^u v^l}} \right)^2 \frac{1}{(B_{v^u} - B_{v^l})^2} \right\} \quad (3.39)$$

This expression can then be substituted in the rotational exponent in Eq. 3.31. It constitutes the final approximation of the “smeared band” model.

The last term to evaluate in Eq. 3.30 is the averaged frequency, $\overline{\nu}_{Bv^u, Av^l}$. This must be evaluated separately for Σ and non- Σ transitions according to the rotational selection rules discussed above. For a given vibrational transition, Eqs. 3.17 to 3.19 describe the line centers of each rotational transition (with Eq. 3.18 not allowed for Σ transitions). Recalling also that the 0-0 rotational transition is always forbidden, $\overline{\nu}_{Bv^u, Av^l}$ can be evaluated as follows.

$$\overline{\nu}_{Bv^u, Av^l} = \overline{\left(\frac{c}{\lambda} \right)}_{Bv^u, Av^l} = \frac{c}{3J_{max}^l + 1} \left[\sum_{J^l=1}^{J_{max}^l} \left(\frac{1}{\lambda_P} + \frac{1}{\lambda_Q} + \frac{1}{\lambda_R} \right) + \frac{1}{\lambda_R|_{J^l=0}} \right] \quad (3.40)$$

$$\overline{\nu}_{Bv^u, Av^l} = \overline{\left(\frac{c}{\lambda} \right)}_{Bv^u, Av^l} = \frac{c}{2J_{max}^l + 1} \left[\sum_{J^l=1}^{J_{max}^l} \left(\frac{1}{\lambda_P} + \frac{1}{\lambda_R} \right) + \frac{1}{\lambda_R|_{J^l=0}} \right] \quad (3.41)$$

where the first form is for non- Σ transitions, and the second for Σ transitions.

Substituting Eqs. 3.17 to 3.19 in Eq. 3.40 and 3.41 and collecting terms results in the following expressions for the averaged frequency.

$$\begin{aligned} \bar{\nu}_{Bv^u, Av^l} = & \frac{c}{\lambda_{v^u v^l}} + \frac{c(J_{max}^l + 1)}{3J_{max}^l + 1} (2B_v^u - 4D_e^u) + \frac{c}{3J_{max}^l + 1} \\ & \left\{ (3D_e^l - 3D_e^u) (J_{max}^l + 1)(2J_{max}^l + 1)(3J_{max}^{l^2} + 3J_{max}^l + 1) \frac{J_{max}^l}{30} \right. \\ & + (6D_e^l - 6D_e^u) \frac{J_{max}^{l^2} (J_{max}^l + 1)^2}{4} + (3B_v^u - 3B_v^l - 15D_e^u + 3D_e^l) \\ & \left. \frac{J_{max}^l (J_{max}^l + 1)(2J_{max}^l + 1)}{6} + (3B_v^u - 3B_v^l - 12D_e^u) \frac{J_{max}^l (J_{max}^l + 1)}{2} \right\} \end{aligned} \quad (3.42)$$

$$\begin{aligned} \bar{\nu}_{Bv^u, Av^l} = & \frac{c}{\lambda_{v^u v^l}} + \frac{c(J_{max}^l + 1)}{2J_{max}^l + 1} (2B_v^u - 4D_e^u) + \frac{c}{2J_{max}^l + 1} \\ & \left\{ (2D_e^l - 2D_e^u) (J_{max}^l + 1)(2J_{max}^l + 1)(3J_{max}^{l^2} + 3J_{max}^l + 1) \frac{J_{max}^l}{30} \right. \\ & + (4D_e^l - 4D_e^u) \frac{J_{max}^{l^2} (J_{max}^l + 1)^2}{4} + (2B_v^u - 2B_v^l - 14D_e^u + 2D_e^l) \\ & \left. \frac{J_{max}^l (J_{max}^l + 1)(2J_{max}^l + 1)}{6} + (2B_v^u - 2B_v^l - 12D_e^u) \frac{J_{max}^l (J_{max}^l + 1)}{2} \right\} \end{aligned} \quad (3.43)$$

where again the first form is for non- Σ transitions, and the second for Σ transitions.

While these equations could be implemented as is, it is simpler and still accurate to again neglect the D_e terms compared to the B_v terms. The result is:

$$\bar{\nu}_{Bv^u, Av^l} = c \left[\frac{1}{\lambda_{v^u v^l}} + \frac{2B_v^u (J_{max}^l + 1)}{3J_{max}^l + 1} + \frac{3(B_v^u - B_v^l)}{3J_{max}^l + 1} J_{max}^l (J_{max}^l + 1)(J_{max}^l + 2) \right] \quad (3.44)$$

$$\bar{\nu}_{Bv^u, Av^l} = c \left[\frac{1}{\lambda_{v^u v^l}} + \frac{2B_v^u (J_{max}^l + 1)}{2J_{max}^l + 1} + \frac{2(B_v^u - B_v^l)}{2J_{max}^l + 1} J_{max}^l (J_{max}^l + 1) \frac{(J_{max}^l + 2)}{3} \right] \quad (3.45)$$

These equations for non- Σ and Σ transitions can then be substituted in Eq. 3.30, and the averaged spectral absorption coefficient can be calculated.

The final result for the “smeared band” molecular absorption coefficient is

$$\begin{aligned} \bar{\kappa}_{\nu_{AB}} = & \frac{8\pi^3}{3hc} \frac{g_B}{g_A} D_{elBA}^2 \sum_{v^l} \sum_{v^u} q_{v^u v^l} \bar{\nu}_{B_{v^u}, A_{v^l}} \\ & \sum_{J^l} N_A \frac{\exp(-E_{v^l}/kT_v)}{Q_v(T_v)} \frac{2J^l + 1}{2cJ^l |B_{v^u} - B_{v^l}| Q_r(T_r)} \\ & \exp(-hc \left\{ \left[B_e^l - \alpha_e^l \left(v^l + \frac{1}{2} \right) \right] \left(\frac{1}{\lambda} - \frac{1}{\lambda_{v^u v^l}} \right) \frac{1}{B_{v^u} - B_{v^l}} \right. \\ & \quad \left. - \frac{4B_e^{l^3}}{\omega_e^{l^2}} \left(\frac{1}{\lambda} - \frac{1}{\lambda_{v^u v^l}} \right)^2 \frac{1}{(B_{v^u} - B_{v^l})^2} \right\} / kT_r) \end{aligned} \quad (3.46)$$

where $\bar{\nu}$ is given by Eq. 3.44 for non- Σ transitions, and by Eq. 3.45 for Σ transitions, and the vibrational energy E_{v^l} is evaluated from Eq. 3.10 with the appropriate values for the lower energy level. To be consistent, the approximation $2J^l + 1 \approx 2J^l$ is used to reduce the fraction inside the summation over J^l .

Maximum Rotational Quantum Number

The maximum rotational quantum number J_{max} can be determined to varying levels of approximation. The first order calculation would predict the maximum to occur when the energy of a level exceeds the dissociation energy of the species. As discussed in Herzberg [65], however, predissociation may occur due to the shape of the energy potential curve. Whiting et al. [19] developed a computer code based on this fact to predict the maximum rotational quantum number. The method was later refined by Whiting [68]. This most recent method has been adopted for use here. For each vibrational band of each molecular contributor, it computes the maximum allowable rotational quantum number to be considered, based on the shape of the

Morse-centrifugal potential describing the rotating and vibrating molecule.

Further enhancements to the theory for the maximum rotational quantum number are possible, but it is felt that this level of accuracy is sufficient for the current work.

3.2 Emission

Under equilibrium conditions, the emission coefficient is found from the absorption coefficient using Kirchhoff's law.

$$j_\nu^e(s) = \kappa_\nu(s) I_{\nu p}(T) (1 - \exp(-h\nu/kT)) \quad (3.47)$$

where the factor in parentheses accounts for induced emission and the black body or Planck intensity is

$$I_{\nu p}(T) = \frac{2h\nu^3}{c^2 [\exp(h\nu/kT) - 1]} \quad (3.48)$$

Combining these two equations gives the following relation for emission:

$$j_\nu^e(s) = \kappa_\nu(s) \frac{2h\nu^3}{c^2} \exp(-h\nu/kT) \quad (3.49)$$

which depends on the existence of an equilibrium temperature T .

In nonequilibrium, the single temperature T is not defined. Two approaches for finding the emission coefficient are possible. A quasi-equilibrium or excitation temperature appropriate to each radiative transition can be calculated, from which individual contributions to the emission can be obtained. This is the approach adopted in the NEQAIR code [20]. Alternately, expressions for the emission coefficient can be found for nonequilibrium from considerations of detailed balancing. In principle,

these two approaches should lead to the same result. However, the definition of an excitation temperature for use in the first approach is very sensitive to predicted nonequilibrium energy level populations that depend on rate data with significant uncertainties. An excitation temperature is defined by assuming that a Boltzmann or Saha equilibrium exists between the upper and lower level populations for a transition. For some nonequilibrium population distributions negative excitation temperatures can be computed. For bound-free transitions, for example, solving Saha's equation for T gives:

$$T_{ex} = \frac{I - E_n}{k \ln (N_n/N_+/N_e/f(T_e))} \quad (3.50)$$

If the nonequilibrium population of level n is small the argument of the logarithm may be less than one (the function $f(T_e)$ in this equation is a combination of partition functions), resulting in a negative excitation temperature. Such negative temperatures have no physical meaning and therefore require that some justification be developed if they are to be used. The detailed balancing approach avoids this difficulty and is therefore employed in LORAN. The necessary expressions for the emission coefficients of the various radiative transitions are developed below.

3.2.1 Atomic Mechanisms

Bound-Bound Transitions

The radiative emission from an atomic line is given by: [6]

$$J^e = N_u h\nu_{ul} A_{ul} \quad (3.51)$$

where A_{ul} is the Einstein coefficient for spontaneous emission of the transition from the upper atomic energy level u to the lower level l . Detailed balancing relates A_{ul} to the absorption oscillator strength f_{lu} as follows:

$$A_{lu} = \frac{8\pi^2 e^2}{mc^3} \frac{g_l}{g_u} \nu_{ul}^2 f_{lu} \quad (3.52)$$

Combining these two equations leads to the spectral emission coefficient for bound-bound atomic transitions. The line shape b is the same as that for absorption.

$$j_\nu^e = \frac{2\pi h e^2}{mc^3} \frac{g_l}{g_u} \nu_{ul}^3 f_{lu} N_u b(\nu, N_e, T_e, \dots) \quad (3.53)$$

Bound-Free Transitions

Bound-free emission results from the capture of a free electron into an ion. The cross section for this process is given by Zel'dovich and Raizer: [6]

$$\sigma_{cn} = \frac{128\pi^4}{3\sqrt{3}} \frac{Z^4 e^{10}}{mc^3 h^4 v^2 n^3 \nu} \quad (3.54)$$

where v is the initial speed of the captured electron. The number n_c of such captures into the n th energy level for electrons with speeds between v and $v + dv$ per unit volume per unit time is

$$n_c = N_+ N_e f(v) dv \nu \sigma_{cn} \quad (3.55)$$

The electron speeds are distributed according to the distribution function $f(v)$ which is assumed to be a Maxwell distribution in equilibrium at the electron translational temperature T_e . The energy emitted, $h\nu_{ul}$, where the subscript u now denotes the

free state, is given by the sum of the initial kinetic energy of the electron and the net energy required to reionize it from the final energy level l .

$$h\nu_{ul} = \frac{mv^2}{2} + (I - E_l) \quad (3.56)$$

I is the ground state ionization potential. E_l is the energy of the bound level, measured from the ground atomic state. This equation is solved for v^2 and substituted to eliminate v in favor of the frequency ν in Eqs. 3.54 and 3.55.

Combining all these pieces, the emission coefficient for bound-free transitions is found from:

$$j_\nu^e d\nu = \sum_{\text{final levels } l} \frac{1}{4\pi} h\nu_{ul} n_c d\nu \quad (3.57)$$

The complete expression is

$$j_\nu^e = \frac{128\pi^4}{3\sqrt{3}} \frac{Z^4 e^{10}}{m^2 c^3 h^2} N_+ N_e \left(\frac{m}{2\pi k T_e} \right)^{3/2} \sum_{n_{\min}}^{n_{\max}} \frac{1}{n^3} \exp\left(-\frac{h\nu - I + E_l}{k T_e}\right) \quad (3.58)$$

The lower limit on the summation corresponds to capture of a zero energy electron. n_{\min} is determined for each frequency by setting v to zero in Eq. 3.56. The upper limit is determined by ionization of the atom.

Free-Free Transitions

Free-free transitions are a special case in nonequilibrium because they involve only free electrons. Since electrons are assumed to equilibrate rapidly to some temperature T_e , Kirchhoff's law and the development of the emission coefficient lead to the same result.

$$j_\nu^e = \frac{8}{3} \left(\frac{2\pi}{3mkT_e} \right)^{1/2} \frac{Z^2 e^6}{mc^3} N_+ N_e \exp(-h\nu/kT_e) \quad (3.59)$$

3.2.2 Molecular Mechanisms

A “smeared band” expression can be developed for the molecular emission coefficient by a process parallel to that for absorption. The total emission in a rotational line, J_{ul}^e , is obtained from the Einstein coefficient for spontaneous emission:

$$J_{ul}^e = N_u A_{ul} h \nu_{ul} \quad (3.60)$$

The emission intensity at a particular frequency is obtained by dividing by the solid angle and introducing the line shape function, $F(\nu)$.

$$j_{\nu_{ul}}^e = \frac{N_u A_{ul} h \nu_{ul}}{4\pi} F(\nu) \quad (3.61)$$

Substituting Eq. 3.20 for the Einstein coefficient, this becomes

$$j_{\nu_{ul}}^e = N_u \frac{16\pi^3}{3c^2} \nu_{ul}^4 D_{elBA}^2 q_{v^u v^l} p_{J^u J^l} F(\nu) \quad (3.62)$$

To obtain the “smeared band” result, this expression must first be summed over J^l and the average frequency $\bar{\nu}_{Bv^u, Av^l}$ introduced. Using the summation rule for $p_{J^u J^l}$ this gives

$$j_{\nu_{Av^l, Bv^u J^u}}^e = N_{Bv^u J^u} \frac{16\pi^3}{3c^2} \bar{\nu}_{Bv^u, Av^l}^4 D_{elBA}^2 q_{v^u v^l} F(\nu) \quad (3.63)$$

Proceeding in parallel to the development for absorption, the sum over v^l is now carried out.

$$j_{\nu_{Av^l, Bv^u J^u}}^e = N_{Bv^u J^u} \frac{16\pi^3}{3c^2} D_{elBA}^2 F(\nu) \sum_{v^l} q_{v^u v^l} \bar{\nu}_{Bv^u, Av^l}^4 \quad (3.64)$$

where again the frequency remains inside this summation for accuracy. The average emission coefficient for a single rotational line is now obtained using the mean value

theorem.

$$\int_{line} j_{\nu_{A, B v^u J^u}}^e d\nu = \frac{16\pi^3}{3c^2} D_{elBA}^2 N_{B v^u J^u} \sum_{v^l} q_{v^u v^l} \bar{\nu}_{B v^u, A v^l}^4 = \bar{j}_{\nu_{A, B v^u J^u}}^e \Delta\nu \quad (3.65)$$

where $\Delta\nu$ is the width of the line.

This equation can now be solved for the rotationally averaged emission coefficient. The complete “smeared band” emission coefficient is then obtained by carrying out the summations over the final rotational and vibrational levels, J^u and v^u . The result is:

$$\bar{j}_{\nu_{AB}}^e = \frac{16\pi^3}{3c^2} D_{elBA}^2 \sum_{v^u} \sum_{v^l} q_{v^u v^l} \bar{\nu}_{B v^u, A v^l}^4 \sum_{J^u} \frac{N_{B v^u J^u}}{\Delta\nu} \quad (3.66)$$

As in the case for absorption, the infinite sums are truncated by the occurrence of dissociation.

The average frequency, $\bar{\nu}_{B v^u, A v^l}$, in Eq. 3.66 is the same as that for absorption, and is given by Eqs. 3.44 and 3.45 for non- Σ and Σ transitions, respectively. The average line spacing is also the same, and is given by the expression in Eq. 3.37 with the rotational quantum number expressed in terms of the wave number according to Eq. 3.38. The final term in the emission coefficient, the nonequilibrium upper level population, is found from the expression:

$$N_{B v^u J^u} = N_B \frac{\exp(-E_{v^u}/kT_v)}{Q_v(T_v)} \frac{g_{J^u} \exp(-E_{J^u}/kT_r)}{Q_r(T_r)} \quad (3.67)$$

where the vibrational and rotational energies are given as a function of wave number by Eqs. 3.10 and 3.39, evaluated for the upper energy level, and the electronic level population, N_B , is obtained from the QSS method. The evaluation of the partition functions was discussed in the section on absorption.

Substituting all these expressions in the emission coefficient, Eq. 3.66, the “smeared band” result is obtained:

$$\begin{aligned} \bar{j}_{\nu_{AB}}^e &= \frac{16\pi^3}{3c^2} D_{\epsilon l BA}^2 \sum_{v^u}^{\infty} \sum_{v^l}^{\infty} q_{v^u v^l} \bar{\nu}_{B_{v^u}, A_{v^l}}^4 \\ &\sum_{J^u}^{\infty} N_B \frac{\exp(-E_{v^u}/kT_v)}{Q_v(T_v)} \frac{2J^u + 1}{2cJ^u |B_{v^u} - B_{v^l}| Q_r(T_r)} \\ &\exp(-hc \left\{ \left[B_e^u - \alpha_e^u \left(v^u + \frac{1}{2} \right) \right] \left(\frac{1}{\lambda} - \frac{1}{\lambda_{v^u v^l}} \right) \frac{1}{B_{v^u} - B_{v^l}} \right. \\ &\quad \left. - \frac{4B_e^{u^3}}{\omega_e^{u^2}} \left(\frac{1}{\lambda} - \frac{1}{\lambda_{v^u v^l}} \right)^2 \frac{1}{(B_{v^u} - B_{v^l})^2} \right\} / kT_r) \end{aligned} \quad (3.68)$$

Again the approximation $2J^u + 1 \approx 2J^u$ is used inside the summation over J^u , to be consistent with the level of accuracy of the result.

3.3 Induced Emission

The above expressions for the emission coefficient do not include all the radiation emitted by the medium. Stimulated or induced emission also occurs due to the presence of photons. This emission is proportional to the radiative intensity, I_ν , and is therefore commonly included as a correction to the absorption coefficient. The induced emission is given by:

$$j'_\nu = j_\nu^e \frac{c^2}{2h\nu^3} I_\nu \quad (3.69)$$

In equilibrium the intensity, I_ν , in this equation becomes the Planck black body function, and the result of Eq. 3.47 is obtained. The absorption coefficient corrected for induced emission can then be identified in equilibrium from Eq. 3.47 as

$$\kappa'_\nu = \kappa_\nu(s)(1 - \exp(-h\nu/kT)) \quad (3.70)$$

In nonequilibrium, the intensity cannot be replaced with the Planck function. Instead, the induced emission coefficient of Eq. 3.69 must be substituted in the transport equation, along with the coefficients for spontaneous emission and induced absorption. The transport equation, Eq. 2.4, then becomes:

$$\frac{\partial I_\nu(s, \hat{\Omega}, t)}{\partial s} + \kappa_\nu(s) I_\nu(s, \hat{\Omega}, t) = j_\nu^e(s, t) + j'_\nu(s, t) \quad (3.71)$$

where j_ν^e is the spontaneous emission coefficient. Substituting Eq. 3.69 and gathering terms containing I_ν then allows the definition of a corrected absorption coefficient equal to the factor multiplying I_ν . The result is:

$$\kappa'_\nu = \kappa_\nu - j_\nu^e \frac{c^2}{2h\nu^3} \quad (3.72)$$

The corrected absorption coefficient may be negative in nonequilibrium. This fact must be carefully considered when developing any solution algorithm for radiative transport in nonequilibrium problems.

Negative values of κ'_ν occur when the nonequilibrium populations are such that the second term on the right-hand-side of Eq. 3.72 is larger than the first term. Physically, this means that the upper energy level of a transition or transitions is overpopulated relative to the lower energy level. Such a population inversion can occur in a nonequilibrium boundary layer, for instance, when the higher energy levels are still populated according to the temperature and chemistry of the inviscid shock layer. Because of the ν^{-3} term appearing in Eq. 3.72, negative values of κ'_ν tend to occur at the low energy end of the spectrum (see Fig. 5.3).

4 Transport Theory

Solving the equation of radiative transport (Eq. 2.4) in a tractable computation requires a number of approximations. It is not possible to consider an infinite number of frequencies or an infinite number of directions. Assumptions commonly made are a step-wise variation of radiation properties over part or all of the frequency spectrum, and a one-dimensional variation of the gas properties.

The first assumption may be acceptable in many situations, but must be used cautiously in nonequilibrium. The absorption coefficient in nonequilibrium cannot be found simply from temperature and equilibrium composition but depends on the population of excited states, and hence the chemical and excitation kinetics. This introduces a number of new variables and makes the design of a step absorption coefficient difficult. Some method of selecting appropriate frequencies at which to compute the radiative properties must be devised. This problem will be discussed in Ch. 5.

The second assumption of one-dimensional property variation should be nearly valid in the stagnation region of flows over blunt bodies. However, the results shown in Figs. 6b and 11 of Candler [4] suggest that even near the stagnation point this approximation may be in error. The assumption certainly introduces considerable error in the radiative flux at corners, and is not at all valid in the wake region of vehicles such as the proposed ASTV. Such wake flows are of great interest, because of

the desire to place unshielded payloads in the lee of these vehicles for orbit transfer.

4.1 Flowfield Coupling

Including gas radiation effects in a thermochemical nonequilibrium flowfield calculation means including the coupling between the fluid dynamics and the radiation. The coupling occurs because of the radiative flux term $\nabla \cdot \vec{q}_R$ (denoted Q_{rad} by Gnoffo [69]) which appears in the total and vibrational-electronic energy conservation equations. In the tangent slab approximation, the divergence of the radiative flux reduces to simply the normal derivative of q_R . The appropriate term is obtained from the radiative transport solution as discussed below for each solution method considered.

4.2 Plane-Parallel Medium

A common approximation for solving the radiative heat transfer equation is to assume that the medium through which the radiation travels varies in only one direction. This is often a reasonable assumption in the stagnation region of a flowfield, as well as in other geometries which are of interest for radiant heating. In this situation the path variable s can be replaced by the Cartesian coordinate y using the chain rule:

$$\frac{\partial}{\partial s} = \frac{\partial}{\partial x} \frac{dx}{ds} + \frac{\partial}{\partial y} \frac{dy}{ds} + \frac{\partial}{\partial z} \frac{dz}{ds} \approx \frac{\partial}{\partial y} \frac{dy}{ds} \quad (4.1)$$

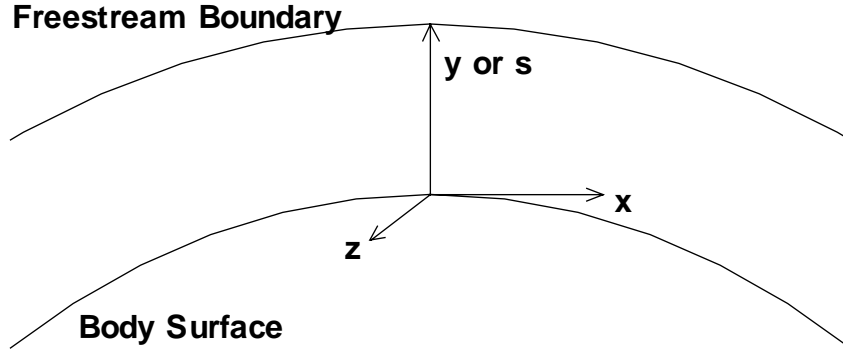


Figure 4.1. Shock Layer Geometry for Plane-Parallel Approximation

For a shock layer geometry, if both s and y are taken along the surface normal direction as shown in Fig. 4.1 then

$$\frac{\partial}{\partial s} = \frac{d}{dy} \quad (4.2)$$

Equation 2.4 then becomes

$$\frac{dI_\nu(y, t)}{dy} + \kappa'_\nu(y)I_\nu(y, t) = j_\nu^e(y, t) \quad (4.3)$$

This is the equation of radiative transfer along the y -axis in a plane-parallel medium under conditions of nonequilibrium.

4.2.1 Transparent Gas

A transparent gas is one in which the absorption coefficient is assumed zero. In this case, Eq. 4.3 can be further simplified to obtain:

$$\frac{dI_\nu(y, t)}{dy} = j_\nu^e(y, t) \quad (4.4)$$

This equation can easily be integrated to find

$$I_\nu(y, t) = \int_{y_0}^y j_\nu^e(y, t) dy \quad (4.5)$$

For a solution over a flowfield grid, in which the emission coefficient is known at a number of discrete points, this equation can be solved by any numerical quadrature method. For a transparent gas, the radiative flux \vec{q}_R can be found simply by multiplying the intensity by 2π . The divergence of \vec{q}_R , needed for coupling to a flowfield, can be obtained by numerical differentiation. Despite the assumption that the gas does not absorb radiation, this term will be nonzero due to emission from the gas.

4.2.2 Absorbing Gas

For an absorbing gas Eq. 4.3 can be integrated formally to obtain an expression for the radiative intensity for any location y . This has been done in equilibrium for instance by Ozisik [21, p. 267]. It is convenient to split the intensity into two components: one directed along $+y$, denoted I_ν^+ , and the other along $-y$, denoted I_ν^- . Ozisik's equations can be adapted to the nonequilibrium situation by recognizing that the source function, S_ν , in a non-scattering nonequilibrium gas becomes j_ν^e/κ'_ν . The formal solution for these two components of the radiative intensity can then be written for the nonequilibrium problem as:

$$I_\nu^+(\tau_\nu) = I_\nu^+(0)e^{-\tau_\nu} + \int_0^{\tau_\nu} \frac{j_\nu^e(\tau'_\nu)}{\kappa'_\nu(\tau'_\nu)} e^{-(\tau_\nu - \tau'_\nu)} d\tau'_\nu \quad (4.6)$$

$$I_\nu^-(\tau_\nu) = I_\nu^-(\tau_{0\nu})e^{-(\tau_{0\nu} - \tau_\nu)} + \int_{\tau_\nu}^{\tau_{0\nu}} \frac{j_\nu^e(\tau'_\nu)}{\kappa'_\nu(\tau'_\nu)} e^{-(\tau'_\nu - \tau_\nu)} d\tau'_\nu \quad (4.7)$$

where τ_ν is the optical variable defined for each frequency ν as

$$\tau_\nu = \int_0^y \kappa'_\nu(y) dy \quad (4.8)$$

The $\tau_\nu = 0$ boundary is the vehicle surface, which is assumed to emit radiation according to Planck's function at the wall temperature T_w . A radiation equilibrium wall temperature can be computed for this purpose, but in this analysis T_w is assumed to be given. The $\tau_\nu = \tau_{0\nu}$ boundary is the freestream gas ahead of the vehicle. The radiative intensity emanating from the freestream is assumed to be zero. The second equation therefore reduces to:

$$I_\nu^-(\tau_\nu) = \int_{\tau_\nu}^{\tau_{0\nu}} \frac{j_\nu^e(\tau'_\nu)}{\kappa'_\nu(\tau'_\nu)} e^{-(\tau'_\nu - \tau_\nu)} d\tau'_\nu \quad (4.9)$$

Nicolet [24] assumed a log-linear variation of properties to solve these equations. This formulation does not accommodate negative values of κ'_ν , the absorption coefficient corrected for induced emission, which can occur in nonequilibrium. Nicolet's transport algorithm can therefore not be used here. As in the transparent gas case, any numerical quadrature method can be used to obtain the radiative intensity distribution along the body normal, but it must allow for negative κ'_ν .

To obtain the radiative flux in an absorbing, plane parallel medium it is easy to show that the above equations apply with the simple replacement of τ_ν by $2\tau_\nu$ and the addition of a factor of π . The net radiative flux is then given by

$$q_{\nu R}(\tau_\nu) = \pi \left\{ I_\nu^+(0) e^{-2\tau_\nu} + \int_0^{\tau_\nu} \frac{j_\nu^e(\tau'_\nu)}{\kappa'_\nu(\tau'_\nu)} e^{-2(\tau_\nu - \tau'_\nu)} d(2\tau'_\nu) - \int_{\tau_\nu}^{\tau_{0\nu}} \frac{j_\nu^e(\tau'_\nu)}{\kappa'_\nu(\tau'_\nu)} e^{-2(\tau'_\nu - \tau_\nu)} d(2\tau'_\nu) \right\} \quad (4.10)$$

The divergence of the radiative flux is obtained by differentiating this equation with

respect to y , then integrating over the complete spectral range. The result is:

$$\frac{\partial q_R}{\partial y} = \int_{\nu_{\min}}^{\nu_{\max}} \left\{ -2\pi \kappa'_\nu(\tau_\nu) \left[I_\nu^+(0) e^{-2\tau_\nu} - 2 \frac{j_\nu^e(\tau_\nu)}{\kappa'_\nu(\tau_\nu)} + \int_0^{\tau_\nu} \frac{j_\nu^e(\tau'_\nu)}{\kappa'_\nu(\tau'_\nu)} e^{-2|\tau_\nu - \tau'_\nu|} d(2\tau'_\nu) \right] \right\} d\nu \quad (4.11)$$

where τ_ν is a function of y . For a solution including all the radiative energy, ν_{\min} is zero and ν_{\max} is infinity. In practice, finite limits on the spectral integration will be required. Most gas radiation in shock layers in air occurs at energies below 16.5 eV. An alternate upper limit at 6.2 eV includes only the visible and infrared portions of the spectrum. This range of energies is easier to measure experimentally and includes minimal self-absorption. The lower limit is often set around 0.3 eV because a zero energy photon causes a singularity in the free-free absorption coefficient (Eq. 3.9). The singularity arises because additional quantum mechanical considerations must be included at very low energies. The radiative energy omitted by ignoring these low energies is minimal.

4.3 Multi-Dimensional Medium

Since an exact solution of the radiative transport equations in multi-dimensional media is not feasible, an approximate method is sought. Such a method should introduce considerable simplifications to the governing equations in keeping with the stated objective of providing a relatively fast solution. Numerous approximate methods are available in the literature. A brief summary was provided in the topical review in Ch. 2. The best-developed of these methods are the moment methods, which reduce

the problem from a solution of integro-differential equations to a solution of simpler ordinary differential equations. Many of these methods have been developed specifically for one-dimensional radiative transport. Sparrow and Cess [70, Sec. 7-9] caution that the extension to three dimensions is open to question and must be made with caution. They also show, however, that the moment method reduces to the correct expressions in the limit of optically thin or optically thick gases and suggest that it should therefore be of reasonable accuracy for all values of optical thickness. Modest has modified the differential approximation to make it even more accurate for small optical depths and generalized it for the three-dimensional case. His method gives results of excellent accuracy for all optical conditions [27]. It is adapted below for the current non-gray, nonscattering, and nonequilibrium flow.

As previously mentioned, the source function in a nonequilibrium, nonscattering medium is

$$S_\nu = \frac{j_\nu^e}{\kappa'_\nu} \quad (4.12)$$

The definitions of the incident intensity and flux are repeated here for convenience:

$$G_\nu(\vec{r}) = \int_{4\pi} I_\nu(\vec{r}, \hat{\Omega}) d\omega \quad (4.13)$$

$$\vec{q}_{\nu R}(\vec{r}) = \int_{4\pi} I_\nu(\vec{r}, \hat{\Omega}) \hat{\Omega} d\omega \quad (4.14)$$

In what follows the R subscript on $\vec{q}_{\nu R}$ will be dropped. The intensity is now divided into two separate contributions: one due to the emission from the medium, I_m ; and the other traceable to the wall emission, I_w : $I(\vec{r}, \hat{\Omega}) = I_w(\vec{r}, \hat{\Omega}) + I_m(\vec{r}, \hat{\Omega})$. The incident intensity and flux will then also have two components: $G = G_w + G_m$ and

$\vec{q} = \vec{q}_w + \vec{q}_m$. While the intensity attributable to the wall may be highly directional, that emanating in the medium should vary quite smoothly. This portion is therefore assumed to be given by the P-1 approximation, which is the simplest form of the moment method. In this case, the medium intensity can be expressed as

$$I_m \approx \frac{1}{4\pi}(G_m + 3\vec{q}_m \cdot \hat{\Omega}) \quad (4.15)$$

This expression is unchanged from the work of Modest [27]. The equation governing the medium intensity then becomes

$$\nabla \cdot (\hat{\Omega} I_{\nu_m}) = j_\nu^e - \kappa'_\nu I_{\nu_m}(\vec{r}, \hat{\Omega}) \quad (4.16)$$

where the nongray, nonscattering, nonequilibrium nature of the gas has been accounted for. Taking the zeroth and first moments of this equation and integrating over 4π steradians yields the applicable governing equations for G_ν and \vec{q}_ν of the medium:

$$\nabla \cdot \vec{q}_{\nu_m} = 4\pi j_\nu^e - \kappa'_\nu G_{\nu_m} \quad (4.17)$$

$$\nabla G_{\nu_m} = -3\kappa'_\nu \vec{q}_{\nu_m} \quad (4.18)$$

The details of the numerical solution to these equations are given in Appendix B.

To obtain the divergence of the radiative heat flux, which is required to couple the solution with the flowfield, the contribution to \vec{q} from the walls must also be considered. This is obtained from the following integral:

$$\vec{q}_{\nu_w} = \frac{1}{\pi} \int_{4\pi} B_\nu[\vec{r}'(\omega)] e^{-\tau_\nu} \hat{\Omega} d\omega \quad (4.19)$$

where the wall radiosity, B_ν , is given by the sum of emission at the wall temperature T_w , and reflection of radiation emanating from other wall surfaces. In Modest's analysis, the wall reflection is assumed to be diffuse. The treatment of specularly reflecting wall surfaces adds considerably to the complexity of the problem and will not be addressed here. In any case, for a forebody flowfield the wall surface is convex so that no reflection of radiation emitted by the wall can occur. Then the radiosity is simply the emission from the wall:

$$B_\nu(\vec{r}) = \varepsilon_\nu \pi I_{\nu p_w}(\vec{r}) \quad (4.20)$$

This contribution to the radiative flux must be computed for each grid cell in the medium by integration over all the wall surface elements to which it has a line of sight. If it is further assumed that the wall is cold, or that it makes a negligible contribution, then $\vec{q}_w \approx 0$, and only the medium contribution need be considered. This approximation is not unreasonable for aeroassist flowfields, since heating rates are relatively low in the upper atmosphere and the wall temperature will accordingly be relatively low during much of the flight. In fact, at the maximum wall temperature predicted for the Aeroassist Flight Experiment (AFE), the peak of the black body emission spectrum occurs at about 0.75 eV. This temperature is close to the limit achievable for reusable surfaces using Space Shuttle-type thermal protection system tiles, and so is representative of the maximum wall temperature to be expected for a non-ablating surface. For lower temperatures, the peak shifts to even lower energies. In this low energy spectral region the gas is quite transparent to radiation (see

Fig. B.1) so the wall can have little effect on the divergence of the radiative flux. In that case, $\nabla \cdot \vec{q}_R \approx \nabla \cdot \vec{q}_m$ and is obtained by integrating Eq. 4.17 over frequency. Note that unlike the plane-parallel medium, numerical differentiation is not required here.

Boundary conditions in the multi-dimensional case are less obvious than for the plane parallel approximation. It may again be assumed that the radiative intensity emitted in the freestream is zero. Even in a three-dimensional flowfield, however, symmetries are generally exploited. This means that some grid boundaries will be symmetry planes. Others will be outflow boundaries. Symmetry planes can be treated with reflecting boundary conditions, but the treatment of outflow boundaries is ill-defined. The conditions of the gas are not known beyond such boundaries, though it is expected to continue radiating for some finite distance for most flight conditions of interest. The treatment of outflow boundaries is discussed further in Sec. 6.2.1 and Appendix B.

For the medium intensity, the vehicle surface is considered to be a cold wall, for which Marshak's boundary condition [21] for the P-1 method is

$$2 \left[\frac{2}{\varepsilon_\nu} - 1 \right] \vec{q}_\nu \cdot \hat{n} + G_\nu = 0 \quad (4.21)$$

The flux, if any, impinging on a wall surface due to emission or reflection from other wall surfaces must be obtained by an integration which considers the view factors of the particular problem. When the wall is convex, this contribution is zero. The numerical details of the treatment of the boundary conditions are given in Appendix B.

5 Implementation

The implementation of the theory for radiation transitions and radiative transport developed in the previous two chapters in a practical computer code requires some additional work. The details of the process are described in this chapter.

5.1 Coding

The present method is implemented in the LORAN (Langley Optimized RAdiative Nonequilibrium) code, which was developed using two existing codes as starting points. The RAD/EQUIL program [33] was followed in developing some of the code structure. It also is the source of part of the algorithm used to model atomic line radiation. The quasi-steady-state (QSS) excitation portion of the NEQAIR program [20] has been minimally adapted for use in LORAN.

LORAN is divided into four major sections: reading data and setting up properties which are constant for a calculation, calculating the nonequilibrium excitation, evaluating the radiative properties, and solving the radiative transport problem.

5.1.1 Initial Setup

Data Input

To evaluate the expressions for absorption and emission obtained in Ch. 3 for each of the radiating mechanisms, input values are required. Data are also required to predict the nonequilibrium populations of the various bound energy levels. Flowfield

data are required to define the local gas conditions. Finally, program control inputs are desirable to maximize the flexibility of the method without requiring constant reprogramming and recompiling. These should allow the user to turn individual radiating mechanisms or species on or off to perform detailed studies of the radiation spectrum. They should also provide for selection of options in the code (i.e. tangent slab vs. 3-D transport). These inputs are obtained from a variety of sources, as discussed below. Most of the inputs are species properties and will not change unless significantly different new data become available.

Flowfield Data

The information required about the gas conditions consists of the number densities of each of the radiating species considered and temperatures for the several energy modes. The Langley Aerothermodynamic Upwind Relaxation Algorithm (LAURA) flowfield solver [71] is the source of the flowfield data used in developing this method. It is an 11-species model which provides number densities for all the nitrogen/oxygen radiating species of interest. LAURA currently incorporates a two-temperature model for thermal nonequilibrium [72]. The rotational and heavy particle translational energy modes are assumed to be equilibrated, while the vibrational and electron translational energy modes are assumed to be in equilibrium with each other but not necessarily with the other modes. This means that the separate T_v and T_e carried in the development of the absorption and emission coefficients are equal, as are T_r and T_t . The distinction between these temperatures was maintained in LORAN, however,

so that each can be used if the separate temperatures become available from LAURA or another Computational Fluid Dynamics (CFD) code in the future. Some recent work [73] suggests further that distinct vibrational temperatures may exist for each molecular species. Should a CFD code ever include such detail, minor modifications to LORAN will allow these individual T_v values to be used.

An effort has been made to keep the input of the flowfield properties from LAURA generic, so that with minor changes to a single subroutine LORAN can be interfaced with a different CFD code.

Maximum Rotational Quantum Number

The radiative property data discussed above are read into the program first. As part of this process, the maximum rotational quantum numbers are assessed using the algorithm developed by Whiting (see Sec. 3.1.2). These values do not change in the program.

Continuum Spectrum

The spectral location of all radiating transitions is determined from the set of energy levels in the atoms and molecules appearing in the gas. This information can be used to select a minimum set of spectral points for use in the radiation calculation.

Consider the bound-free continuum. The absorption coefficient for this mechanism is a smooth function of frequency with discontinuities corresponding to the activation of additional energy levels. To resolve this spectrum, spectral points must be

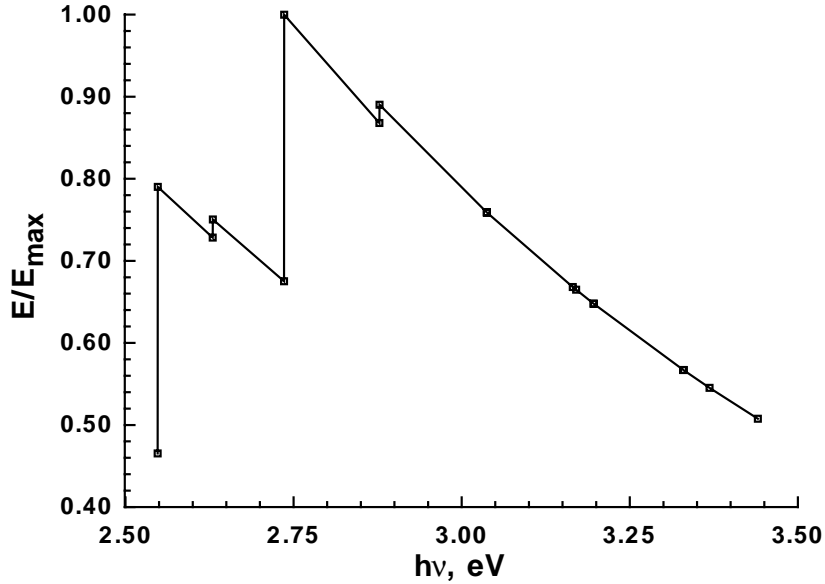


Figure 5.1. Example of Spectrum Optimization for Bound-Free Continuum

placed within a very small interval on either side of each jump, as shown in Fig. 5.1. However, this interval is much smaller than what is needed for the smooth portions of the curve. RAD/EQUIL took advantage of this fact by allowing the user to input a few spectral points to capture the jumps. In LORAN, this procedure is automated and incorporated in the radiation calculation. For the particular set of atomic species considered in a computation, a tailored atomic spectrum is generated to resolve the active discontinuities, as the figure illustrates. This simplifies the inputs and eliminates the chances of omitting a level. It also allows the atomic continuum calculation to be performed on the minimum resolving array of spectral points.

As discussed in Ch. 3, the molecular radiation has been modeled here using the “smeared band” approximation. In this approximation, the rotational structure is

smoothed into an exponential variation. To resolve the resulting spectrum, spectral points must be placed around each vibrational band head. A few points are sufficient to capture the smoothed rotational variation within each such band. The resulting structure is similar to the bound-free spectrum, though it is much more complicated because the vibrational bands are far more numerous and often overlap each other. These considerations have been used to develop a routine to choose an optimum molecular spectrum for each input spectral range and set of active species.

For each active species, the vibrational band heads that occur in the spectral range under study are computed from Eq. 3.36 with $J = 0$. An initial spectrum is generated by resolving the band head and spacing nv points in the interval between the zero rotational level ($J = 0$) and the maximum rotational level ($J = J_{max}$). An example for a major vibrational band of N_2^+ is given by the curve labeled “initial spectrum” in Fig. 5.2. Note that the clustering of points along this curve results from additional weaker bands which underlie this major band. Since the absorption coefficient decreases rapidly for a given vibrational band (note the log scale in the figure), this spectrum can be reduced. This is done by discarding points that describe a vibrational band away from its band head (points required to resolve the jump are kept), if they are within a given interval *crit* of another point. This procedure can reduce the spectral array by nearly an order of magnitude. A second reduction can be made by discarding *any* point which has a neighbor within a smaller interval *crit2*. Applying these steps to the spectrum in Fig. 5.2 results in the optimized

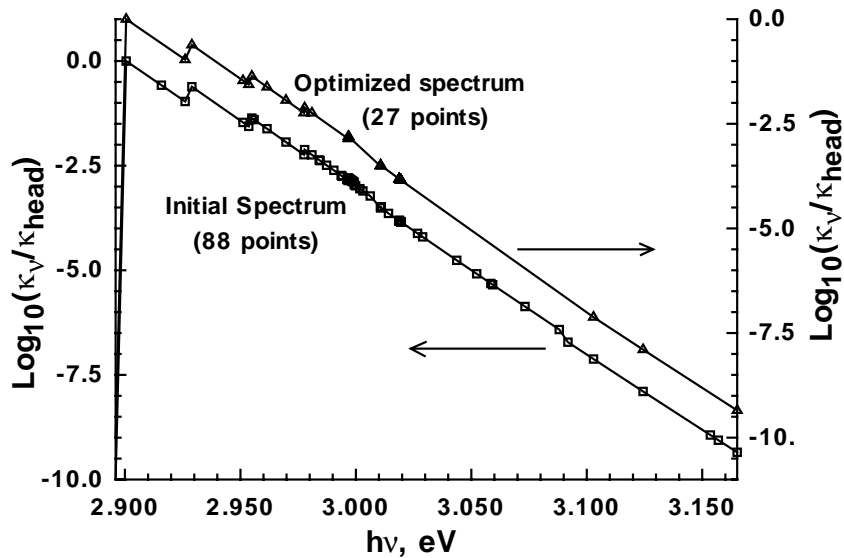


Figure 5.2. Example of Spectrum Optimization for a Vibrational Band

spectrum shown. Applying them to the entire set of vibrational bands, a spectrum can be generated that resolves the molecular transitions using less than 2000 points and that is optimized for whatever species and spectral range have been requested. This calculation is computationally expensive, since it sifts through a large number of possible spectral points to produce the optimized molecular spectrum, and it is therefore only exercised once per run. The resulting spectrum is stored for all further computations. Appropriate selection of the parameters *nv*, *crit*, and *crit2* controls the amount of detail included in the molecular spectrum and its size.

Once an optimized spectrum is obtained, the index of the first and last spectral point for each vibrational band is determined. These indices simplify the logic required in computing the molecular band radiation, and improve its efficiency.

A few (about 50) points from the optimized molecular spectrum that resolve strong vibrational transitions are identified and interleaved into the atomic continuum spectrum discussed above. The resulting spectrum of about 150 points will be referred to as the modified atomic spectrum. Its use is discussed in Sec. 5.1.4.

5.1.2 Nonequilibrium Excitation

To obtain the nonequilibrium electronic level populations for the atoms and molecules in the flowfield, data on the rates of excitation and deexcitation of each level are required. Sources for this data are varied, but the rates presented are often uncertain due to the experimental difficulties involved in their measurement. Park [20] has collected a complete set of rates for nitrogen and oxygen species which has been adopted here.

The nonequilibrium excitation calculation in the present method was taken from Park's NEQAIR program. It consists of a QSS solution to the set of excitation rate equations, in which it is assumed that the rate of change in a level's population is small compared to the rate of transitions into and out of that level [67, Chapter 3]. This method is designed for use in situations where the amount of nonequilibrium is "not too large". Its most serious weakness in the present application is that it does not account for the history of the flow in areas of high gradients (boundary layer and shock).

The excitation calculation depends on excitation rate data for the various energy levels. This type of data is rather difficult to obtain and therefore has a significant

level of uncertainty. Park [3] cites this uncertainty as a factor of two, and asserts that the impact on the excited state populations is negligible. Further verification of this accuracy would be desirable in the future.

5.1.3 Radiation Properties

Bound-Bound Mechanisms

For bound-bound transitions the oscillator strengths f_{lu} , line centers ν_{CL} and Stark (half) half-widths γ^S are needed. The National Bureau of Standards (NBS) has published a large number of line centers and oscillator strengths [66], while Stark (half) half-width information is available from Griem [63], among others. In addition, the energy levels and degeneracies of the upper and lower levels of the transitions can be found in the NBS compilation.

In the RAD/EQUIL code, Nicolet approximated the so-called high series lines by an integral. These lines have lower state quantum numbers of four or greater, and are numerous and closely spaced at energies below 3.2 eV. Park treats each of these lines individually in NEQAIR. In the present method, in order to reduce the number of lines computed and therefore the run time, the high series lines were represented by multiplet-averaged values. Data for these averaged lines were obtained from the NBS tables, for transitions corresponding to Park's inputs. This approximation should have minimal impact on the results, and yet allows the number of lines treated to be reduced by more than half.

The line shape models for LORAN are taken from the development by Nicolet

[23] as implemented in the RAD/EQUIL code [33]. This includes natural, Doppler, resonance, and Stark broadening of the atomic lines, as discussed in Ch. 3. Lorentz or Doppler line shapes are selected depending which line width is larger. Each line is resolved by a small number $nppl$ (generally less than or about 15) of spectral points that are distributed starting from the line center (see Fig. 3.1). The location of the spectral point farthest from the line center is determined from the width of each atomic line. In Nicolet's implementation the line width used to distribute these points was an approximation to the maximum width in the gas layer so that all or most of the energy in each line would be included. This approximate maximum width was calculated at a location input by the user at which the maximum temperature was expected.

For an application in which a complete flowfield is to be computed, the identification of the occurrence of maximum line width presents some difficulties. Further, since the line width may vary by orders of magnitude between various points in a flowfield, the use of a spectrum geared to the largest width can result in significant loss of accuracy. For these reasons, the routine which sets up the line frequency spectrum (subroutine *freq* of RAD/EQUIL) has been modified to be applied to every point in the flowfield. This results in the specification of a local set of spectral points based on the local line width. These disparate frequency spectra are then reconciled to generate a single atomic line spectrum. This process results in the selection of a set of spectral points capturing the energy in a line at its broadest, but involving

detailed spectral information at each grid point. This technique allows satisfactory resolution of the atomic lines, without requiring an excessive amount of storage or computation.

An additional change made to Nicolet’s method arises because Stark broadening is not always the dominant effect on line width. In the original RAD/EQUIL, the point distribution logic in subroutine *freq* considered only the Stark line width. In the present model, the largest of the Doppler and Lorentz (Stark effect) line widths is used. While this is a small change, it should result in more complete coverage of the atomic line radiation in the present model.

The RAD/EQUIL method has also been modified to use nonequilibrium excited state populations and electron temperature, where appropriate. The Doppler line width remains a function of heavy particle temperature, since it arises from the thermal motion of the atoms themselves.

Bound-Free Mechanisms

Computing the radiation from atomic mechanisms requires knowledge of the energy levels of each atomic species. The large number of electronic energy levels in Eq. 3.8 must be modeled by a manageable set of inputs. To reduce book-keeping and complexity, a common practice is to group neighboring energy levels into one, with an appropriate overall degeneracy. This practice has been adopted here. The grouped levels from Park’s QSS method [20] are used for nitrogen and oxygen atoms (twenty-two levels for atomic nitrogen, nineteen levels for atomic oxygen). The re-

quired values for the principal quantum number n and the energy level E_n for each of these levels is input.

The bound-free photoionization edge structure is produced by the activation of each level in the summation term of Eq. 3.8. This requires determining the lowest accessible bound energy level, n^* , for each spectral point in the atomic continuum spectrum. The ground state cross sections are invoked as constants to avoid the errors arising from the hydrogenic model, as discussed in Ch. 3. Each of the atomic energy levels is treated individually in the bound-free calculation, but since these are grouped levels many more energy levels are in fact approximately included.

Free-Free Mechanisms

LORAN considers only the radiation produced by an electron slowed by the presence of an atomic ion. The free-free radiation produced by the proximity of a neutral atom or a molecule is considered negligible. The free-free contribution is computed on the same spectrum as the bound-free radiation. The resolution thus obtained is more than sufficient, and allows the two atomic continuum processes to be easily combined.

Molecular Mechanisms

To predict the molecular band radiation, spectroscopic constants describing the distribution of rotational and vibrational energy levels according to Eqs. 3.11 and 3.10 must be provided. These can be found in a number of sources, such as Herzberg [65], Bond et al. [74], and many others. These sources also provide the necessary informa-

tion on the electronic energy levels and energy level degeneracies in molecules. The intensity of radiation depends on the Frank-Condon factors $q_{v^u v^l}$ and the electronic transition moments D_{elBA} . Data on these quantities may be found in many often contradictory sources. The complete set of molecular inputs collected by Park for his NEQAIR code [20] has been adopted here for simplicity.

The molecular band radiation is computed using the optimized molecular spectrum whose determination was discussed in Sec. 5.1.1. The expressions for the emission and absorption coefficients developed in Ch. 3 have many terms in common. Advantage is taken of this fact to reduce the computation time required. Since the molecular calculation remains one of the more expensive parts of the radiation calculation, care was taken in programming this particular mechanism to ensure that the advantages of vectorization are exploited to the extent possible.

5.1.4 Radiative Transport

Two distinct methods to compute radiative transport were developed in Ch. 4, with and without the tangent slab approximation. Both employ an approximate treatment of atomic lines based on the method of RAD/EQUIL. A single mean value of the continuum (atomic continuum plus molecular band) absorption and emission coefficient is computed for each line and added to the detailed absorption and emission coefficients calculated at the $nppl$ points describing the line. These mean values are obtained by interpolating the information in the optimized continuum spectra, thus avoiding an expensive computation at each of the $nppl$ spectral points describing

each line. Since each atomic line covers only a very small part of the spectrum (see for instance Fig. B.1), this approximation should introduce minimal inaccuracy. Radiative transport is then computed at all $nppl$ spectral points describing each line. This detailed result can be integrated over frequency to provide an average flux for each line if a concise presentation is desired, or it can be presented in full detail.

The molecular spectrum can be averaged to obtain values at each point in the much smaller modified atomic continuum spectrum, so that the number of spectral points for which transport must be calculated is significantly reduced. Since these approximate results are based on a detailed molecular spectrum of both emission and absorption, the prediction of molecular radiation transport should be quite accurate. This averaging technique has been used for the full flowfield solutions reported in Ch. 6 to reduce the computation time. For those cases in which only the stagnation line is computed, the complete optimized molecular spectrum is used in the transport calculation.

Tangent Slab

The numerical integration of the transport equation simplified for the case of one-dimensional radiation (Eq. 4.3) is straightforward, with one exception. The method used by Nicolet in the RAD/EQUIL code assumes a log-linear variation of the absorption coefficient between grid points [24]. As mentioned in Sec. 3.3, under nonequilibrium conditions there is no longer any assurance that the absorption coefficient corrected for induced emission, κ'_ν , will be positive. The log-linear variation assumed

by Nicolet cannot handle a negative κ'_ν . For this work, a simple linear variation between grid points is used instead.

Multi-Dimensional Transport

The details of the modified differential approximation used to solve the radiative transport equation for multi-dimensional media are discussed in App. B, along with related numerical considerations. When κ'_ν is not positive, numerical instabilities have been observed in this method. Further work is needed to determine whether these instabilities can be removed. For now, spectral points at which these instabilities occur are ignored. Figure 5.3 is a plot of the number of occurrences of a negative κ'_ν in a test flowfield at each point in the radiation spectrum. It shows that significant numbers of negative κ'_ν only occur for a few points in the low energy end of the spectrum. The effect on predictions of wall radiative flux from ignoring these few spectral points will be quite small (see Ch. 6).

It should also be pointed out that the occurrence of these negative values of κ'_ν is controlled by the nonequilibrium excitation calculation. As mentioned before, this calculation contains significant uncertainties. An example of a population distribution at a point with negative κ'_ν is shown in Fig. 5.4 (an equilibrium distribution would appear as a straight line in this figure). This population distribution is quite odd, with neighboring energy levels having populations different by many orders of magnitude, and may be due to uncertainties in excitation rates. It is possible, therefore, that at least some of the negative κ'_ν values result from uncertainties in the excitation

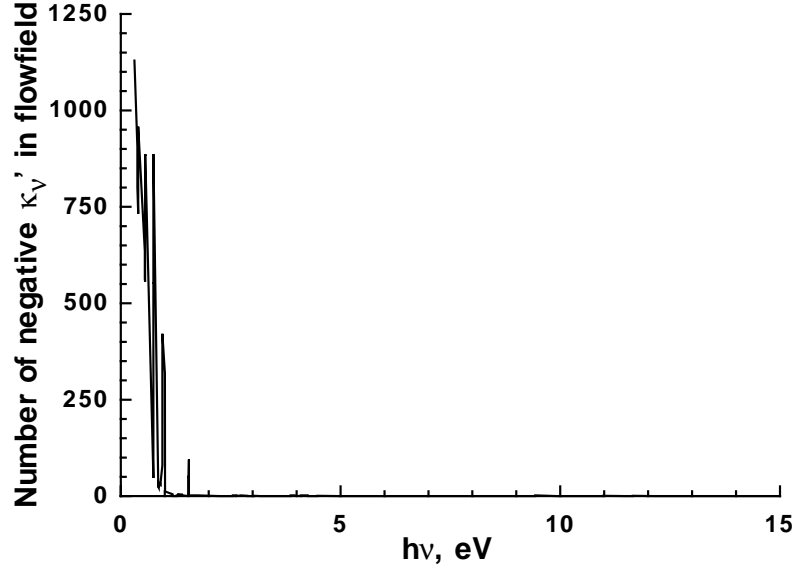


Figure 5.3. Occurrence of Negative κ'_ν in a Test Flowfield

calculation. Ignoring these spectral points may therefore introduce less error than including them.

5.2 Computational Optimization

Obtaining radiation predictions for complete flowfields, or coupling radiation and flowfield solutions, requires that the radiation calculations be carried out many times. In order to make this practical and to minimize the cost, it is desirable to optimize the radiation program, and to determine the minimum set of calculations which will provide an accurate radiation prediction. Methods of achieving this are discussed below.

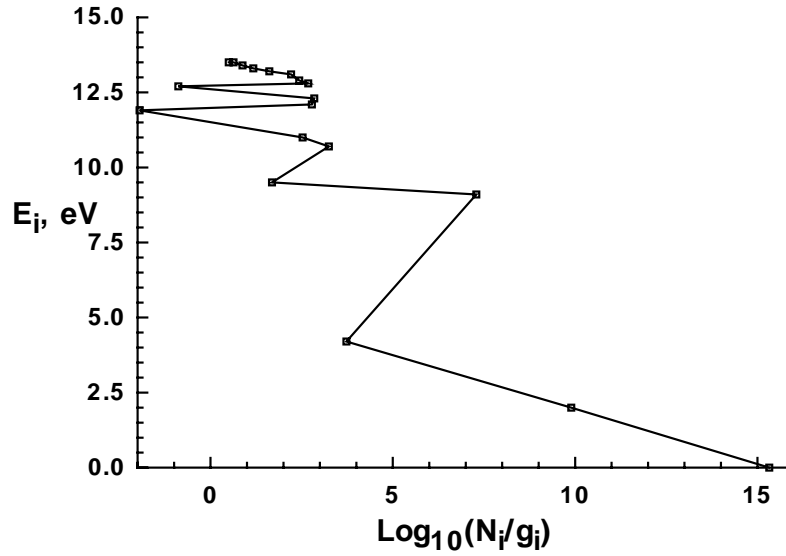


Figure 5.4. Nonequilibrium Population of Excited States of O for Negative κ'_ν

5.2.1 Radiation Calculation

Parametric studies were conducted to determine the spectral resolution required for acceptable accuracy in the predicted radiation. Variables whose effect was studied include na , the number of points allowed in the atomic continuum spectrum; $nppl$, the number of points resolving an atomic line; and the several variables which control the generation of the spectrum for molecular band radiation (nv , $crit$, $crit2$).

Tables 5.1-5.3 summarize the findings of this optimization process. The baseline against which the flux calculation is judged (first line of each table) is a detailed spectrum case with $na = 1500$, $nppl = 15$, $nv = 10$, $crit = 0.00825$ eV, and $crit2 = 0.0011$ eV. While uncertainties in the radiation calculation mean that this prediction is not necessarily right, such a detailed spectrum does provide the best result possible. The run

times are judged against a case with $na = 100$ and all other values unchanged (second line of each table). The transport time appearing in column 4 is the time required for tangent slab transport. Relative time savings for the modified differential approximation should be similar. Alternate values tested for these parameters are given in the first column of the tables. The designations C1 and C2 refer to combinations of the alternate values as follows: C1 has $na = 75$, $nppl = 11$, $nv = 8$, $crit = 0.0165$ eV, and $crit2$ unchanged; C2 is the same as C1 except $na = 100$. Three flight conditions identified as Cases A, B, and C, were studied to obtain results over a wide range of nonequilibrium conditions. These cases are described in further detail in Ch. 6 and 7.

As shown in Tables 5.1-5.3, the prediction of the radiative flux is affected by less than 5 percent for each set of parameters, except for two occurrences in Case C (see column 2). These are both attributable to setting $na = 75$. The potential savings in computational time are considerable. Based on these results, it is determined that the parameter set denoted C2 ($na = 100$, $nppl = 11$, $nv = 8$, $crit = 0.0165$ eV, and $crit2 = 0.0011$ eV) is appropriate for use in the radiation model. Increasing $crit2$ in line with the changes in the other parameters was found to have no effect, so results are not presented here.

5.2.2 Excitation Calculation

The last column in Tables 5.1-5.3 shows the fraction of CPU time used by the radiation and transport calculations. The remainder is required to obtain the nonequi-

Table 5.1. Computational Optimization - FIRE II at 1631 sec

| Case | Flux | CPU time for Radiation | CPU time for Transport | CPU Fraction |
|-------------|-------|---------------------------|---------------------------|-----------------|
| Baseline | 0.508 | 6.116 | 1.735 | 0.50 |
| $na = 100$ | +0.8% | 3.561 | 0.895 | 0.37 |
| $nppl = 11$ | +0.9% | -13.5% | -29.7% | 0.33 |
| $na = 75$ | +0.8% | -1.6% | -2.1% | 0.36 |
| $nv = 8$ | +1.4% | -0.3% | -0.8% | 0.37 |
| $crit * 2$ | +0.8% | -0.9% | -0.7% | 0.37 |
| C1 | +1.4% | -14.9% | -30.8% | 0.32 |
| C2 | +1.4% | -26.6% | -29.5% | 0.30 |

Table 5.2. Computational Optimization - FIRE II at 1634 sec

| Case | Flux | CPU time for Radiation | CPU time for Transport | CPU Fraction |
|-------------|-------|---------------------------|---------------------------|-----------------|
| Baseline | 22.50 | 10.843 | 3.059 | 0.69 |
| $na = 100$ | +2.1% | 6.326 | 1.714 | 0.57 |
| $nppl = 11$ | +3.6% | -13.0% | -29.3% | 0.52 |
| $na = 75$ | +2.5% | -1.1% | -1.6% | 0.56 |
| $nv = 8$ | +2.6% | +0.1% | -0.1% | 0.57 |
| $crit * 2$ | +2.1% | -0.6% | -0.8% | 0.57 |
| C1 | +4.5% | -14.8% | -30.7% | 0.52 |
| C2 | +4.1% | -26.0% | -29.3% | 0.49 |

Table 5.3. Computational Optimization - FIRE II at 1637.5 sec

| Case | Flux | CPU time for Radiation | CPU time for Transport | CPU Fraction |
|-------------|-------|---------------------------|---------------------------|-----------------|
| Baseline | 292.9 | 10.061 | 2.913 | 0.73 |
| $na = 100$ | +1.5% | 5.754 | 1.617 | 0.60 |
| $nppl = 11$ | +1.9% | -12.1% | -28.9% | 0.56 |
| $na = 75$ | +6.1% | -1.2% | -1.1% | 0.60 |
| $nv = 8$ | +1.2% | -0.1% | +0.1% | 0.60 |
| $crit * 2$ | +1.6% | -0.7% | +0.2% | 0.60 |
| C1 | +6.3% | -14.1% | -30.2% | 0.55 |
| C2 | +1.7% | -24.5% | -28.8% | 0.53 |

librium excited state populations, and is a significant fraction of the total. The QSS algorithm used to perform this calculation was obtained from NEQAIR and is used as a black box. While important savings may be possible in this algorithm, no attempt has been made to achieve them. It is clear that this is a limiting factor in the efficiency of the radiation prediction. It is interesting, but not surprising, to note that the excitation calculation takes longer for conditions which are further out of equilibrium.

5.2.3 Radiation Subgrid

Calculating radiative properties at every point on a flowfield grid is often wasteful. The absorption and emission coefficients only change significantly in regions where the temperatures or species concentrations have large gradients. Bolz [30] developed an algorithm to automatically select a subset of grid points for the radiation calculation. He defines a weighting function which can be adapted to the nonequilibrium situation as

$$Z_k = k + \sum_{i=1}^k \left[W_N \frac{\overline{N}'_i}{\overline{N}'_{i,max}} + W_{T_t} \frac{|T'_t|_i}{|T'_t|_{i,max}} + W_{T_v} \frac{|T'_v|_i}{|T'_v|_{i,max}} + W_{T_e} \frac{|T'_e|_i}{|T'_e|_{i,max}} + W_{q_R} \frac{|\vec{q}'_R|_i}{|\vec{q}'_R|_{i,max}} \right] \quad (5.1)$$

The ' in these equations denotes the partial derivative with respect to η , the normal to the wall. The average derivative of the species number densities is

$$\overline{N}'_i = \sum_{j=1}^s |N'_{i,j}| \quad (5.2)$$

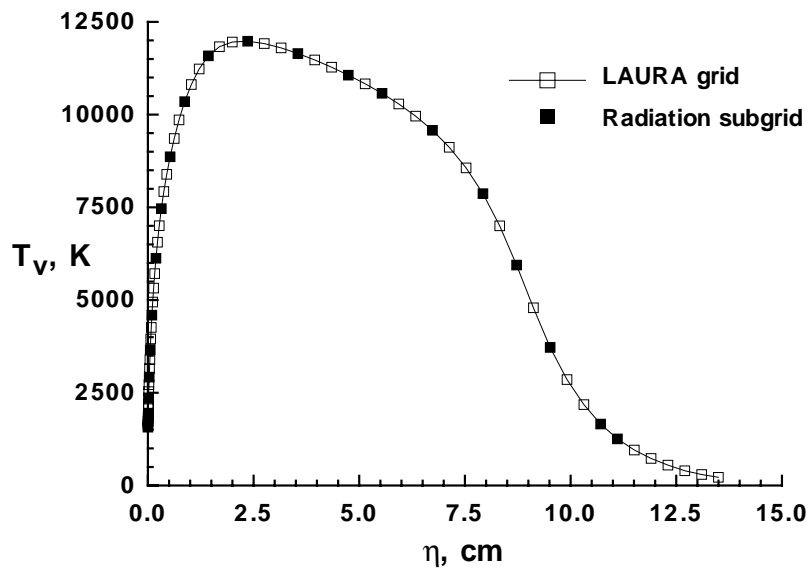


Figure 5.5. Example of Radiation Subgrid Selection

for s chemical species. Radiation is then computed for $k_R < k$ grid points at equal intervals of Z_k . An example of such a grid is given in Fig. 5.5. Though weighting factors are included for each term in Z_k there is no obvious reason to emphasize the gradient in one variable more than that of another. These factors are therefore all set equal to one. This algorithm has been implemented in LORAN as an option. It can be invoked when reducing the computational time is important. If a separate rotational temperature is available, or if individual species vibrational temperatures are computed, additional terms can be added to the function Z_k .

The subgrid algorithm has been assessed using the three nonequilibrium test cases of Ch. 7. The effects are summarized in Table 5.4. The subgrid results (columns 3 and 4) were obtained using the optimized C2 set of parameters discussed in Sec. 5.2,

Table 5.4. Effect of Radiation Subgrid Algorithm

| Case | Detail spectrum | 20 grid points | 15 grid points |
|------|-----------------|----------------|----------------|
| | All grid points | | |
| A | 0.508 | -1.4% | +6.4% |
| B | 22.50 | +10.7% | +14.2% |
| C | 292.9 | +3.9% | +2.9% |

while the detailed spectrum result (column 2) uses the Baseline parameter set to establish a reference heat flux (this is again a grid refinement test rather than an accuracy check, since even the detailed spectrum result relies on uncertain radiation and excitation properties). The CPU time required to compute the excitation and radiation for a given case is a nearly linear function of the number of grid points, so the time savings can easily be assessed.

For each of the three cases using twenty grid points (out of 64 in the flowfield grid) selected with the modified Bolz algorithm provides radiative heat flux predictions within about ten percent of the reference result, even including the spectral approximations introduced by the use of the C2 data set. A subgrid of this size is therefore considered adequate, confirming Bolz' conclusions.

In an axisymmetric or 3-D shock layer flowfield this algorithm can be applied to each normal ray of grid points. This results in a "patchwork" grid, in which cell shapes are more irregular than those in a standard LAURA grid. In an extreme case, such a grid may destabilize the transport solution. In most cases, however, optimizing

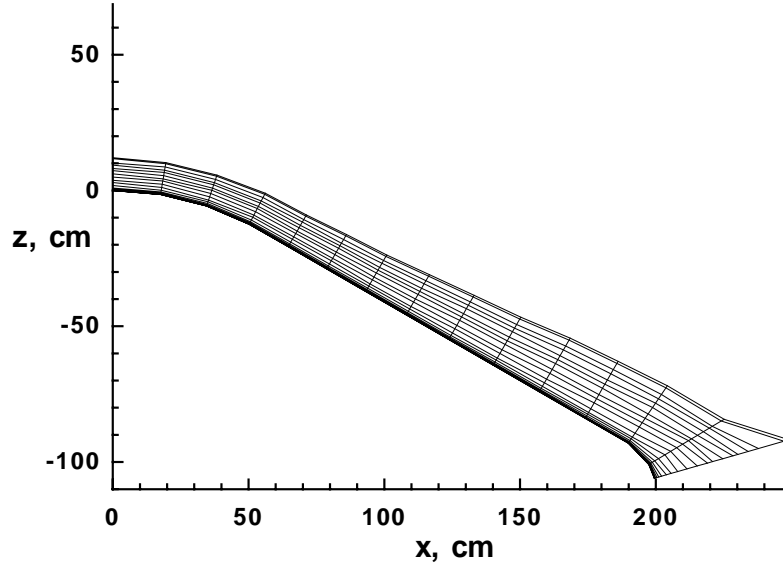


Figure 5.6. Patchwork Grid Resulting from Application of Subgrid Algorithm
Along Each Normal Line

the subgrid along each normal ray may be acceptable and even beneficial. Figure 5.6 presents an example of such a grid for a test flowfield. The irregularities appearing in the mesh are in fact quite minor.

To further reduce the required computational time, every other normal line of the flowfield grid might be skipped in the radiation calculation. The required properties can easily be interpolated for the skipped normal lines.

5.3 Flowfield Coupling

The divergence of the radiative flux, $\nabla \cdot \vec{q}_R$, which appears in the energy conservation equations to couple radiation and fluid dynamic phenomena, is computed for

each point in the flowfield by LORAN, either directly or by interpolation of results on a radiation subgrid. Coupling can be accomplished by alternatively computing the flowfield with LAURA and the radiative flux term with LORAN. Because the computation of the radiation requires up to three orders of magnitude more computational time than one iteration of the fluid dynamics computation, however, it is advantageous to utilize a multitasking strategy. Multiple tasks are assigned to the radiation calculation while a single task computes the nonequilibrium flowfield. The computational domain is partitioned into three to seven subdomains (depending on the number of processors available), each assigned to a processor for calculation of the radiation field. When run asynchronously with the single flowfield task, the multiple radiation tasks allow the flowfield equations access to the latest radiative flux terms in shared memory (multiple LAURA iterations still occur during a single radiation update). This asynchronous strategy is an efficient use of a multiple processor machine since no processor remains idle waiting for another task. Preliminary computational experiments indicate no instabilities in this approach. The effectiveness of asynchronous multitasking schemes using LAURA is further discussed in Ref. [75].

As a practical matter, it is often more efficient to first obtain a converged flowfield solution using LAURA, then “turn on” radiation and converge the coupled flowfield. If the radiation is only a small perturbation to the flowfield this second convergence may require only a few additional LAURA iterations. If there are strong radiation effects then converging the perturbed flowfield will require many additional iterations.

Though the necessary code to couple the LAURA and LORAN solutions has been generated, only a very few preliminary results have so far been obtained with flowfield coupling. The cases run to date confirm that this coupling can be done, but no significant effects have yet been observed for the cases so far examined. Coupled results are therefore not included in Ch. 6.

6 Results and Discussion

Gas radiation is a complex phenomenon, so that true verification of a radiation model requires checking it against a large number of flight and ground-based experiments covering a wide range of conditions. Only a few such measurements are currently available. Representative results for these cases are shown here as an initial test of the method. All nonequilibrium flowfields used in the verification were generated by the LAURA code of Gnoffo [71], in order to eliminate differences caused by flowfield modeling. As discussed in the following chapter, the selection of models in a flowfield code can have a large impact on the predicted radiation.

6.1 Comparison to Experiment

6.1.1 Ground-Based Data: AVCO Shock Tube

One of the classic radiation measurements is that in the AVCO shock tube [43]. Using the gas conditions suggested by Park [72], a predicted spectrum for the emission intensity has been obtained for the peak radiation point, and is shown in Fig. 6.1. This spectrum can be compared to Figure 5 of the just-cited reference, which is reproduced here in Fig. 6.2 and shows the measured spectrum compared to a prediction obtained by NEQAIR. The agreement between the measured data and the present result is no worse than that shown by NEQAIR and may actually be a little better. The atomic lines appearing in Fig. 6.1 are multiplet-averaged, and so should exhibit only a gross

agreement with the NEQAIR prediction of Fig. 6.2, as is observed.

It is clear from Fig. 6.2 that the measurements obtained in the AVCO experiments had a lot of scatter. It is difficult, therefore, to do more than note the general agreement between the experimental results and the prediction. Both predictions do have significant differences from the AVCO data in a few spectral regions (particularly below $0.3\ \mu\text{m}$). These may be attributable either to contamination of the shock tube or to inexact specification of the gas conditions.

6.1.2 Flight Data: Project FIRE

The FIRE flight project of the mid-1960's consisted of two flights simulating reentry of an Apollo type vehicle. The first flight, FIRE I, experienced telemetry problems that made data reduction and analysis difficult as well as control problems during the second half of the entry that resulted in substandard data. These problems were corrected before the FIRE II flight, which provided good measurements of the total and spectral radiation at the stagnation point during the forty second entry period [76, 77].

The FIRE flight vehicles had an Apollo-like geometry with a layered beryllium heatshield (the second layer had a geometry identical to Apollo). Each of the three layers was used up to a temperature limit and jettisoned, resulting in three periods of prime data during the entry. The first heatshield had a nose radius of 0.935 m and a diameter of 0.672 m. Only data obtained during the use of this first heatshield will be examined here, since it coincided with the nonequilibrium portion of the flight.

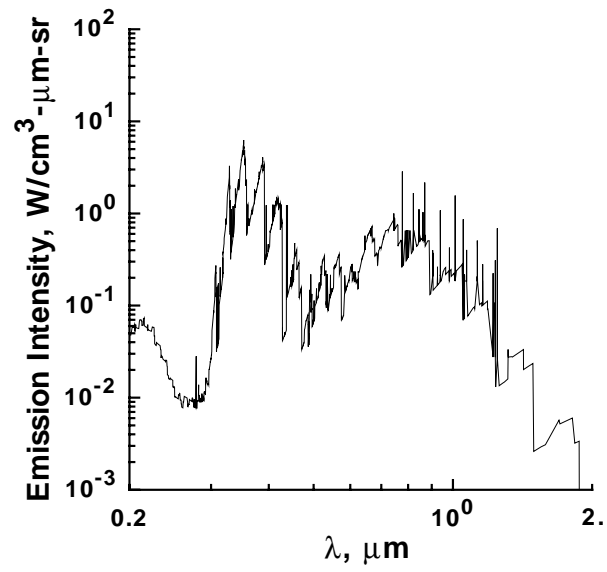


Figure 6.1. Calculated Spectrum for the Peak Radiation Point of the AVCO
Experiment

Figure 6.2. Measured Spectrum and NEQAIR Prediction for the Peak Radiation
Point of the AVCO Experiment

The trajectory of the FIRE II flight is reported in Lewis and Scallion [62]. Forebody temperature histories are given in Cornette [78]. The instrumentation used for the flight measurements is described by Richardson [61]. In particular, the spectral response of the radiometer windows is reported by Dingeldein [79, Fig.5]. It is flat between 0.23 and 2. μm in wavelength, falling off sharply below 0.2 μm and more gradually above 2. μm . The design goal is reported as a flat response from 0.2 to 6. μm . The various reports on FIRE quote actual spectral ranges starting between 0.2 and .23 μm , and ending between 4. and 6. μm . Taking these variations into account, the spectral range of 0.23 to 4. μm (0.31 to 5.4 eV) is considered to be closest to the actual window transmission range. FIRE also had scanning spectral radiometers that were designed to cover the range of 0.2 to 0.6 μm (2.1 to 4.1 eV). Mechanical problems during the flight limited forward scans to 0.3-0.5575 μm , and backward scans to 0.6090-0.3 μm [77]. The spectral resolution is quoted as 0.004 μm , with a root-sum-square uncertainty in the measured spectra of ± 23 percent. This resolution is insufficient to resolve any atomic lines.

For this study of stagnation line radiation, the FIRE vehicle geometry has been modeled by a sphere with an effective nose radius of 0.747 m. A fully catalytic wall boundary condition at the flight-measured wall temperature was used. The cases selected from the FIRE II flight are shown in Table 6.1 [62]. The designations Case A, B and C will be used below to identify each case. These cases cover the range from extreme nonequilibrium to near-equilibrium according to Cauchon [76,

Table 6.1. Selected FIRE II Flight Conditions

| Case | Time (sec) | Altitude (km) | Velocity (km/sec) | Density (kg/m ³) | T _w (K) | q _R (W/cm ²) |
|------|---------------|------------------|----------------------|---------------------------------|-----------------------|--|
| A | 1631 | 84.59 | 11.37 | 9.15e-6 | 460 | .16±20% |
| B | 1634 | 76.41 | 11.36 | 3.72e-5 | 615 | 8.2±20% |
| C | 1637.5 | 67.04 | 11.25 | 1.47e-4 | 1030 | 81.7±20% |

p.14]. Predicted temperature profiles along the stagnation line, using the baseline set of energy exchange models in LAURA (defined in Ch. 7), are presented in Figs. 6.3-6.5. For Case A, extreme thermal nonequilibrium is predicted, in agreement with Cauchon, while Case C is predicted to be in thermal equilibrium through about half the shock layer.

The flight radiation levels (q_R) quoted in the above table were taken from Cauchon [76, fig.13] and converted from intensities to fluxes assuming a transparent plane-parallel shock to be consistent with the calculations below. Also shown is the root-sum-square uncertainty estimated in a post-flight error analysis. It should be noted that the uncertainty in the radiation level for Case A is probably higher, as the radiometers were at the lower limit of their sensitivity range for that case. The measurements show considerable scatter during the early part of the trajectory [76], with a variation of about a factor of three between high and low readings for the first several seconds. The scatter decreases as the level of radiation increases. It is noteworthy that the FIRE I data acquired in this density range for a slightly higher

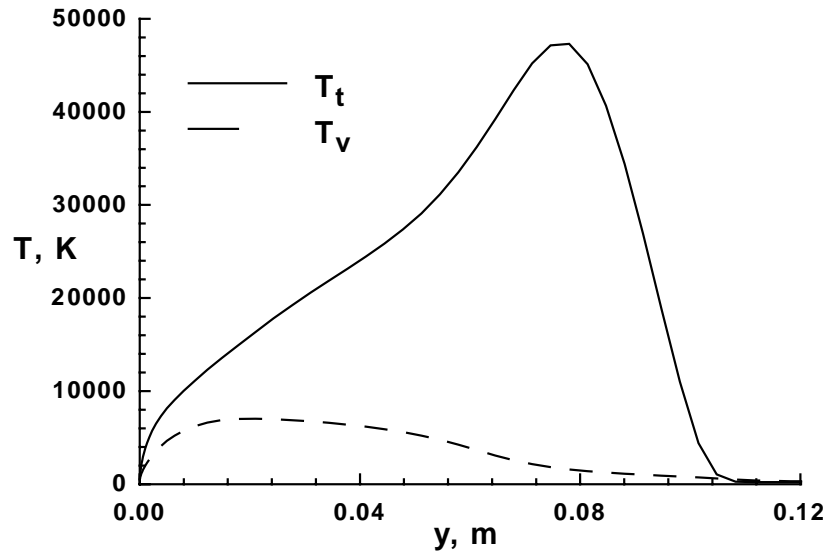


Figure 6.3. Predicted FIRE II Stagnation Line Temperature Profiles - 1631 sec

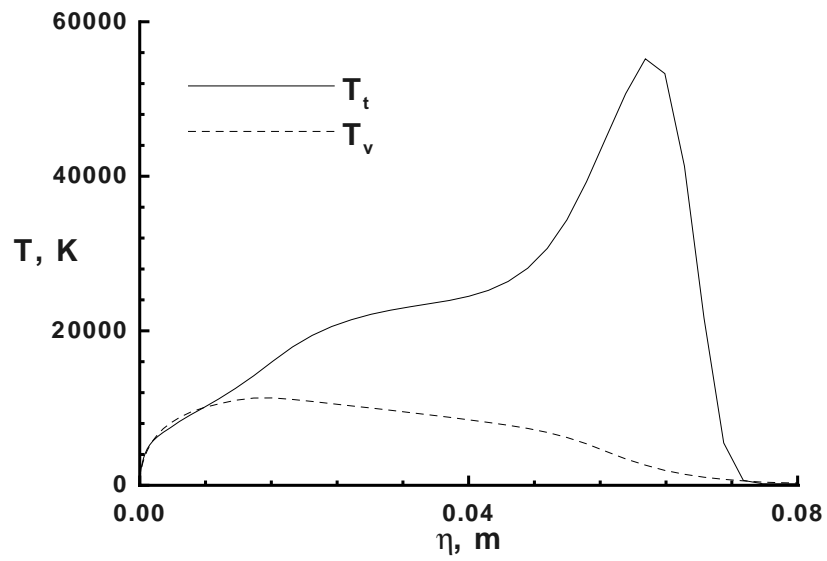


Figure 6.4. Predicted FIRE II Stagnation Line Temperature Profiles - 1634 sec

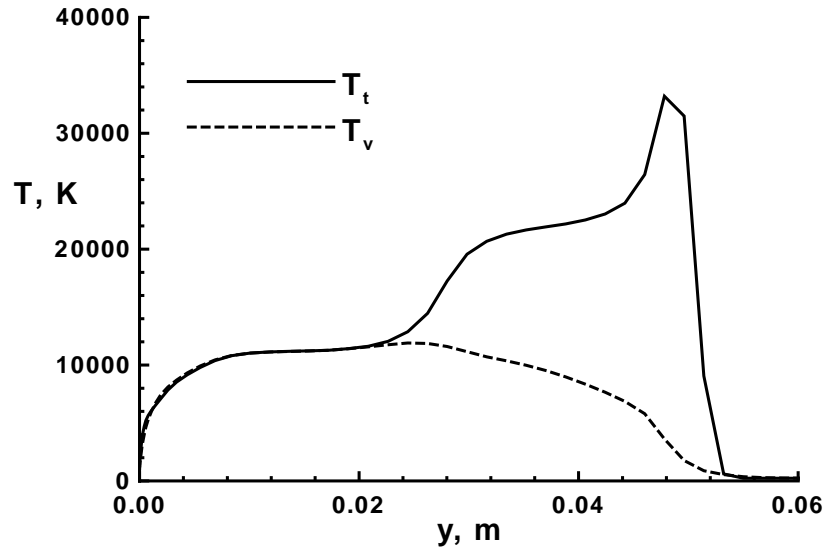


Figure 6.5. Predicted FIRE II Stagnation Line Temperature Profiles - 1637.5 sec

velocity (11.57 vs 11.37 km/sec) were higher by a factor of three than the FIRE II results for both the total and spectral radiometers. The two flights thus suggest a very sensitive dependence of radiative heating on freestream velocity under these flow conditions. At the conditions of Case B, the flight-to-flight variation is about a factor of 1.6. For Case C, it is about 1.3.

Detailed comparisons between the LORAN predictions and the FIRE flight radiometer measurements are given in the following chapter, as part of a study in which the impact of various nonequilibrium flowfield models on radiation is assessed. Some additional comparisons between LORAN and other nonequilibrium radiation prediction methods are given here.

The predicted profiles of radiative emission along the stagnation line for Case B, for

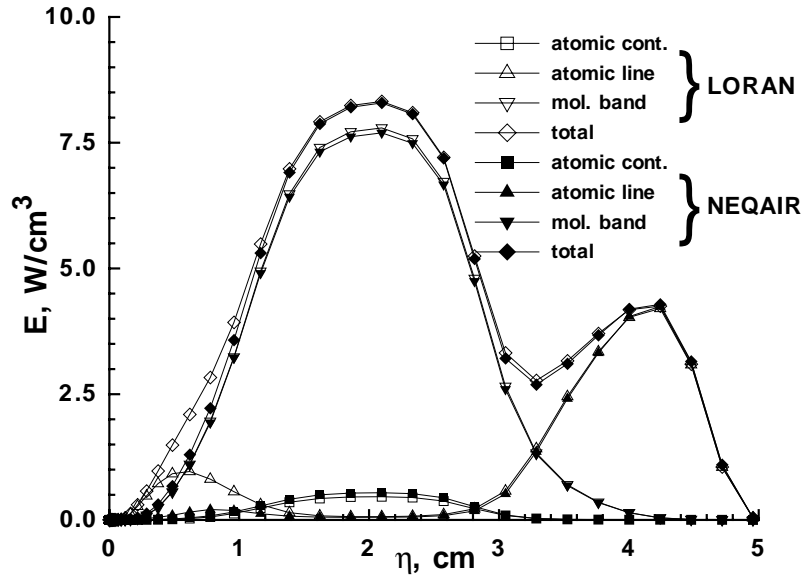


Figure 6.6. Emission Profiles for FIRE II at 1634 sec with Comparison to
NEQAIR

the spectral range in which the radiometer windows transmit, are shown in Fig. 6.6. Calculations from LORAN and NEQAIR [20] are compared, broken out into the various radiating mechanisms. The NEQAIR result shown here was computed using a version of the NEQAIR code which was obtained from Chul Park in 1988. It has been slightly modified to correct some minor errors this version contained, and to allow emission calculations within a limited spectral range. The agreement between the two predictions is excellent except for a discrepancy in the atomic line radiation near the wall. The predicted wall radiative heat flux differs by only 3 percent between the two codes.

Figure 6.7 shows the emission profiles for Case C. The overall agreement between

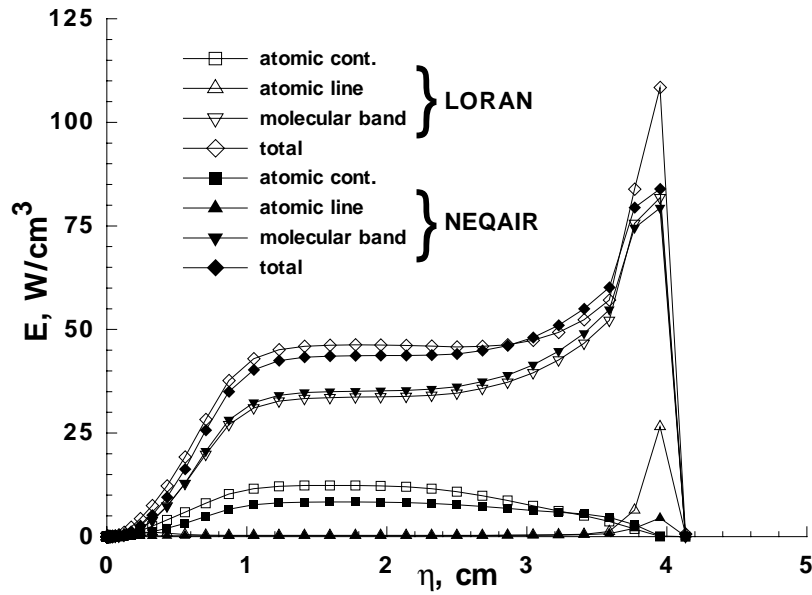


Figure 6.7. Emission Profiles for FIRE II at 1637.5 sec with Comparison to
NEQAIR

the two predictions is quite good, although there are some differences. The radiative flux reaching the wall varies by about 6 percent between these two predictions.

Radiation predictions for these cases have also been made by Carlson and Gally [35] for a nitrogen freestream. Figure 6.8 can be qualitatively compared to Fig. 6.9, which is reprinted from Figure 5 of their paper. It shows the approximate spectral variation of the wall radiative flux over the entire spectrum including the ultraviolet. Though the predicted magnitudes are lower in Ref. [35] because only nitrogen is considered, the variations are nonetheless qualitatively very similar. The details of the spectra cannot be compared because of the line group presentation used in the reference. It should also be noted that the chemical kinetics and energy exchange

Table 6.2. Radiative Heat Flux Predictions for FIRE II

| Case | NEQAIR | LORAN | Difference | LORAN |
|------------|--|--------|------------|-----------------|
| | Flux, W/cm ² (0.31-16.5 eV) | | Percent | with Absorption |
| 1634 sec | 1682. | 1806. | 7.4 | 29.35 |
| 1637.5 sec | 13233. | 14771. | 11.6 | 421.2 |

models used by Carlson and Gally are different from those in the LAURA code. As demonstrated in Ch. 7, these models can have a large impact on the magnitude and spectral distribution of the predicted radiative heating.

Results have also been computed for the complete radiation spectrum (0.31 to 16.5 eV) for these two cases. These are summarized in Table 6.2, which compares the emission predictions between NEQAIR and LORAN. The difference, about ten percent, is minor. The last column shows the total radiative flux reaching the wall when absorption is included in the transport calculation. The large self-absorption of the ultraviolet portion of the spectrum is evident here. This wall flux is still somewhat high relative to the flight data, but the effect of radiation cooling on the flowfield has not been accounted for in these calculations.

6.2 Nonequilibrium Test Cases

6.2.1 Mars Return

A flowfield solution has been obtained for one of a number of possible flight conditions identified for the return from a mission to Mars [80]. It consists of a 60° sphere

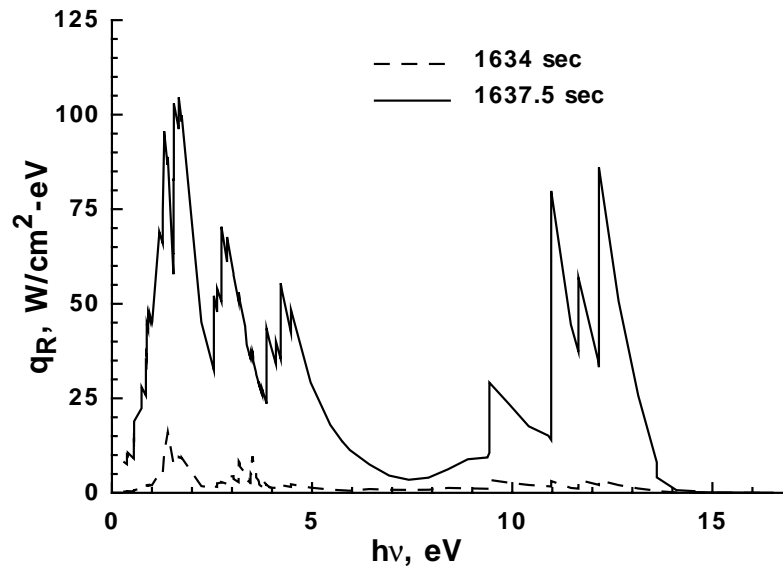


Figure 6.8. Spectral Variation of Stagnation Point Radiative Heat Transfer for
FIRE II

Figure 6.9. Spectral Variation of Stagnation Point Nitrogen Radiation for FIRE II

cone with a 1.08 m nose radius flying at 80 km altitude with a velocity of 12 km/sec. The radiative heating for this case is not too severe, so it provides a good initial test of the method. Results have been obtained for this case using both tangent slab transport and the modified differential approximation (MDA). Figure 6.10 compares the wall radiation flux predictions from the two transport methods. As expected, the MDA result is lower than the tangent slab result. The low q_w value for the MDA result near the stagnation point is believed to be erroneous, however. The sudden increase in q_w at the shoulder in the MDA result certainly is, and is attributable to the treatment of the outflow boundary. Further work will be required to correct both of these problems. The qualitative trends of the two methods are similar, showing the radiative flux increasing with distance from the stagnation point. This increase is unlike the behavior of convective heating on such a body and results because radiation is a volumetric quantity. As seen in Fig. 6.12 below, the standoff distance is much larger on the flank than at the stagnation point, and the region of significantly radiating gas has increased greatly. The vibrational temperature in this nonequilibrium flowfield is still high in this region, and a large amount of radiation is therefore emitted from the gas.

The other variable of interest for coupled flowfields is the divergence of the radiative flux in the shock layer. Figures 6.11 and 6.12 show contour plots of $\nabla \cdot \vec{q}_R$ computed with each transport method. The tangent slab result shown in Fig. 6.11 is in fact just the derivative of q_R along each normal grid line, so the values at neigh-

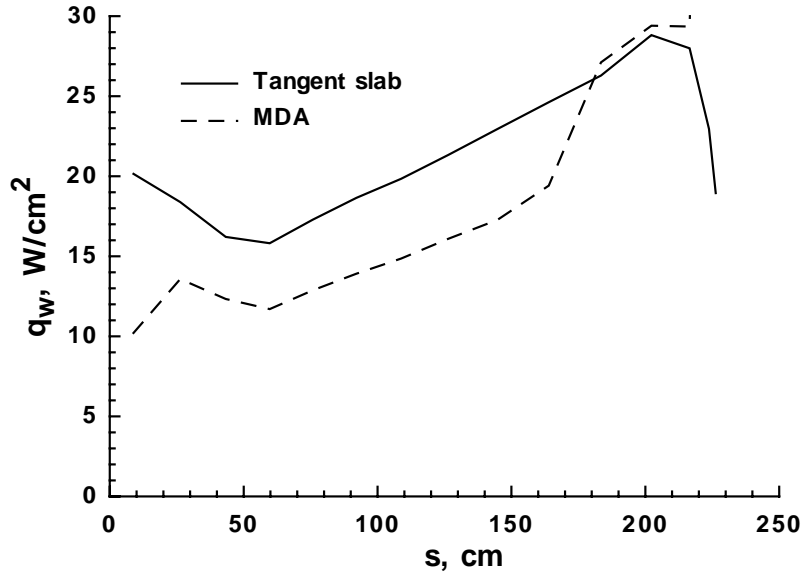


Figure 6.10. Wall Radiative Flux for Mars Return Case

boring grid lines do not influence each other. Compared to the MDA result given in Fig. 6.12 the tangent slab result is very disjointed. Accounting for the long range influence of radiation with the MDA solution provides a much smoother variation of $\nabla \cdot \vec{q}_R$. Should stability be an issue in a coupled flowfield solution, therefore, the MDA result might be expected to have less of a destabilizing effect than the tangent slab result. While this has not traditionally been used as an argument against the tangent slab approximation, it may prove to be decisive at some flow conditions. For the few coupled cases run to date, the stability of the CFD solution has not been reduced by adding radiation.

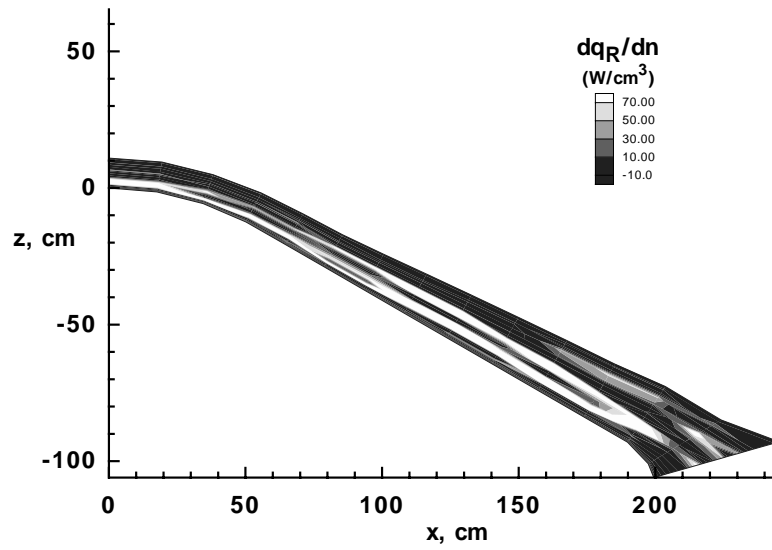


Figure 6.11. Radiative Flux Divergence for Mars Return Case with Tangent Slab
Transport

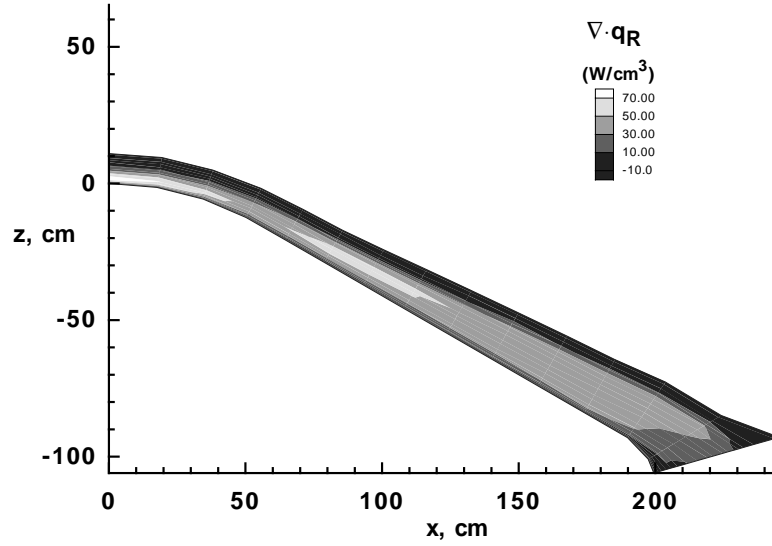


Figure 6.12. Radiative Flux Divergence for Mars Return Case with MDA
Transport

6.2.2 Aeroassist Flight Experiment

The Aeroassist Flight Experiment (AFE) is a NASA project intended to obtain flight data for the design of future Aeroassist Space Transfer Vehicles (ASTV). Measurement of the nonequilibrium radiative heating to the AFE surface is one of the principle objectives of the project. The aerobrake configuration is a raked cone with a blunted elliptic nose [81]. Several studies of nonequilibrium radiative heating for this configuration have been made to provide inputs to the design of the heatshield [17, 37, 82, 83].

The LORAN method has been used to obtain a prediction of the level and distribution of radiative heating at the peak heating point in the trajectory. An axisymmetric LAURA flowfield solution in which the AFE geometry was modeled by a sphere with an equivalent nose radius of 2.16 m [84] was generated [85]. The flowfield models used to obtain this solution are the baseline models listed in Sec. 7.1, including the use of the Park-87 chemical kinetics. The wall temperature was assumed to be constant at 1750 K.

Radiation predictions were obtained for this case, again using both tangent slab and MDA transport methods. The tangent slab calculation was completed in about 45 minutes of actual elapsed time on a Silicon Graphics 4D/320, while the MDA result required about 12 hours of elapsed time. The convergence of the MDA solution for this case was much slower than that for the Mars return case (in fact this case is not quite converged), but even this run time is not unreasonable. The radiative heating rates

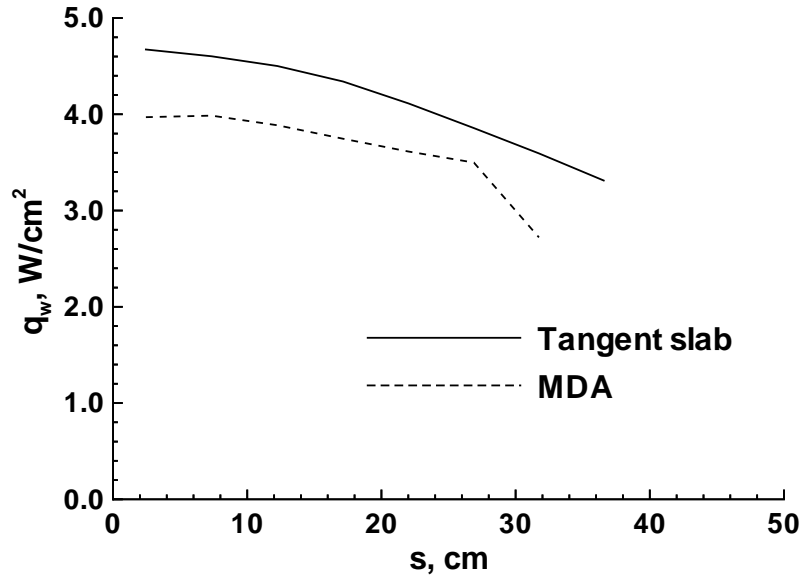


Figure 6.13. Wall Radiative Flux for AFE

predicted for the AFE peak heating point are given in Fig. 6.13. These predictions are in the same range as earlier computations for the AFE radiative heating [4, 86]. The MDA prediction is again lower than the tangent slab result, with problems still appearing at the grid boundaries. It is expected that running the MDA transport to complete convergence for this case would result in closer agreement between the two, as would a correction for the depressed MDA value near the stagnation line. It should also be noted that only the nose region of the equivalent sphere flowfield has been used for the AFE case. Away from the nose the geometry deviates quickly from the AFE configuration so the results are not of interest.

The radiative flux divergence for the AFE flowfield is presented in Figs. 6.14 and 6.15 for the tangent slab and MDA transport, respectively. Again the smoother

behavior of the MDA solution can be noted. As mentioned earlier, the tangent slab method employs a numerical differentiation to obtain dq_R/dn . This differentiation may be adding to the error already incurred by ignoring the variation of the radiation properties in the direction parallel to the surface.

The amount of heating for the AFE vehicle resulting from radiation in the ultraviolet (UV) portion of the spectrum has been the subject of some debate. The distribution of radiation predicted by the LORAN method is shown in Fig. 6.16. Curves are shown using the tangent slab and MDA transport models. The relative importance of different spectral regions varies only slightly between the two transport methods. Both curves indicate that just over half of the radiative heating experienced by the AFE spacecraft results from the UV portion of the spectrum. This is a significant fraction of the total. Radiation in the UV spectral range is highly self-absorbed (see for example Table 6.2). If the amount of self-absorption is mispredicted only slightly, the wall radiative flux may be significantly increased for AFE.

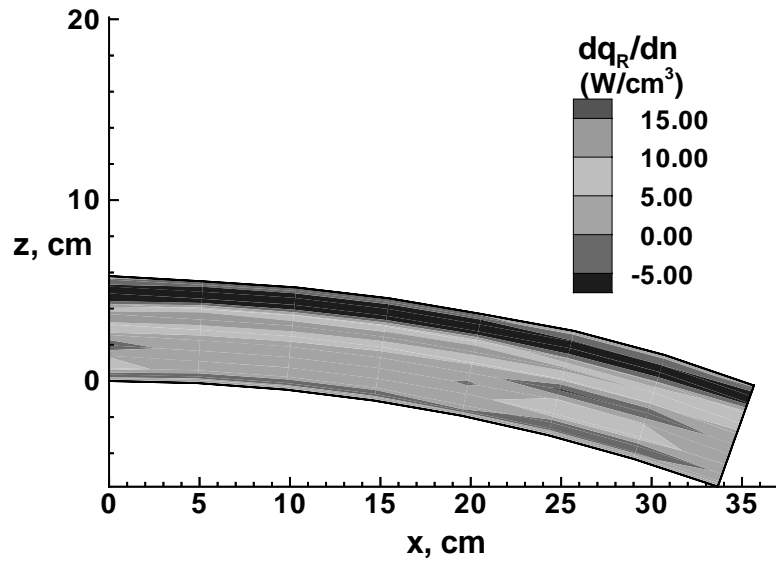


Figure 6.14. Radiative Flux Divergence for AFE with Tangent Slab Transport

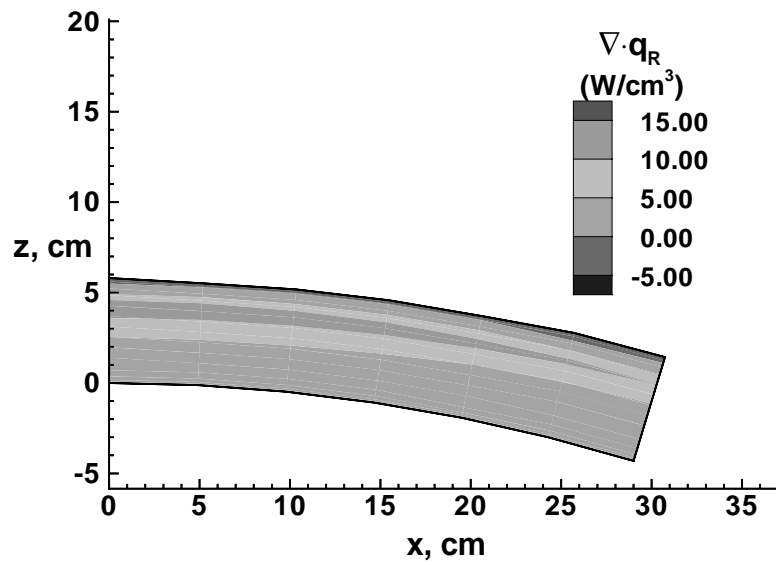


Figure 6.15. Radiative Flux Divergence for AFE with MDA Transport

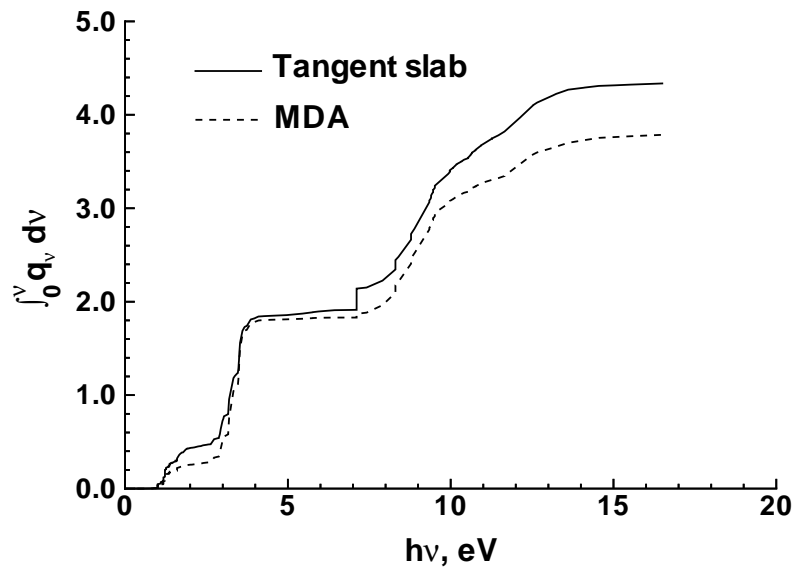


Figure 6.16. Spectral Distribution of AFE Wall Radiative Flux

7 Flowfield Model Studies

Flowfield studies were performed using the Langley Aerothermodynamic Upwind Relaxation Algorithm (LAURA) code developed by Gnoffo [71] to investigate the sensitivity of the radiation predicted by LORAN. LAURA, like all nonequilibrium Computational Fluid Dynamics (CFD) codes, contains a number of semi-empirical models governing the exchange of energy between energy modes. LAURA presently incorporates the two-temperature model of Park, in which the heavy particle translational and rotational energy modes are assumed to equilibrate to a temperature T_t (the combination is referred to as the translational mode), and the vibrational, electronic, and free electron translational energy modes are assumed to reach a separate equilibrium with a temperature T_v (the combination is referred to as the vibrational mode). Since radiation is strongly influenced by the amount of energy available in each mode, a study was conducted to assess the impact that uncertainties in these energy exchange models have on radiation predictions.

The flowfield cases chosen for these studies are taken from the trajectory of the FIRE II flight project [61, 62]. Widely varying freestream conditions were selected to exercise the exchange models over a range of levels of nonequilibrium. A description of this flight experiment was given in Sec. 6.1.2. All the cases run for the flowfield studies had 64 grid cells normal to the body in the LAURA solution. This is not sufficient to resolve the shock, as illustrated for instance in Fig. 6.5. One grid-resolved solution

with 128 grid cells was obtained to quantify the effect of this lack of resolution. The radiation prediction obtained with this refined grid was only about 15 percent different from that with the coarser grid. This is not enough to change any of the conclusions drawn from this study.

All the results presented in this chapter are for the stagnation line of the FIRE II vehicle and use the tangent slab radiative transport method. Only the spectral range in which the FIRE radiometer windows were transparent (0.31-5.4 eV) has been included.

7.1 Baseline Models

A discussion of the energy exchange mechanisms and the alternate models used for each is given in the following sections. The set of models considered as the baseline consists of the most recent recommendations from Park which have been incorporated in the LAURA code. They are, for the vibrational-translational energy exchange cross section:

$$\sigma_v = 10^{-21} (50,000/T_t)^2 m^2 \quad (7.1)$$

for the dissociation temperature:

$$T_d = T_t^{.7} T_v^{.3} \quad (7.2)$$

and for the energy exchange in dissociation:

$$\Delta E_v = \overline{E_v} \quad (7.3)$$

In addition, the set of chemical reactions known as Park-87 [87] is considered part of the baseline.

A run identifier specifies the models used for each solution. The baseline set is denoted *v173*. The first two characters, *v1*, denote the first model for vibrational-translational energy exchange, Eq. 7.1. The last two, *73*, denote the powers in the dissociation temperature equation. Only alternate models for the energy exchange in dissociation and the chemical reaction set are flagged in the run identifier for conciseness. These will be explained as they are used below.

7.2 Energy Relaxation

The modeling of relaxation or equilibration between energy modes is an important question in nonequilibrium CFD. Generally the process of equilibration is not completely understood and must be described semi-empirically. Several formulations have been proposed for many of these models. Data to evaluate the different formulations are scarce.

To quantify the influence which the different proposed formulations of the models for energy relaxation have on predictions of radiative heat transfer, a parametric study was undertaken on a number of such models. The models and formulations considered, and the results obtained, are detailed below.

7.2.1 Dissociation Temperature

The dissociation temperature, T_d , is the rate-controlling temperature for reactions involving the dissociation of a molecular species. Several formulations have been proposed for this temperature, notably by Park and his co-workers [87, 88]. These models are empirical and consist of a geometric weighting of the translational temperature T_t and the vibrational temperature T_v as follows:

$$T_d = T_t^m T_v^n \quad (7.4)$$

The choice of powers m and n adjusts the weight given to each temperature. The recent trend has been to increase the weighting of the translational temperature T_t because of indications that heavy particle collisions are more important than other mechanisms in causing dissociation. Three different models with (m, n) equal to $(.5, .5)$, $(.7, .3)$, and $(1, 0)$ are considered here. The first set is the original Park two-temperature proposal, the second the more recent model, and the third is included to study the extreme case of dissociation controlled by the heavy particle temperature alone. The dissociation temperature models will be denoted by *55*, *73*, and *10*, respectively, in the third and fourth digits of the run identifier.

As shown in Figs. 6.3-6.5, the translational temperature T_t is much higher than T_v near the shock. Increasing the weighting of the dissociation temperature, T_d , on T_t in Eq. 7.4 therefore results in faster dissociation of the molecular species. This dissociation removes both translational and vibrational energy, decreasing T_t and T_v . The increased dissociation is shown in Fig. 7.1 which compares the N_2 and O_2 profiles

along the stagnation line for Case A for the two extreme T_d models. The effect on the temperature profiles is shown in Fig. 7.2 also for Case A. The decreased temperature results in increased density and a smaller shock standoff distance. For the three FIRE II cases, placing increasing weight on the translational temperature T_t in the definition of the dissociation temperature T_d decreases the total radiation. Part of the decrease occurs in the molecular bands, which depend directly on the molecular concentrations. The rest of the decrease results from the lower T_v and decreased standoff distance affecting all three radiating mechanisms. Figure 7.3 shows the emission profiles for the three T_d models for Case A. Case A is the most nonequilibrium of the three FIRE conditions studied here, and therefore is most sensitive to these energy relaxation models. The sensitivity to the T_d model decreases at the later, more equilibrium, flight times of Cases B and C.

Tables 7.1-7.3 at the end of this chapter reveal that in all three cases ($v110$, $v155$ and $v173$) the predictions are closer to the flight data when T_t is weighted more in the definition of T_d , confirming the recent work on this model mentioned above. For Cases A and B, agreement within about a factor of three is found. For Case C, the case nearest equilibrium, the variations caused by this model are within the uncertainty of the flight data.

7.2.2 Vibrational-Translational Energy Exchange

The equilibration of the vibrational and translational energy modes is modeled using a relaxation time, τ_v , for each species. Millikan and White [89] proposed a

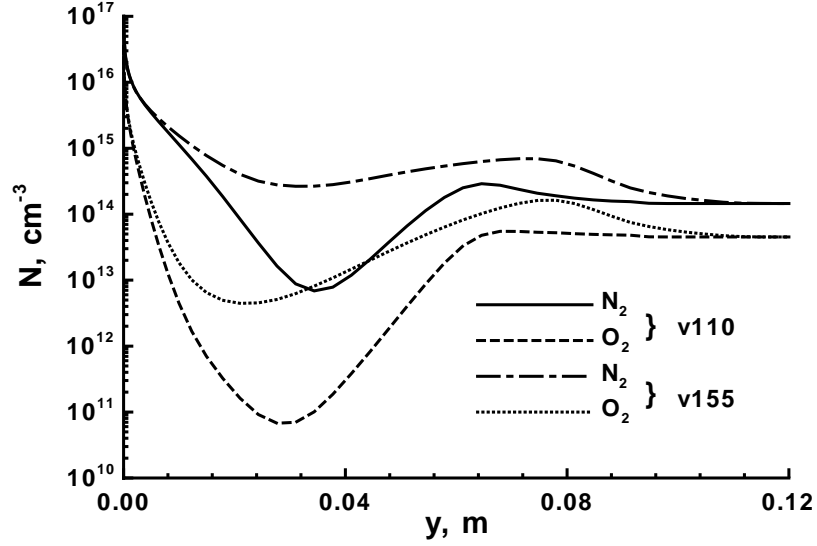


Figure 7.1. Effect of T_d Models on Molecular Dissociation - 1631 sec

semi-empirical formulation, τ_v^{MW} , in the range of 300 to 8000 K. Park [90] suggests an additional collision limiting correction, τ_v^P , for high temperatures where the Millikan-White correlation predicts excessively fast relaxation. A concise explanation of the failure of the Millikan-White correlation is provided by Sharma and Park [91, p. 136]. The total relaxation time is then

$$\tau_v = \tau_v^{MW} + \tau_v^P \quad (7.5)$$

where Park's contribution is

$$\tau_v^P = (\sigma_v \overline{v_s} N_s)^{-1} \quad (7.6)$$

In this expression $\overline{v_s}$ is the average speed and N_s the number density of molecular species s , and σ_v is an effective cross section for vibrational relaxation. The latter quantity has been the subject of some debate, with three different values receiving

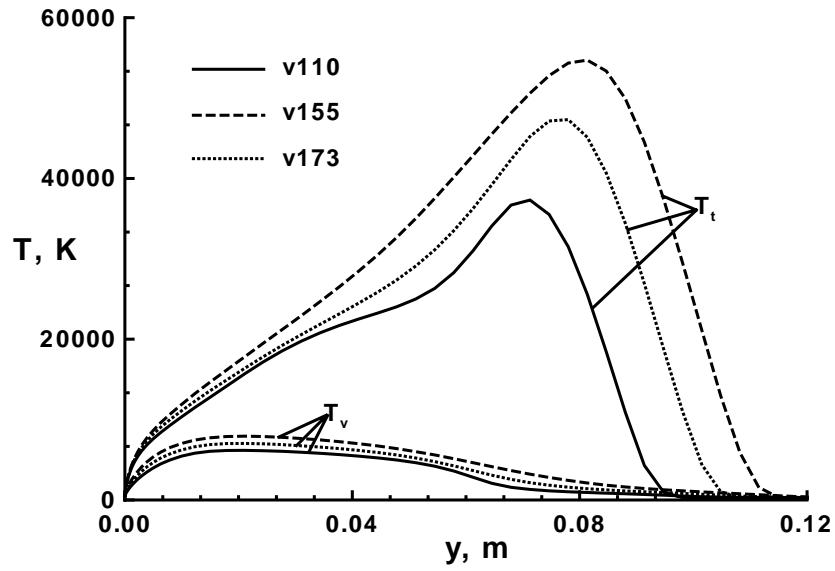


Figure 7.2. Effect of T_d Models on Temperature Profiles - 1631 sec

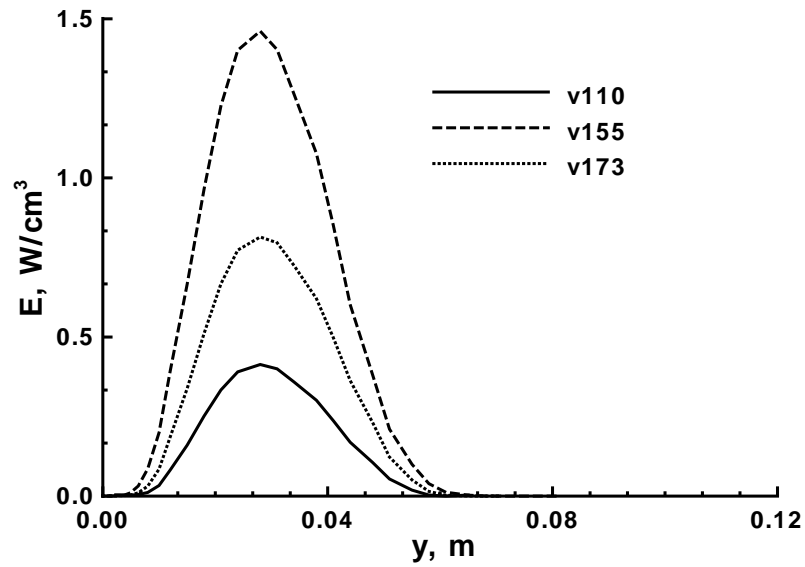


Figure 7.3. Effect of T_d Models on Radiative Emission Profiles - 1631 sec

support in various efforts to match the limited experimental data that has bearing on the question:

$$\sigma_v = 10^{-21} (50,000/T_t)^2 \text{ m}^2 \quad (7.7)$$

$$\sigma_v = 10^{-20} \text{ m}^2 \quad (7.8)$$

$$\sigma_v = 10^{-21} \text{ m}^2 \quad (7.9)$$

Equation 7.8 is the original proposal, which assumes this cross section to be one tenth of the elastic cross section. Equation 7.9 was suggested when Eq. 7.8 seemed still too high. Equation 7.7 is a modification of Eq. 7.9 that reduces the contribution of τ_v^P at low temperatures. All three models are considered here, and are identified by the notation *v1*, *v2*, and *v3*, respectively, in the first two digits of the run identifier.

A further modification to this energy exchange process has been proposed by Park [87]. He argues that vibrational relaxation exhibits a diffusion-like behavior at high temperatures which requires a correction to the relaxation time. However, this modification requires evaluation of the post-shock levels of T_t and T_v . Interpretation of these quantities in a shock capturing solution is somewhat ambiguous [92]. Improper definition can lead to instabilities in some circumstances, consequently no attempt was made to include this modification.

Figures 7.4 and 7.5 present the effect of the different vibrational-translational energy exchange cross sections in Eqs. 7.7-7.9 on the temperature and radiative emission profiles predicted for Case A. For a smaller σ_v , the relaxation time τ_v increases. Increasing τ_v delays the relaxation of translational to vibrational energy. This increases

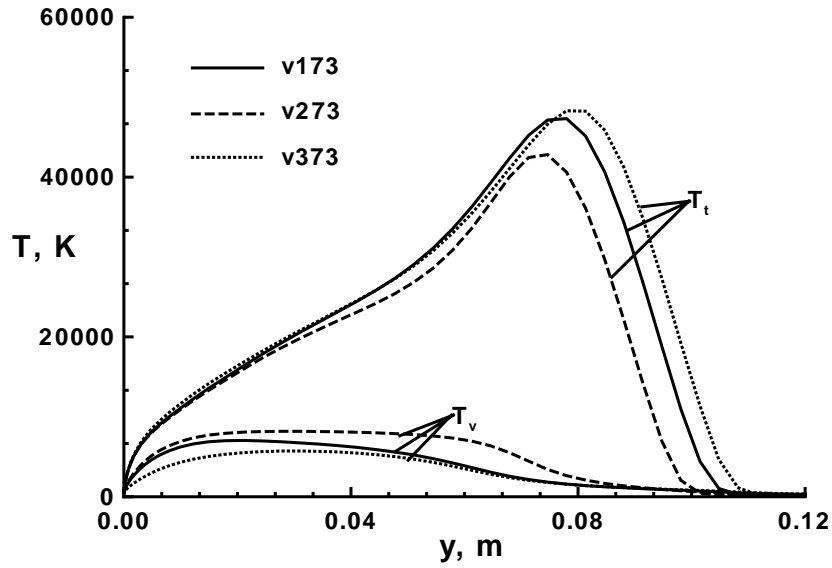


Figure 7.4. Effect of σ_v Models on Temperature Profiles - 1631 sec

T_t while reducing T_v , as illustrated in Fig. 7.4. Although the standoff distance increases with increasing T_t , the reduction in radiation due to the lower T_v in this model more than compensates. The lower T_v reduces the radiation from all three mechanisms, as shown in Figure 7.5. The lowest radiation for all three FIRE cases is predicted with Eq. 7.9, and the highest with Eq. 7.8. Comparing the predicted radiation for the $v173$, $v273$, and $v373$ models in Tables 7.1-7.3 shows that the influence of σ_v is largest in Case A, the most nonequilibrium case.

Again all three cases are closest to FIRE II when the radiation prediction is lowest, with Eq. 7.9, though only Case A exhibits much sensitivity or discrimination among the models. The predictions in Case B remain high, while the effect on Case C, the near-equilibrium case, is within the data uncertainty as was observed for the

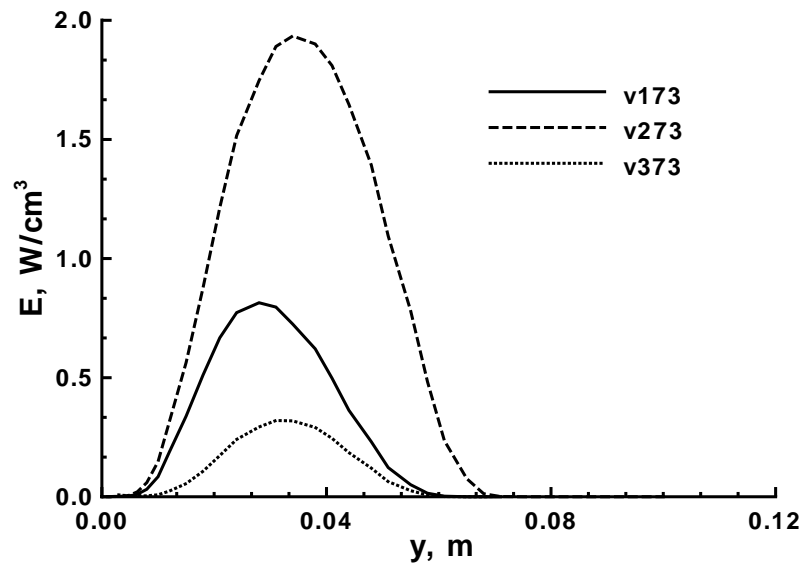


Figure 7.5. Effect of σ_v Models on Radiative Emission Profiles - 1631 sec

dissociation temperature models.

7.2.3 Energy Exchange in Dissociation

When a diatomic molecule dissociates, the vibrational energy it contained is consumed by the higher ground states (heats of formation) of the constitutive atoms. The energy thus removed must be accounted for in the vibrational energy equation. The amount of energy lost is commonly assumed to be the average vibrational energy at the local conditions, $\overline{E_v}$. Because dissociation from a higher vibrational state may be more probable (the concept of preferential dissociation) several other formulations have been proposed [69].

One model assumes that the vibrational energy loss in dissociation, ΔE_v , is some

fraction of the dissociation energy of a molecule measured from its ground state, D :

$$\Delta E_v = c_1 D \quad (0 < c_1 \leq 1) \quad (7.10)$$

Sharma et al. [88] have proposed using $c_1 = 0.3$. This model was considered, but since it predicts the non-physical result of a negative T_v in the shock region it was not pursued [92].

Park [93] has proposed that

$$\Delta E_v = D - kT_t \quad (7.11)$$

so that the energy lost is the dissociation energy minus the average translational energy. This model arises from the assumption that dissociation only occurs from levels that are within the average collisional energy of the dissociation threshold (similar to the mechanism of bound-free radiation). Again, this ΔE_v is too large (particularly when T_t is low) and results in an unrealistically small T_v behind the shock [92].

A third proposed model assumes that dissociation occurs from some vibrational state(s) above the average. This is expressed as:

$$\Delta E_v = c_2 \overline{E_v} \quad (c_2 > 1.) \quad (7.12)$$

The best value of c_2 to use in this empirical model is unknown, and may depend on $\overline{E_v}$ (or T_v). In this work $c_2 = 2$ has been selected to provide an initial assessment of the model. The suffix *2evs* is used in the run identifier for these cases.

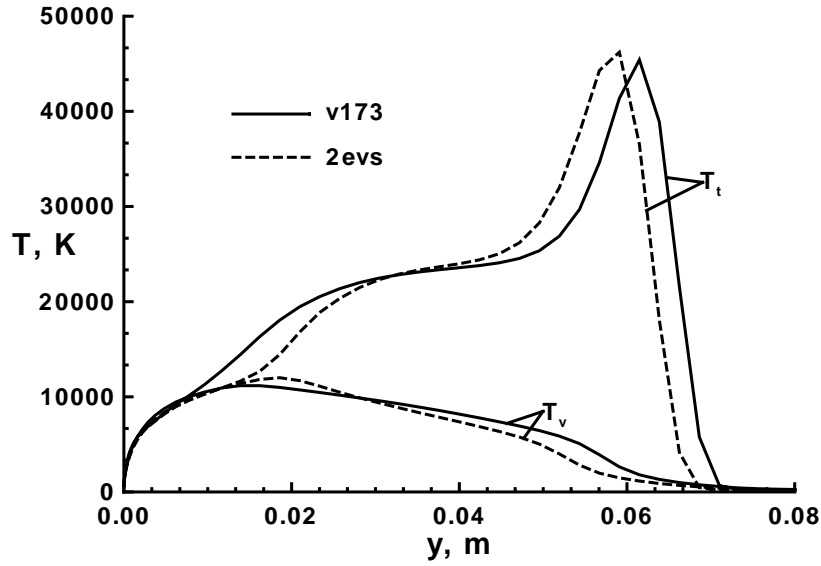


Figure 7.6. Effect of ΔE_v Models on Temperature Profiles - 1634 sec

Figure 7.6 compares the temperature profiles for Eq. 7.12 with $c_2 = 1$ (the baseline model) and $c_2 = 2$ for Case B. The increased ΔE_v in the *2evs* model ($c_2 = 2$) reduces T_v in the region behind the shock where dissociation occurs, and increases it deeper in the shock layer where recombination begins. It also results in a smaller shock standoff distance. Figure 7.7 presents the radiative emission for Case B and confirms that the lower T_v near the shock results in reduced radiation, while the higher T_v in the shock layer increases it. This is observed in the tables as a decrease in the molecular band radiation and a slight increase in the atomic contributions, resulting in a net decrease in the total radiation. (The lower peak in the dashed curve of Fig. 7.7 is the atomic radiation peak.)

For Cases A and B, the decreased radiation resulting from the *2evs* model brings

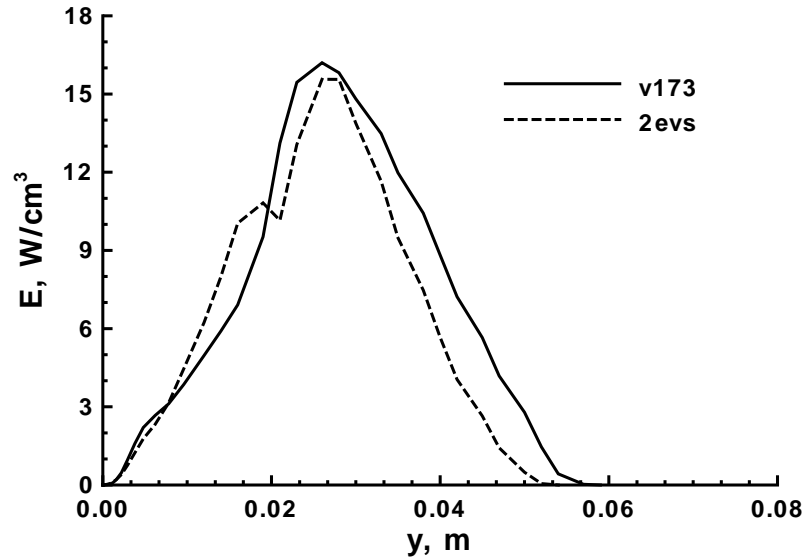


Figure 7.7. Effect of ΔE_v Models on Radiative Emission Profiles - 1634 sec

the prediction closer to the flight measurement, but it remains high (Tables 7.1-7.3). For Case C the effect is within the data uncertainty, but this is the only model where the prediction is lower than the flight measurement. Table 7.3 also includes a solution run with the model of Eq. 7.10 using $c_1 = 0.3$ (denoted *3dis*) for comparison. A flag was introduced in LAURA to suppress negative temperatures. The result is not significantly different so it provides no incentive to pursue this model.

As with the two previous energy exchange models, the sensitivity to this model decreases as the flowfield tends toward equilibrium. The decreasing sensitivity to all these models near equilibrium is expected, since they govern the exchange between energy modes in the two-temperature thermal nonequilibrium model. When dealing with flowfields near equilibrium, the choice of formulation for these models is not as

important. The remaining models shown in Tables 7.1-7.3 will be discussed later.

7.3 Spectral Radiation Comparison

To obtain further information on the validity of the energy exchange models, the FIRE spectral radiometer measurements (vs. wavelength, λ , in μm) are compared with those exchange models whose predictions are closest to the flight measurements. Only continuum radiation is shown for the predicted spectra, since the resolution of the flight spectral radiometer is not sufficient to record any line radiation. In evaluating the flight spectra reproduced here, it should be noted that only a few are available in the literature. Those that have been published are the ones that were judged by researchers at the time to contain the least amount of noise. This criterion had the effect of selecting spectra that correspond to the lower range of flight radiation measurements. It is not known whether the unpublished data which correspond to the higher range of measurements had increased intensity levels or broader spectra or both.

Case A (t=1631 sec)

The spectral distribution of radiation has been examined for Case A for the *v373* solution, which appears in Table 7.1 to best match the flight data. Figures 7.8 and 7.9 compare the prediction at 1631 sec with a flight spectral radiometer scan at 1631.3 sec, the closest available, reproduced from Cauchon [77]. Though the prediction is much higher than the flight scan they are qualitatively similar. Both show radiation from

the N_2^+ first negative band, whose two major band heads can be distinguished. (The spike in the flight spectrum between 0.5 and 0.6 μm has been attributed to a spurious signal [77].) Integrating the LORAN predictions over this limited spectral range results in a value that is high but within the data scatter at this flight condition [76, Fig. 13].

Case B (t=1634 sec)

Figures 7.10 and 7.11 compare the *2evs* result for Case B, the closest to the flight data in Table 7.2, to a flight spectrum at 1634.43 sec [77], the closest time available. The qualitative agreement is comparable to that shown for Case A above. Integrating the predicted radiation over the range of the spectral radiometer gives a result that again, while high, is within the scatter of the flight data given in Fig. 13 of Cauchon [76]. The curve labeled *dk73* in this figure will be discussed in Sec. 7.4.

Case C (t=1637.5 sec)

Figures 7.12 and 7.13 compare the predicted *v373* spectrum for Case C to the nearest available flight spectrum, at 1636.43 sec. As in Case A, the *v373* shows the closest match to the flight data in Table 7.3. By this point in the trajectory, the radiometer windows are approaching their melting point. A detailed post-flight analysis determined, however, that the windows cause less than a 10 percent change in the measured radiation [76]. The intensity spectrum predicted by the *v373* is excessive, having far too much radiative energy in the N_2^+ first negative band. The

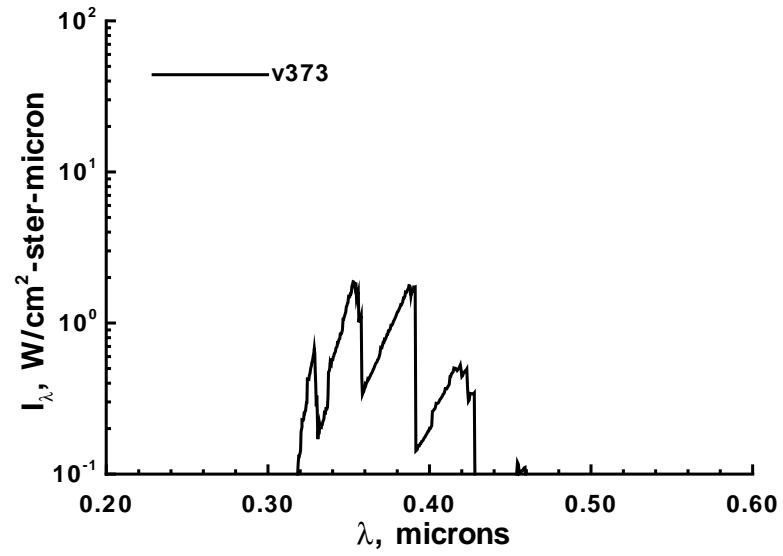


Figure 7.8. Predicted Radiation Spectrum - 1631 sec

Figure 7.9. Measured Radiation Spectrum - 1631.3 sec

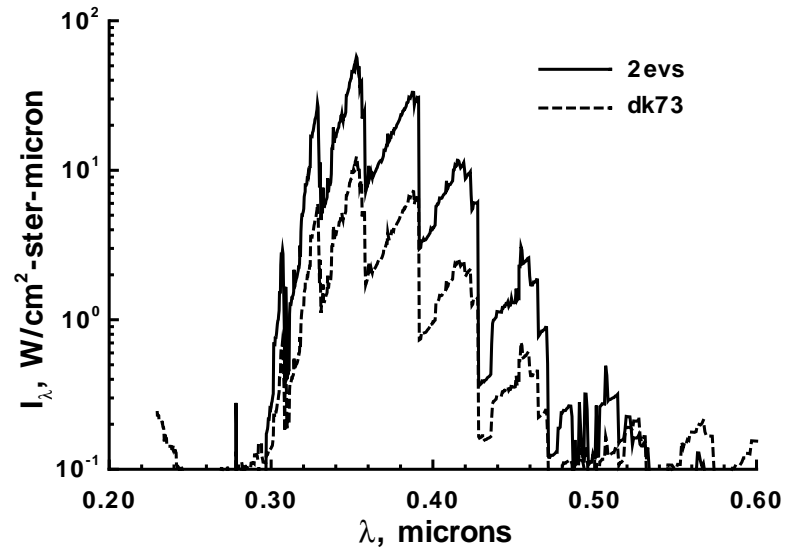


Figure 7.10. Predicted Radiation Spectra - 1634 sec

Figure 7.11. Measured Radiation Spectrum - 1634.43 sec

curve labeled *v1eq* will be discussed below.

7.4 Nonequilibrium Chemistry

The set of chemical reaction rates used in a flowfield model is somewhat better defined than are the rates of energy relaxation. Uncertainties remain, however, particularly in the extrapolation of the rates to temperatures at which little or no experimental data is available. Two rate sets are in widespread use: that of Dunn & Kang [94], and that of Park [87]. The latter rate set has been updated several times [67, 95]. In addition, there are several options for obtaining rates for the backward reactions. Dunn & Kang originally included curve fits for the backward rates. It is generally agreed, however, that more accurate results for backward rates are obtained by computing them from the forward rates and associated equilibrium constants (at appropriate temperatures). These equilibrium constants are commonly obtained from curve fits. Recently Gupta [96] generated a new set of curve fits for these constants which differ noticeably from those proposed by Park. Mitcheltree [97] has used the LORAN radiation model in the LAURA code to study the influence of these various sets of chemical rate data for a 12 km/sec entry. A few results for the FIRE II cases are presented here.

The Dunn & Kang chemical kinetics model, denoted *dk*, has been applied to each of the FIRE II cases. As shown in Table 7.2, it results in a closer match of the flight heating rate for Case B. The wall spectral intensity predicted for this model was therefore also included in Fig. 7.10. This spectrum is much closer to the FIRE II

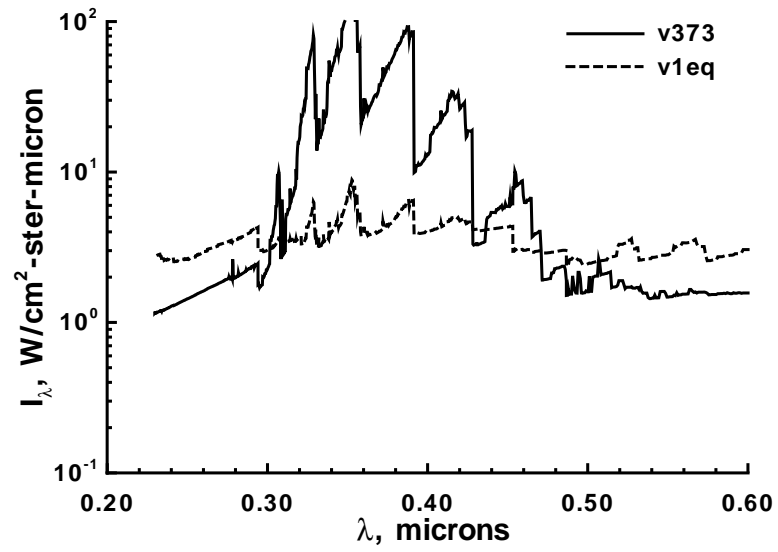


Figure 7.12. Predicted Radiation Spectra - 1637.5 sec

Figure 7.13. Measured Radiation Spectrum - 1636.43 sec

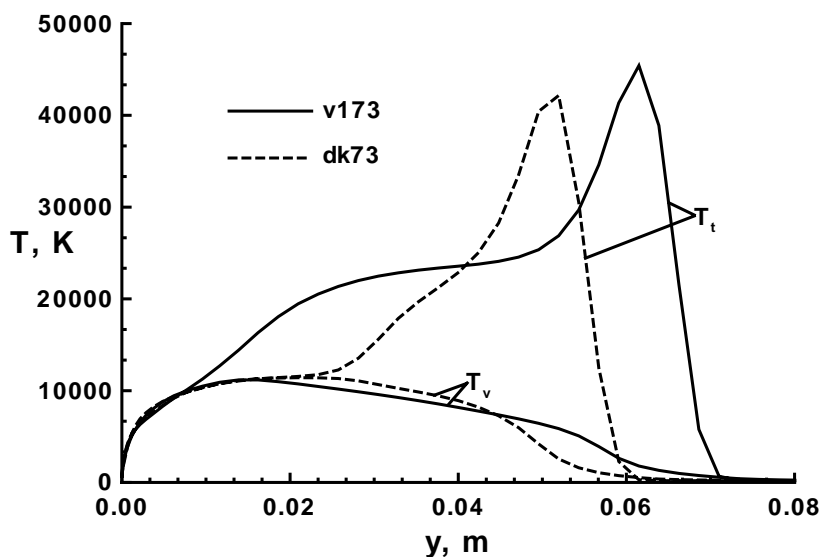


Figure 7.14. Effect of Chemical Kinetics Model on Temperature Profiles - 1634 sec

measurements than any of those obtained for Case B with the Park kinetics [87]. The distribution and relative magnitudes of the several band heads in this figure agree quite well with the flight data, and the Dunn & Kang prediction exhibits quantitative as well as qualitative agreement with the measured spectrum. For Case A, Table 7.1 shows that the Dunn & Kang model is not an improvement. For the near-equilibrium Case C, the Dunn & Kang result was obtained for a thermal equilibrium solution. This resulted in a significantly higher radiation prediction (Table 7.3).

Referring again to the temperature profiles in Figs. 6.3-6.5, it is clear that the thermal relaxation is in two stages with different time constants. Right behind the shock T_t decreases rapidly as a result of dissociation, then starts to level off. This suggests the involvement of slow reactions such as ionization, which become increasingly

important as the level of ionization rises. This two-stage equilibration is much less apparent for the Dunn & Kang chemical kinetics model profiles shown in Fig. 7.14 for Case B. The improved agreement noted for Case B only with the Dunn & Kang solution suggests, therefore, that this second equilibration process deserves further study.

7.5 Nonequilibrium Temperature

The most obvious model of importance to the radiation calculation is the nonequilibrium temperature model. The choice of the number of temperatures modeled and the equations used is a crucial one for radiation. In a completely nonequilibrium situation, separate temperatures would be required for each energy mode of each species. This is impractical, except perhaps in a Direct Simulation Monte Carlo (DSMC) solution. Park's two-temperature model, discussed above, seems to provide reasonable accuracy with the minimum of complexity. If three temperatures are to be used, there is as yet no consensus about the electron energy equation which should be employed. Carlson and Gally [98] have studied this question for Martian return conditions. Candler [4] has studied the problem for general conditions.

For Case C, which is close to thermal equilibrium, solutions were generated for both the Park and the Dunn & Kang chemical kinetics, using Park's two temperature model or assuming thermal equilibrium (a single temperature T). This allows an assessment of the extent and impact of thermal nonequilibrium. The results are included in Table 7.3 (*vleq* and *dkeq*, respectively). The *vleq* result is closer to the

Table 7.1. Effect of Energy Exchange Models for FIRE II at 1631 sec

| Run Identifier | Flux, W/cm ² (0.31-5.4 eV) | | | |
|----------------|---------------------------------------|-----------|-------------|----------------|
| | Atomic Cont. | Mol. Band | Atomic Line | Total |
| flight | | | | $.16 \pm 20\%$ |
| v110 | .1E-4 | .54 | .4E-3 | .54 |
| v155 | .7E-5 | 2.0 | .5E-2 | 2.0 |
| v173 | .1E-4 | 1.1 | .9E-3 | 1.1 |
| v273 | .1E-4 | 3.2 | .2E-1 | 3.2 |
| v373 | .1E-4 | .41 | .5E-3 | .41 |
| dk73 | .2E-3 | 1.7 | .5E-1 | 1.7 |
| v1732evs | .1E-4 | .72 | .5E-3 | .73 |

Table 7.2. Effect of Energy Exchange Models for FIRE II at 1634 sec

| Run Identifier | Flux, W/cm ² (0.31-5.4 eV) | | | |
|----------------|---------------------------------------|-----------|-------------|----------------|
| | Atomic Cont. | Mol. Band | Atomic Line | Total |
| flight | | | | $8.2 \pm 20\%$ |
| v110 | .2E-1 | 17.7 | 2.7 | 20.3 |
| v155 | .4E-1 | 19.1 | 3.8 | 22.9 |
| v173 | .3E-1 | 17.7 | 3.3 | 21.1 |
| v273 | .7E-1 | 22.5 | 5.2 | 27.8 |
| v373 | .1E-1 | 17.6 | 2.2 | 19.9 |
| dk73 | .3 | 3.1 | 7.9 | 11.4 |
| v1732evs | .1 | 12.1 | 6.0 | 18.3 |

flight result and is therefore shown on Fig. 7.12. The agreement between this predicted spectrum and the flight spectrum is remarkable. (Recall that the spectral radiometer did not measure below $0.3 \mu\text{m}$, so there is nothing to compare with in this range.) Thus, examining the radiation spectra at this condition suggests that Case C is in fact in thermal equilibrium, or at least that the distribution of energy between modes is more nearly in equilibrium than was suggested by the other nonequilibrium CFD models.

Table 7.3. Effect of Energy Exchange Models for FIRE II at 1637.5 sec

| Run Identifier | Flux, W/cm ² (0.31-5.4 eV) | | | |
|----------------|---------------------------------------|-----------|-------------|-----------------|
| | Atomic Cont. | Mol. Band | Atomic Line | Total |
| flight | | | | $81.7 \pm 20\%$ |
| v110 | 3.8 | 33.5 | 45.3 | 82.7 |
| v155 | 3.9 | 38.9 | 46.2 | 89.0 |
| v173 | 3.9 | 35.4 | 45.7 | 84.9 |
| v273 | 4.1 | 38.8 | 49.2 | 92.1 |
| v373 | 3.8 | 33.6 | 44.5 | 81.9 |
| dkeq | 5.2 | 18.8 | 99.9 | 123.9 |
| v1eq | 6.5 | 5.8 | 75.6 | 87.8 |
| v1732evs | 4.6 | 20.8 | 52.0 | 77.4 |
| v1733dis | 4.6 | 15.5 | 52.6 | 72.8 |

8 Conclusions

8.1 Accomplishments

A new method, LORAN, was developed to predict gas radiation in conditions of thermochemical nonequilibrium. This method includes a moderately detailed radiative spectrum employing the smeared band model for molecular radiation. It is intended to provide radiation predictions with an accuracy between that of detailed line by line models and what is obtainable from highly approximate but very fast step models. The optimization of the method to provide the maximum detail for the minimum of computational effort is described. Representative results comparing the method to available ground and flight data indicate that LORAN predicts radiation with accuracy similar to that of Park's NEQAIR code [20] and the nonequilibrium method of Carlson et al. [35].

Two options for radiative transport were incorporated in LORAN. The first is the traditional tangent slab method, in which the radiating medium is assumed to be one-dimensional. A second transport method was developed without invoking this approximation by applying a modified differential approximation (MDA). Predictions of the radiative heat flux to the wall from the two transport methods were compared and show qualitative agreement with fluxes from the MDA method about 20 to 25 percent lower than from the tangent slab. The profiles suggest that the boundary conditions of the MDA method might be improved. The variation of the divergence

of the radiative heat flux, appearing in the energy equation to couple the radiation and flowfield properties, was also examined and found to be much smoother in the MDA method. In addition to providing more accurate coupled results, this feature of the MDA method has the potential to enhance the stability of coupled solutions.

A sensitivity study was performed using LORAN and flowfield solutions from LAURA to assess the effect that various models used in nonequilibrium CFD codes have on radiation predictions. The results indicate that radiation is a very sensitive indicator of phenomena occurring in nonequilibrium flowfields. This fact may be used in conjunction with currently available and future flight and ground-based data to improve the modeling of such things as exchange between energy modes in thermochemical nonequilibrium, and chemical reaction rates.

8.2 Future Work

Opportunities and needs for additional work have been identified in several areas.

LORAN makes use of the NEQAIR method and data set for the computation of electronic energy level populations in nonequilibrium. This QSS algorithm incorporates assumptions about the rate of change of energy level populations which are known to be violated in high gradient flow regions. The rate data which it uses are also known to contain uncertainties. Both of these areas of potential error should be investigated in more detail.

Many of the radiative properties used in LORAN are uncertain, so the radiative heating values it predicts can only be regarded as approximate. An effort needs to be

undertaken to reduce these uncertainties. To do so may require new measurements to be made beyond those already available in the literature. In addition, corrections to the bound-free and free-free atomic continuum absorption coefficients accounting for deviations from a hydrogenic atomic structure could be included, though an initial inquiry suggests that these corrections have little effect.

The multi-dimensional transport algorithm presented here is only a first iteration. Several aspects of this algorithm will be developed further in the future. These include the application of the method to cases when the absorption coefficient corrected for induced emission is nonpositive, the optimum selection of the underrelaxation parameter for each spectral point, and the identification of improved boundary conditions.

Additional work is needed to make LORAN a practical tool for computing nonequilibrium flowfields with coupled radiation, especially when coupling effects are significant and many iterations are required to converge the coupled solution. Work is continuing to further reduce the time required to compute radiation by applying vectorization and other efficient strategies.

References

- [1] Gerald D. Walberg. A Review of Aerobraking for Mars Missions. IAF Paper 88-196, October 1988.
- [2] Claire E. Chapin. *Nonequilibrium Radiation and Ionization in Shock Waves*. PhD thesis, Purdue University, 1967.
- [3] Chul Park. Calculation of Nonequilibrium Radiation in AOTV Flight Regimes. AIAA Paper 84-0306, January 1984.
- [4] Graham Candler and Chul Park. The Computation of Radiation from Nonequilibrium Hypersonic Flows. AIAA Paper 88-2678, June 1988.
- [5] H.F. Nelson. Nonequilibrium Radiative Heating During Outer Planet Atmospheric Entry. *Journal of Spacecraft and Rockets*, pages 407–409, July-August 1983.
- [6] Ya.B. Zel'dovich and Yu.P. Raizer. *Physics of Shock Waves and High-Temperature Hydrodynamic Phenomena*, volume 1. Academic Press, New York, 1966.
- [7] S.S. Penner. *Radiation and Reentry*. Academic Press, New York, 1968.
- [8] B.F. Armaly. Continuum Absorption Coefficient of Atoms and Ions. Final Report NASA Grant NSG 1581, U. Missouri-Rolla, Dept. of Mech. and Aero. Eng., May 1979.

- [9] L.M. Biberman and G.E. Norman. Recombination Radiation and Bremsstrahlung of a Plasma. *Journal of Quantitative Spectroscopy and Radiative Transfer*, 3:221ff, 1963.
- [10] L.M. Biberman and G.E. Norman. On the Calculation of Photoionization Absorption. *Optics and Spectroscopy*, 8:230–232, 1960.
- [11] L.M. Biberman, G.E. Norman, and K.N. Ulyanov. On the Calculation of Photoionization Absorption in Atomic Gases. *Optics and Spectroscopy*, X(5):297–299, May 1961.
- [12] Jim J. Jones, Robert E. Boughner, Kenneth V. Haggard, John E. Nealy, David R. Schryer, and E.V. Zoby. Radiative Property Data for Venusian Entry. NASA SP 348, 1974.
- [13] T.E. Horton. Estimating the Importance of Ultraviolet Radiation for Reentry Simulation. AIAA Paper 71-467, April 1971.
- [14] T.E. Horton. Importance of Nonequilibrium in Estimating Radiative Heat Transfer Through a Flow. In *Progress in Astronautics and Aeronautics: Vol. 56*: . AIAA Paper, 1976.
- [15] J.H. Clarke and C. Ferrari. Gas Dynamics with Nonequilibrium Radiative and Collisional Ionization. *Physics of Fluids*, 8:2121, 1965.
- [16] L.A. Carlson. Approximation for Hypervelocity Nonequilibrium Radiating, Re-

- acting, and Conducting Stagnation Regions. AIAA Paper 88-2672, June 1988.
- [17] L.A. Carlson, G.J. Bobskill, and R.B. Greendyke. Comparison of Vibration-Dissociation Coupling and Radiative Heat Transfer Models for AOTV/AFE Flowfields. AIAA Paper 88-2673, June 1988.
- [18] R.B. Greendyke and L.C. Hartung. An Approximate Method for the Calculation of Nonequilibrium Radiative Heat Transfer. AIAA Paper 90-0135, January 1990.
- [19] Ellis E. Whiting, James O. Arnold, and Gilbert C. Lyle. A Computer Program for a Line-By-Line Calculation of Spectra from Diatomic Molecules and Atoms Using a Voigt Line Profile. NASA TN D-5088, March 1969.
- [20] Chul Park. Nonequilibrium Air Radiation (NEQAIR) Program: User's Manual. NASA TM- 86707, July 1985.
- [21] M.N. Ozisik. *Radiative Transfer and Interactions with Conduction and Convection*. Werbel and Peck, New York, 1973.
- [22] W.G. Vincenti and C.H. Kruger, Jr. *Introduction to Physical Gas Dynamics*. Robert E. Krieger Publishing Company, Malabar, Florida, 1982.
- [23] W.E. Nicolet. Advanced Methods for Calculating Radiation Transport in Ablation-Product Contaminated Boundary Layers. NASA CR 1656, September 1970.

- [24] W.E. Nicolet. Rapid Methods for Calculating Radiation Transport in the Entry Environment. NASA CR 2528, April 1975.
- [25] Charles W. Bolz, Jr. A Marching Method for Calculating Line and Continuum Radiation in High Energy Flowfields. NASA CR 3046, June 1979.
- [26] J.S. Truelove. Three-Dimensional Radiation in Absorbing-Emitting-Scattering Media Using the Discrete-Ordinates Approximation. *Journal of Quantitative Spectroscopy and Radiative Transfer*, 39(1):27–31, 1988.
- [27] Michael F. Modest. Modified Differential Approximation for Radiative Transfer in General Three-Dimensional Media. *Journal of Thermophysics and Heat Transfer*, 3(3), July 1989.
- [28] E.H. Cheng and M.N. Ozisik. Heat Transfer in a Radiating Nonsteady Three-Dimensional Stagnation Flow. *Applied Sci. Res.*, 28:185–197, October 1973.
- [29] D.K. Edwards, D.S. Babikian, P.L. Fuehrer, and W.C. Davy. Computational Volumetric Radiative Transfer for AOTV's. 1989 Annual Report NASA Ames Interchange No. NCA2-353, 1990.
- [30] Charles W. Bolz, Jr. An Algorithm for Selecting a Radiation Transport Subgrid for Ablation and Radiation Coupled Hypersonic Viscous Shock Layer Problems. NASA CR 144957, March 1976.
- [31] W.B. Olstad. Nongray Radiating Flow about Smooth Symmetric Bodies. *AIAA*

Journal, 9(1):122–130, January 1971.

- [32] E.V. Zoby, K. Sutton, W.B. Olstad, and J.N. Moss. Approximate Inviscid Radiating Flowfield Analysis for Outer Planet Entry Probes. In Raymond Viskanta, editor, *Progress in Astronautics and Aeronautics: Vol. 64: Outer Planet Entry Heating and Thermal Protection*, pages 42–64. AIAA Paper, 1979.
- [33] W.E. Nicolet. User’s Manual for the Generalized Radiation Transfer Code (RAD/EQUIL). NASA CR 116353, October 1969.
- [34] Kenneth Sutton. *Characteristics of Coupled Nongray Radiating Gas Flows with Ablation Products Effects About Blunt Bodies During Planetary Entries*. PhD thesis, North Carolina State University, Raleigh, North Carolina, 1973.
- [35] L.A. Carlson and T.A. Gally. Nonequilibrium Chemical and Radiation Coupling Phenomena in AOTV Flowfields. AIAA Paper 91-0569, January 1991.
- [36] Chul Park and Frank S. Milos. Computational Equations for Radiating and Ablating Shock Layers. AIAA Paper 90-0356, January 1990.
- [37] J.N. Moss and J.M. Price. Direct Simulation of AFE Forebody and Wake Flow with Thermal Radiation. NASA TM 100673, September 1988.
- [38] G.A. Bird. Nonequilibrium Radiation During Re-entry at 10 km/s. AIAA Paper 87-1543, June 1987.

- [39] Ann B. Carlson. *Direct Simulation Monte Carlo With Ionization and Radiation*. PhD thesis, North Carolina State University, 1990.
- [40] Ann B. Carlson and H. A. Hassan. Radiation Modeling with Direct Simulation Monte Carlo. AIAA Paper 91-1409, June 1991.
- [41] J.D. Teare, S. Georgiev, and R.A. Allen. Radiation from the Non-Equilibrium Shock Front. Research Report 112, AFCRL 937, Avco-Everett Research Laboratory, October 1961.
- [42] Richard A. Allen, J.C. Keck, and J.C. Camm. Non-Equilibrium Radiation from Shock Heated Nitrogen and a Determination of the Recombination Rate. Research Report 110, Avco-Everett Research Laboratory, June 1961.
- [43] Richard A. Allen, P.H. Rose, and J.C. Camm. Nonequilibrium and Equilibrium Radiation at Super-Satellite Re-entry Velocities. Research Report 156, BSD-TDR-62-349, Avco-Everett Research Laboratory, September 1962.
- [44] Richard A. Allen. Nonequilibrium Shock Front Rotational, Vibrational and Electronic Temperature Measurements. NASA CR 58673, August 1964.
- [45] Richard A. Allen, A. Textoris, and J. Wilson. Measurements of the Free-Bound and Free-Free Continua of Nitrogen, Oxygen, and Air. Research Report 195, Avco-Everett Research Laboratory, September 1964.
- [46] Bennett Kivel. Chemistry, Ionization and Radiation in the Nonequilibrium

Front of Normal Shocks in Air. Technical Report AMP 34, Avco-Everett Research Laboratory, September 1959.

- [47] William A. Page, Thomas N. Canning, Roger A. Craig, and Jack D. Stephenson. Measurements of Thermal Radiation of Air from the Stagnation Region of Blunt Bodies Traveling at velocities up to 31,000 Feet Per Second. NASA TM X-508, 1961.
- [48] W.A. Page. Shock-Layer Radiation of Blunt Bodies Traveling at Lunar Return Entry Velocities. Technical report, Presented at the IAS 31st Annual Meeting, New York, January 1963.
- [49] Thomas N. Canning and William A. Page. Measurements of Radiation from the Flow Fields of Bodies Flying at Speeds up to 13.4 Kilometers per Second. In W.C. Nelson, editor, *The High Temperature Aspects of Hypersonic Flow*, pages 569–581. The Macmillan Co., New York, 1964.
- [50] Robert M. Nerem. Measurements of Aerodynamic and Radiative Heating at Super-Orbital Velocities. Technical Report The Aerodynamic Laboratory 1598-1, Ohio State University, January 1964.
- [51] Robert M. Nerem. Stagnation Point Heat Transfer in High Enthalpy Gas Flows. Part II: Shock Layer Radiative Emission During Hypervelocity Re-entry. FDL TR 64-41 Part II, March 1964.

- [52] Robert M. Nerem and George H. Stickford. Stagnation Point Heat Transfer in High Enthalpy Gas Flows. Part I: Convective Heat Transfer in Partially Ionized Air. FDL TR 64-41 Part I, March 1964.
- [53] Robert M. Nerem. Radiating Flows around Re-entry Bodies. Technical Report The Aerodynamic Laboratory 1941-1, Ohio State University, September 1965.
- [54] R.M. Nerem and G. Stickford. Shock Tube Studies of Equilibrium Radiation. *AIAA Journal*, 3(6):1011–1018, June 1965.
- [55] R.M. Nerem, L.A. Carlson, and R.A. Golobic. Radiation-Gas-Dynamic Coupling Behind Reflected Shock Waves in Air. Technical report, Presented at the 12th International Congress on Applied Mechanics held at Stanford University, California, August 1968.
- [56] R.M. Nerem, L.A. Carlson, and J.E. Hartsel. Chemical Relaxation Phenomena Behind Normal Shock Waves in a Dissociated Freestream. *AIAA Journal*, 5(5):910–916, May 1967.
- [57] Robert A. Golobic and Robert M. Nerem. Shock Tube Measurements of End-Wall Radiative Heat Transfer in Air. *AIAA Journal*, 6(9):1741–1746, September 1968.
- [58] Robert A. Golobic and Robert M. Nerem. Shock Tube Studies of Radiative Transfer Effects in Air and Xenon. Technical report, NASA-LaRC Symposium

on Hypervelocity Radiating Flowfields for Earth and Planetary Entries, Hampton, VA, January 1971.

- [59] R.M. Nerem, R.A. Golobic, and J.B. Bader. Laboratory Studies of Radiative Transfer Effects in Shock-Heated Gases. In *Shock Tube Research: Proceedings of the Eighth International Shock Tube Symposium*, pages 19/1–19/19. Chapman and Hall, London, July 1971.
- [60] Robert M. Nerem. Radiative Transfer Effects Behind Reflected Shock Waves. Final Report Grant NGL-36-008-106, March 1972.
- [61] Norman R. Richardson. Project FIRE Instrumentation for Radiative Heating and Related Measurements. NASA TN D-3646, 1966.
- [62] John H. Lewis, Jr. and William I. Scallion. Flight Parameters and Vehicle Performance for Project FIRE Flight II, Launched May 22, 1965. NASA TN D-3569, August 1966.
- [63] Hans R. Griem. *Spectral Line Broadening by Plasmas*. Academic Press, New York, 1974.
- [64] William A. Page, Dale L. Compton, William J. Borucki, Donald L. Ciffone, and David M. Cooper. Radiative Transfer in Inviscid Non-Adiabatic Stagnation Region Shock Layers. AIAA Paper 68-784, June 1968.
- [65] G. Herzberg. *Molecular Spectra and Molecular Structure. I. Spectra of Diatomic*

Molecules. D. Van Nostrand Co., Inc., Princeton, New Jersey, 1950.

- [66] W.L. Wiese, M.W. Smith, and B.M. Glennon. *Atomic Transition Probabilities; Volume I: Hydrogen Through Neon*. NSRDS-NBS 4. National Bureau of Standards, May 1966.
- [67] Chul Park. *Nonequilibrium Hypersonic Aerothermodynamics*. Wiley, New York, 1990.
- [68] Ellis Whiting, 1989. Private Communication.
- [69] Peter A. Gnoffo, Roop N. Gupta, and Judy L. Shinn. Conservation Equations and Physical Models for Hypersonic Air Flows in Thermal and Chemical Nonequilibrium. NASA TP 2867, February 1989.
- [70] E. M. Sparrow and R. D. Cess. *Radiation Heat Transfer*. Brooks/Cole Publishing Company, Belmont, California, 1966.
- [71] Peter A. Gnoffo. Upwind-Biased Point-Implicit Relaxation Strategies for Viscous Hypersonic Flows. AIAA Paper 89-1972, June 1989.
- [72] Chul Park. Assessment of Two-Temperature Kinetic Model for Ionizing Air. *Journal of Thermophysics and Heat Transfer*, 3(3):233–244, July 1989.
- [73] Surendra P. Sharma, Walter D. Gillespie, and Scott A. Meyer. Shock Front Radiation Measurements in Air. AIAA Paper 91-0573, January 1991.

- [74] John W. Bond, Jr., Kenneth M. Watson, and Jasper A. Welch, Jr. *Atomic Theory of Gas Dynamics*. Addison-Wesley, Reading, Massachusetts, 1965.
- [75] Peter A. Gnoffo. Asynchronous, Macrotasked Relaxation Strategies For the Solution of Viscous Hypersonic Flows. AIAA Paper 91-1579, June 1991.
- [76] Dona L. Cauchon. Radiative Heating Results from the FIRE II Flight Experiment at a Reentry Velocity of 11.4 Kilometers per Second. NASA TM X-1402, July 1967.
- [77] Dona L. Cauchon, Charles W. McKee, and Elden S. Cornette. Spectral Measurements of Gas-Cap Radiation During Project FIRE Flight Experiments at Reentry Velocities Near 11.4 Kilometers per Second. NASA TM X-1389, October 1967.
- [78] Elden S. Cornette. Forebody Temperatures and Calorimeter Heating Rates Measured During Project FIRE II Reentry at 11.35 Kilometers per Second. NASA TM X-1305, November 1966.
- [79] Richard C. Dingeldein. Radiative and Total Heating Rates Obtained from Project FIRE Reentries at 37,000 Feet per Second. Technical report, December 1965. Paper presented at the AFFDL/ASSET Advanced Lifting Reentry Technology Symposium.
- [80] Robert A. Mitcheltree and Peter A. Gnoffo. Thermochemical Nonequilibrium Issues for Earth Reentry of Mars Mission Vehicles. AIAA Paper 90-1698, June

1990.

- [81] F. McNeil Cheatwood, Fred R. DeJarnette, and H. Harris Hamilton, II. Geometrical Description for a Proposed Aeroassist Flight Experiment Vehicle. NASA TM- 87714, July 1986.
- [82] J.N. Moss, G.A. Bird, and V.K. Dogra. Nonequilibrium Thermal Radiation for an AFE Vehicle. AIAA Paper 88-0081, January 1988.
- [83] Peter A. Gnoffo. Code Calibration Program in Support of the Aeroassist Flight Experiment. *Journal of Spacecraft & Rockets*, 27(2):131–142, March-April 1990.
- [84] H. Harris Hamilton, II, Roop N. Gupta, and Jim J. Jones. Flight Stagnation-Point Heating Calculations on Aeroassist Flight Experiment Vehicle. *Journal of Spacecraft & Rockets*, 28(1), January-February 1991.
- [85] Robert B. Greendyke, 1991. Private Communication.
- [86] R.B. Greendyke and L.C. Hartung. An Approximate Method for the Calculation of Nonequilibrium Radiative Heat Transfer. *Journal of Spacecraft & Rockets*, 28(1), January-February 1991.
- [87] Chul Park. Assessment of Two-Temperature Kinetic Model for Ionizing Air. AIAA Paper 87-1574, June 1987.
- [88] Surendra P. Sharma, Winifred M. Huo, and Chul Park. The Rate Parameters for Coupled Vibration-Dissociation in a Generalized SSH Approximation -

Schwartz, Slawsky, and Herzfeld. AIAA Paper 88-2714, June 1988.

- [89] R.C. Millikan and D.R. White. Systematics of Vibrational Relaxation. *Journal of Chemical Physics*, 39(12):3209–3213, December 1963.
- [90] Chul Park. Problems of Rate Chemistry in the Flight Regimes of Aeroassisted Orbital Transfer Vehicles. In H.F. Nelson, editor, *Progress in Astronautics and Aeronautics: Thermal Design of Aeroassisted Orbital Transfer Vehicles*, volume 96, pages 511–537. AIAA Paper, 1985.
- [91] Surendra P. Sharma and Chul Park. Survey of Simulation and Diagnostic Techniques for Hypersonic Nonequilibrium Flows. *Journal of Thermophysics*, 4(2):129–142, April 1990.
- [92] Peter A. Gnoffo, 1991. Private Communication.
- [93] Chul Park. Two-Temperature Interpretation of Dissociation Rate Data for N_2 and O_2 . AIAA Paper 88-0458, January 1988.
- [94] Michael G. Dunn and Sang-Wook Kang. Theoretical and Experimental Studies of Reentry Plasmas. NASA CR 2232, 1973.
- [95] Chul Park, John T. Howe, Richard L. Jaffe, and Graham V. Candler. Chemical-Kinetic Problems of Future NASA Missions. AIAA Paper 91-0464, January 1991.

- [96] Roop N. Gupta, Jerrold M. Yos, Richard A. Thompson, and Kam-Pui Lee. A Review of Reaction Rates and Thermodynamic and Transport Properties for an 11-Species Air Model for Chemical and Thermal Nonequilibrium Calculations to 30 000 K. NASA RP 1232, August 1990.
- [97] Robert A. Mitcheltree. A Parametric Study of Dissociation and Ionization Models at 12 km/sec. AIAA Paper 91-1368, June 1991.
- [98] L.A. Carlson and T.A. Gally. The Effect of Electron Temperature and Impact Ionization on Martian Return AOTV Flowfields. AIAA Paper 89-1729, June 1989.
- [99] Peter A. Gnoffo. An Upwind-Biased, Point-Implicit Relaxation Algorithm for Viscous, Compressible Perfect-Gas Flows. NASA TP 2953, February 1990.
- [100] Dale A. Anderson, John C. Tannehill, and Richard H. Pletcher. *Computational Fluid Mechanics and Heat Transfer*. Hemisphere Publishing Corporation, New York, 1984.

A Gaussian Units

Much of the work in radiation has historically been done in the Gaussian system of units. This system introduces the particular oddity of measuring the electron charge in statcoulombs. As this particular unit of measure is uncommon, the following information is provided for the reader.

In the Gaussian system of units:

| | | |
|------------------------------|----------|--------------------------|
| $c=2.9979 \times 10^{10}$ | cm/sec | speed of light in vacuum |
| $e=4.80286 \times 10^{-10}$ | statcoul | electron charge |
| $h=6.6262 \times 10^{-27}$ | erg-sec | Planck's constant |
| $k=1.3807 \times 10^{-16}$ | erg/K | Boltzmann's constant |
| $m_e=9.1095 \times 10^{-28}$ | g | electron mass. |

The following relations hold among several of these quantities:

The Bohr radius, a_0 , is given by

$$a_0 = \frac{h^2}{4\pi^2 m_e e^2} = 0.52918 \times 10^{-8} \text{ cm} \quad (\text{A.1})$$

The fine structure constant, α , a dimensionless quantity, is

$$\alpha = \frac{2\pi e^2}{hc} = 7.292 \times 10^{-3} \quad (\text{A.2})$$

B Finite Volume Formulation of Radiative Transport

B.1 Finite Volume Development

The following development is for the modified differential approximation for radiative transport as reported by Modest [27]. The method has been reexpressed for a non-gray, non-scattering and nonequilibrium medium.

The governing equations for the medium flux and incident intensity are:

$$\vec{\nabla} \cdot \vec{q}_{\nu\text{R}} = 4\pi j_{\nu}^e - \kappa'_{\nu} G_{\nu} \quad (\text{B.1})$$

$$\vec{\nabla} G_{\nu} = -3\kappa'_{\nu} \vec{q}_{\nu\text{R}} \quad (\text{B.2})$$

In what follows the R subscript on the radiative heat flux will be dropped for clarity. The first of these equations is a scalar equation, while the second is a vector equation. There are accordingly four unknowns for each spectral frequency chosen: G_{ν} , q_{ν_x} , q_{ν_y} , and q_{ν_z} . The only quantity required for coupling to a Computational Fluid Dynamics (CFD) solution, however, is the divergence of the radiative flux, $\vec{\nabla} \cdot \vec{q}_{\text{R}}$. This quantity is given as a function of G by integrating Eq. B.1 over frequency, so that a solution for the single unknown G_{ν} at each spectral frequency is sufficient.

To obtain a form of these equations suitable for a finite-volume solution, first rearrange Eq. B.2:

$$\frac{1}{\kappa'_{\nu}} \vec{\nabla} G_{\nu} = -3\vec{q}_{\nu} \quad (\text{B.3})$$

Now take the dot product of this equation to allow the substitution of Eq. B.1:

$$\vec{\nabla} \cdot \left(\frac{1}{\kappa'_\nu} \vec{\nabla} G_\nu \right) = -3\vec{\nabla} \cdot \vec{q}_\nu = -12\pi j_\nu^e + 3\kappa'_\nu G_\nu \quad (\text{B.4})$$

So now rearranging,

$$\vec{\nabla} \cdot \left(\frac{1}{\kappa'_\nu} \vec{\nabla} G_\nu \right) = 3\kappa'_\nu G_\nu - 12\pi j_\nu^e \quad (\text{B.5})$$

In the finite volume approach, this is now to be integrated over the volume of a single grid cell, V .

$$\int \int \int_V \vec{\nabla} \cdot \left(\frac{1}{\kappa'_\nu} \vec{\nabla} G_\nu \right) dV = \int \int \int_V (3\kappa'_\nu G_\nu - 12\pi j_\nu^e) dV \approx V (3\kappa'_\nu G_\nu - 12\pi j_\nu^e) \quad (\text{B.6})$$

Then by application of Gauss' theorem (the divergence theorem), the volume integral on the left-hand-side can be transformed to a surface integral.

$$\int \int_S \left(\frac{1}{\kappa'_\nu} \vec{\nabla} G_\nu \cdot \hat{n} \right) da = V (3\kappa'_\nu G_\nu - 12\pi j_\nu^e) \quad (\text{B.7})$$

The integral is performed by assuming that the absorption coefficient κ'_ν and the gradient of the incident intensity $\vec{\nabla} G_\nu$ are constant on each cell face. The integral then becomes a summation over the six faces of the cell. The notation used for the cell geometry is that of Gnoffo [99], where I , J , and K denote cell centers, and i , j , and k denote cell faces. Then

$$\begin{aligned} & \left[\left(\frac{1}{\kappa'_\nu} \vec{\nabla} G_\nu \right)_{i+1} \cdot \hat{n}_{i+1} a_{i+1} - \left(\frac{1}{\kappa'_\nu} \vec{\nabla} G_\nu \right)_i \cdot \hat{n}_i a_i \right]_{J,K} \\ & + \left[\left(\frac{1}{\kappa'_\nu} \vec{\nabla} G_\nu \right)_{j+1} \cdot \hat{n}_{j+1} a_{j+1} - \left(\frac{1}{\kappa'_\nu} \vec{\nabla} G_\nu \right)_j \cdot \hat{n}_j a_j \right]_{I,K} \end{aligned}$$

$$\begin{aligned}
& + \left[\left(\frac{1}{\kappa'_\nu} \vec{\nabla} G_\nu \right)_{k+1} \cdot \hat{n}_{k+1} a_{k+1} - \left(\frac{1}{\kappa'_\nu} \vec{\nabla} G_\nu \right)_k \cdot \hat{n}_k a_k \right]_{I,J} \\
& = V (3\kappa'_\nu G_\nu - 12\pi j_\nu^e)_{I,J,K}
\end{aligned} \tag{B.8}$$

For the nongray gas found in a shock layer, the radiative properties κ'_ν and j_ν^e vary over orders of magnitude at various locations and frequencies. To minimize the numerical difficulties that this variation can introduce, some kind of normalization is desired. Define

$$\bar{j}_\nu = \frac{\sum_{\text{cells}} j_\nu^e}{N_{\text{cells}}} \tag{B.9}$$

and

$$\bar{\kappa}_\nu = \frac{\sum_{\text{cells}} \kappa'_\nu}{N_{\text{cells}}} \tag{B.10}$$

Both these quantities are constant for each frequency considered, and provide a measure of the approximate magnitude of the emission and absorption at that frequency. Figure B.1 is an example of the variation of these average coefficients for the Mars return test case presented in Ch. 6 and demonstrates the wide variation in radiation properties for various frequencies in a single flowfield.

Proceeding with the finite volume development, now divide Eq. B.8 by \bar{j}_ν on both sides, and also multiply terms containing G_ν by 1 in the form of $\bar{\kappa}_\nu / \bar{\kappa}_\nu$. Define a new variable $\gamma_\nu = G_\nu / (\bar{j}_\nu \bar{\kappa}_\nu)$. Then Eq. B.8 becomes:

$$\begin{aligned}
& \left[\left(\frac{\bar{\kappa}_\nu}{\kappa'_\nu} \vec{\nabla}, \gamma_\nu \right)_{i+1} \cdot \hat{n}_{i+1} a_{i+1} - \left(\frac{\bar{\kappa}_\nu}{\kappa'_\nu} \vec{\nabla}, \gamma_\nu \right)_i \cdot \hat{n}_i a_i \right]_{J,K} \\
& + \left[\left(\frac{\bar{\kappa}_\nu}{\kappa'_\nu} \vec{\nabla}, \gamma_\nu \right)_{j+1} \cdot \hat{n}_{j+1} a_{j+1} - \left(\frac{\bar{\kappa}_\nu}{\kappa'_\nu} \vec{\nabla}, \gamma_\nu \right)_j \cdot \hat{n}_j a_j \right]_{I,K}
\end{aligned}$$

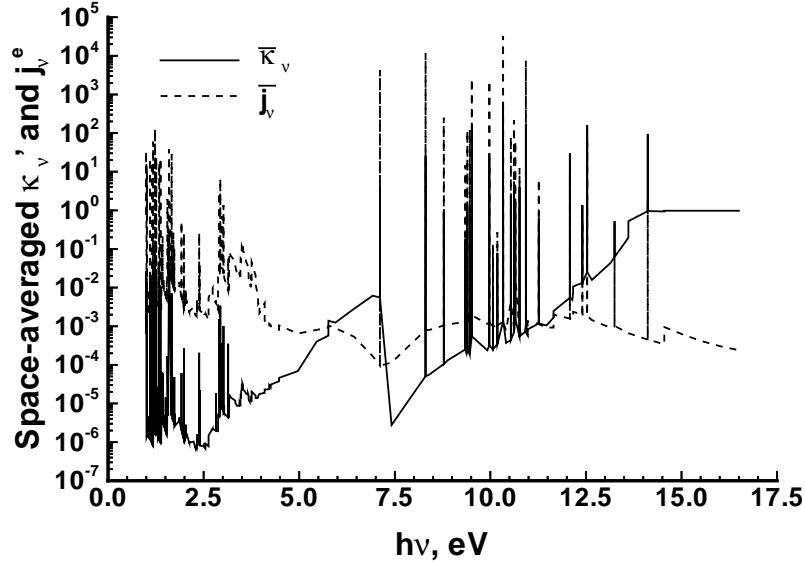


Figure B.1. Variation of $\bar{\kappa}_\nu$ and \bar{j}_ν for a Mars Return Flowfield

$$\begin{aligned}
 & + \left[\left(\frac{\bar{\kappa}_\nu}{\kappa'_\nu} \vec{\nabla}, \nu \right)_{k+1} \cdot \hat{n}_{k+1} a_{k+1} - \left(\frac{\bar{\kappa}_\nu}{\kappa'_\nu} \vec{\nabla}, \nu \right)_k \cdot \hat{n}_k a_k \right]_{I,J} \\
 & = V \left(3\bar{\kappa}_\nu \kappa'_{\nu, \nu} - 12\pi \frac{j_\nu^e}{j_\nu} \right)_{I,J,K}
 \end{aligned} \tag{B.11}$$

This formulation reduces the variation of the unknown, κ_ν , and of the coefficients of the equation, making the numerical solution easier.

Now consider the j and $j + 1$ cell faces in an axisymmetric flow. The gradient of κ_ν has no component in the circumferential direction, while the surface normal \hat{n} on these faces is entirely in the circumferential direction. Therefore the dot product of these two quantities is zero and the terms on these faces drop out. This is a mathematical expression of the fact that there is no flux through these cell faces in an axisymmetric flow. The j and J subscripts then become superfluous, and will be omitted in the remainder of this development.

Since the flowfield grid is not orthogonal, it is necessary to use a generalized transformation to obtain finite difference expressions for the gradients in Eq. B.11. The elements of such a transformation are repeated below from Anderson et al. [100, Sec. 5-6.2], specialized to the case of an axisymmetric flowfield. Second order accurate central difference expressions are used to obtain the necessary partial derivatives, where ξ , η , and ζ are the coordinates of the orthogonal and uniformly spaced computational grid corresponding to the i , j , and k grid directions, respectively.

$$x_\xi = \frac{x_{i+1,k} - x_{i-1,k}}{2} \quad (\text{B.12})$$

$$x_\eta = 0 \quad (\text{B.13})$$

$$x_\zeta = \frac{x_{i,k+1} - x_{i,k-1}}{2} \quad (\text{B.14})$$

$$y_\xi = 0 \quad (\text{B.15})$$

$$y_\eta = \frac{y_{i,j+1,k} - y_{i,j-1,k}}{2} = x_{i,k} \sin \theta \quad (\text{B.16})$$

where

$$\theta = 2. * \arctan \frac{y}{x} \big|_{\text{cell corner}} \quad (\text{B.17})$$

$$y_\zeta = 0 \quad (\text{B.18})$$

$$z_\xi = \frac{z_{i+1,k} - z_{i-1,k}}{2} \quad (\text{B.19})$$

$$z_\eta = 0 \quad (\text{B.20})$$

$$z_\zeta = \frac{z_{i,k+1} - z_{i,k-1}}{2} \quad (\text{B.21})$$

At the boundaries first order backward differences are applied, except for the axis of symmetry boundary. At this boundary the coordinates of a “ghost” cell can be obtained through reflection. Second order accurate central differencing can therefore be applied at this boundary. The Jacobian of the transformation can then be obtained from:

$$\hat{J} = \frac{1}{x_\xi y_\eta z_\zeta - x_\zeta y_\eta z_\xi} \quad (\text{B.22})$$

while the metrics of the transformation are given by:

$$\xi_x = \hat{J} y_\eta z_\zeta \quad (\text{B.23})$$

$$\xi_y = 0 \quad (\text{B.24})$$

$$\xi_z = -\hat{J} x_\zeta y_\eta \quad (\text{B.25})$$

$$\eta_x = 0 \quad (\text{B.26})$$

$$\eta_y = \hat{J} (x_\xi z_\zeta - x_\zeta z_\xi) \quad (\text{B.27})$$

$$\eta_z = 0 \quad (\text{B.28})$$

$$\zeta_x = -\hat{J} y_\eta z_\xi \quad (\text{B.29})$$

$$\zeta_y = 0 \quad (\text{B.30})$$

$$\zeta_z = \hat{J} x_\xi y_\eta \quad (\text{B.31})$$

The first derivatives which appear in the gradient terms are then obtained from

$$\frac{\partial}{\partial x} = \xi_x \frac{\partial}{\partial \xi} + \zeta_x \frac{\partial}{\partial \zeta} \quad (\text{B.32})$$

$$\frac{\partial}{\partial y} = \eta_y \frac{\partial}{\partial \eta} \quad (\text{B.33})$$

$$\frac{\partial}{\partial z} = \xi_z \frac{\partial}{\partial \xi} + \zeta_z \frac{\partial}{\partial \zeta} \quad (\text{B.34})$$

so the gradient can be expanded as:

$$\vec{\nabla}_{,\nu} = \left(\xi_x \frac{\partial_{,\nu}}{\partial \xi} + \zeta_x \frac{\partial_{,\nu}}{\partial \zeta} \right) \hat{i} + \eta_y \frac{\partial_{,\nu}}{\partial \eta} \hat{j} + \left(\xi_z \frac{\partial_{,\nu}}{\partial \xi} + \zeta_z \frac{\partial_{,\nu}}{\partial \zeta} \right) \hat{k} \quad (\text{B.35})$$

The y-derivative can be omitted since there is no circumferential variation of $_{,\nu}$ in the case of axisymmetric flow. Collecting terms then yields

$$\vec{\nabla}_{,\nu} = \left(\xi_x \hat{i} + \xi_z \hat{k} \right) \frac{\partial_{,\nu}}{\partial \xi} + \left(\zeta_x \hat{i} + \zeta_z \hat{k} \right) \frac{\partial_{,\nu}}{\partial \zeta} = \vec{\nabla} \xi \frac{\partial_{,\nu}}{\partial \xi} + \vec{\nabla} \zeta \frac{\partial_{,\nu}}{\partial \zeta} \quad (\text{B.36})$$

Now note that the combination $\hat{n}a$ is just the directed area of the cell face, or \vec{a} .

The finite volume expression, Eq. B.11, can now be reformulated as:

$$\begin{aligned} & \frac{\bar{\kappa}_\nu}{\kappa'_{\nu_{i+1,K}}} \left(\vec{\nabla} \xi_{i+1,K} \frac{\partial_{,\nu}}{\partial \xi_{i+1,K}} + \vec{\nabla} \zeta_{i+1,K} \frac{\partial_{,\nu}}{\partial \zeta_{i+1,K}} \right) \cdot \vec{a}_{i+1,K} \\ & - \frac{\bar{\kappa}_\nu}{\kappa'_{\nu_{i,K}}} \left(\vec{\nabla} \xi_{i,K} \frac{\partial_{,\nu}}{\partial \xi_{i,K}} + \vec{\nabla} \zeta_{i,K} \frac{\partial_{,\nu}}{\partial \zeta_{i,K}} \right) \cdot \vec{a}_{i,K} \\ & + \frac{\bar{\kappa}_\nu}{\kappa'_{\nu_{I,k+1}}} \left(\vec{\nabla} \xi_{I,k+1} \frac{\partial_{,\nu}}{\partial \xi_{I,k+1}} + \vec{\nabla} \zeta_{I,k+1} \frac{\partial_{,\nu}}{\partial \zeta_{I,k+1}} \right) \cdot \vec{a}_{I,k+1} \\ & - \frac{\bar{\kappa}_\nu}{\kappa'_{\nu_{I,k}}} \left(\vec{\nabla} \xi_{I,k} \frac{\partial_{,\nu}}{\partial \xi_{I,k}} + \vec{\nabla} \zeta_{I,k} \frac{\partial_{,\nu}}{\partial \zeta_{I,k}} \right) \cdot \vec{a}_{I,k} \\ & = V_{I,K} \left(3\bar{\kappa}_\nu \kappa'_{\nu,\nu} - 12\pi \frac{j_\nu^e}{j_\nu} \right)_{I,K} \end{aligned} \quad (\text{B.37})$$

The radiative properties κ'_ν and j_ν^e are known at cell centers (I, K) . The required values of κ'_ν at the cell faces can be obtained by averaging the values at the two nearest cell centers. Then for instance

$$\frac{1}{\kappa'_{\nu_{i+1,K}}} = \frac{1}{2} \left(\frac{1}{\kappa'_{\nu_{I+1,K}}} + \frac{1}{\kappa'_{\nu_{I,K}}} \right) \quad (\text{B.38})$$

This average has been found to produce better stability than the alternate form with $2/(\kappa'_{\nu_{I+1,K}} + \kappa'_{\nu_{I,K}})$ because of the extreme variation of the absorption coefficient near the freestream boundary in particular. The first derivatives of ν in computational space at the cell faces are obtained by second-order accurate central differences, as follows:

$$\frac{\partial \nu}{\partial \xi}_{i+1,K} = (\nu_{I+1,K} - \nu_{I,K}) \quad (\text{B.39})$$

$$\frac{\partial \nu}{\partial \zeta}_{i+1,K} = \frac{1}{2} \left(\frac{\nu_{I+1,K+1} - \nu_{I+1,K-1}}{2} + \frac{\nu_{I,K+1} - \nu_{I,K-1}}{2} \right) \quad (\text{B.40})$$

The next two differences are the same but with a shift in the i and I indices:

$$\frac{\partial \nu}{\partial \xi}_{i,K} = (\nu_{I,K} - \nu_{I-1,K}) \quad (\text{B.41})$$

$$\frac{\partial \nu}{\partial \zeta}_{i,K} = \frac{1}{2} \left(\frac{\nu_{I,K+1} - \nu_{I,K-1}}{2} + \frac{\nu_{I-1,K+1} - \nu_{I-1,K-1}}{2} \right) \quad (\text{B.42})$$

Along the normal cell faces:

$$\frac{\partial \nu}{\partial \xi}_{I,k+1} = \frac{1}{2} \left(\frac{\nu_{I+1,K+1} - \nu_{I-1,K+1}}{2} + \frac{\nu_{I+1,K} - \nu_{I-1,K}}{2} \right) \quad (\text{B.43})$$

$$\frac{\partial \nu}{\partial \zeta}_{I,k+1} = (\nu_{I,K+1} - \nu_{I,K}) \quad (\text{B.44})$$

And again the next two differences are the same except for a shift in the k and K indices:

$$\frac{\partial \nu}{\partial \xi}_{I,k} = \frac{1}{2} \left(\frac{\nu_{I+1,K} - \nu_{I-1,K}}{2} + \frac{\nu_{I+1,K-1} - \nu_{I-1,K-1}}{2} \right) \quad (\text{B.45})$$

$$\frac{\partial \nu}{\partial \zeta}_{I,k} = (\nu_{I,K} - \nu_{I,K-1}) \quad (\text{B.46})$$

All these expressions can now be substituted back into Eq. B.37, to obtain:

$$\begin{aligned}
& \frac{\bar{\kappa}_\nu}{\kappa'_{\nu_{i+1,K}}} \left[\vec{\nabla} \xi_{i+1,K} (, \nu_{I+1,K} - , \nu_{I,K}) \right. \\
& + \vec{\nabla} \zeta_{i+1,K} \frac{1}{2} \left(\frac{, \nu_{I+1,K+1} - , \nu_{I+1,K-1}}{2} + \frac{, \nu_{I,K+1} - , \nu_{I,K-1}}{2} \right) \left. \right] \cdot \vec{a}_{i+1,K} \\
& - \frac{\bar{\kappa}_\nu}{\kappa'_{\nu_{i,K}}} \left[\vec{\nabla} \xi_{i,K} (, \nu_{I,K} - , \nu_{I-1,K}) \right. \\
& + \vec{\nabla} \zeta_{i,K} \frac{1}{2} \left(\frac{, \nu_{I,K+1} - , \nu_{I,K-1}}{2} + \frac{, \nu_{I-1,K+1} - , \nu_{I-1,K-1}}{2} \right) \left. \right] \cdot \vec{a}_{i,K} \\
& + \frac{\bar{\kappa}_\nu}{\kappa'_{\nu_{I,k+1}}} \left[\vec{\nabla} \xi_{I,k+1} \frac{1}{2} \left(\frac{, \nu_{I+1,K+1} - , \nu_{I-1,K+1}}{2} + \frac{, \nu_{I+1,K} - , \nu_{I-1,K}}{2} \right) \right. \\
& \quad \left. + \vec{\nabla} \zeta_{I,k+1} (, \nu_{I,K+1} - , \nu_{I,K}) \right] \cdot \vec{a}_{I,k+1} \\
& - \frac{\bar{\kappa}_\nu}{\kappa'_{\nu_{I,k}}} \left[\vec{\nabla} \xi_{I,k} \frac{1}{2} \left(\frac{, \nu_{I+1,K} - , \nu_{I-1,K}}{2} + \frac{, \nu_{I+1,K-1} - , \nu_{I-1,K-1}}{2} \right) \right. \\
& \quad \left. + \vec{\nabla} \zeta_{I,k} (, \nu_{I,K} - , \nu_{I,K-1}) \right] \cdot \vec{a}_{I,k} = V_{I,K} \left(3\bar{\kappa}_\nu \kappa'_{\nu, \nu} - 12\pi \frac{j_\nu^e}{j_\nu} \right)_{I,K} \quad (B.47)
\end{aligned}$$

Carrying out the dot products and collecting terms results in:

$$\begin{aligned}
& d_{1, \nu_{I+1,K+1}} + d_{2, \nu_{I+1,K}} + d_{3, \nu_{I+1,K-1}} + d_{4, \nu_{I,K+1}} + d_{5, \nu_{I,K}} + d_{6, \nu_{I,K-1}} \\
& + d_{7, \nu_{I-1,K+1}} + d_{8, \nu_{I-1,K}} + d_{9, \nu_{I-1,K-1}} = -12\pi V_{I,K} \frac{j_{\nu_{I,K}}^e}{j_\nu} \quad (B.48)
\end{aligned}$$

where

$$d_1 = \frac{1}{4} \frac{\bar{\kappa}_\nu}{\kappa'_{\nu_{i+1,K}}} \vec{\nabla} \zeta_{i+1,K} \cdot \vec{a}_{i+1,K} + \frac{1}{4} \frac{\bar{\kappa}_\nu}{\kappa'_{\nu_{I,k+1}}} \vec{\nabla} \xi_{I,k+1} \cdot \vec{a}_{I,k+1} \quad (B.49)$$

$$d_2 = \frac{\bar{\kappa}_\nu}{\kappa'_{\nu_{i+1,K}}} \vec{\nabla} \xi_{i+1,K} \cdot \vec{a}_{i+1,K} + \frac{1}{4} \frac{\bar{\kappa}_\nu}{\kappa'_{\nu_{I,k+1}}} \vec{\nabla} \xi_{I,k+1} \cdot \vec{a}_{I,k+1} - \frac{1}{4} \frac{\bar{\kappa}_\nu}{\kappa'_{\nu_{I,k}}} \vec{\nabla} \xi_{I,k} \cdot \vec{a}_{I,k} \quad (B.50)$$

$$d_3 = -\frac{1}{4} \frac{\bar{\kappa}_\nu}{\kappa'_{\nu_{i+1,K}}} \vec{\nabla} \zeta_{i+1,K} \cdot \vec{a}_{i+1,K} - \frac{1}{4} \frac{\bar{\kappa}_\nu}{\kappa'_{\nu_{I,k}}} \vec{\nabla} \xi_{I,k} \cdot \vec{a}_{I,k} \quad (B.51)$$

$$d_4 = \frac{1}{4} \frac{\bar{\kappa}_\nu}{\kappa'_{\nu_{i+1,K}}} \vec{\nabla} \zeta_{i+1,K} \cdot \vec{a}_{i+1,K} - \frac{1}{4} \frac{\bar{\kappa}_\nu}{\kappa'_{\nu_{i,K}}} \vec{\nabla} \zeta_{i,K} \cdot \vec{a}_{i,K} + \frac{\bar{\kappa}_\nu}{\kappa'_{\nu_{I,k+1}}} \vec{\nabla} \zeta_{I,k+1} \cdot \vec{a}_{I,k+1} \quad (\text{B.52})$$

$$\begin{aligned} d_5 = & -\frac{\bar{\kappa}_\nu}{\kappa'_{\nu_{i+1,K}}} \vec{\nabla} \xi_{i+1,K} \cdot \vec{a}_{i+1,K} - \frac{\bar{\kappa}_\nu}{\kappa'_{\nu_{i,K}}} \vec{\nabla} \xi_{i,K} \cdot \vec{a}_{i,K} \\ & - \frac{\bar{\kappa}_\nu}{\kappa'_{\nu_{I,k+1}}} \vec{\nabla} \zeta_{I,k+1} \cdot \vec{a}_{I,k+1} - \frac{\bar{\kappa}_\nu}{\kappa'_{\nu_{I,k}}} \vec{\nabla} \zeta_{I,k} \cdot \vec{a}_{I,k} - 3V_{I,K} \bar{\kappa}_\nu \kappa'_{\nu_{I,K}} \end{aligned} \quad (\text{B.53})$$

$$d_6 = -\frac{1}{4} \frac{\bar{\kappa}_\nu}{\kappa'_{\nu_{i+1,K}}} \vec{\nabla} \zeta_{i+1,K} \cdot \vec{a}_{i+1,K} + \frac{1}{4} \frac{\bar{\kappa}_\nu}{\kappa'_{\nu_{i,K}}} \vec{\nabla} \zeta_{i,K} \cdot \vec{a}_{i,K} + \frac{\bar{\kappa}_\nu}{\kappa'_{\nu_{I,k}}} \vec{\nabla} \zeta_{I,k} \cdot \vec{a}_{I,k} \quad (\text{B.54})$$

$$d_7 = -\frac{1}{4} \frac{\bar{\kappa}_\nu}{\kappa'_{\nu_{i,K}}} \vec{\nabla} \zeta_{i,K} \cdot \vec{a}_{i,K} - \frac{1}{4} \frac{\bar{\kappa}_\nu}{\kappa'_{\nu_{I,k+1}}} \vec{\nabla} \xi_{I,k+1} \cdot \vec{a}_{I,k+1} \quad (\text{B.55})$$

$$d_8 = \frac{\bar{\kappa}_\nu}{\kappa'_{\nu_{i,K}}} \vec{\nabla} \xi_{i,K} \cdot \vec{a}_{i,K} - \frac{1}{4} \frac{\bar{\kappa}_\nu}{\kappa'_{\nu_{I,k+1}}} \vec{\nabla} \xi_{I,k+1} \cdot \vec{a}_{I,k+1} + \frac{1}{4} \frac{\bar{\kappa}_\nu}{\kappa'_{\nu_{I,k}}} \vec{\nabla} \xi_{I,k} \cdot \vec{a}_{I,k} \quad (\text{B.56})$$

$$d_9 = \frac{1}{4} \frac{\bar{\kappa}_\nu}{\kappa'_{\nu_{i,K}}} \vec{\nabla} \zeta_{i,K} \cdot \vec{a}_{i,K} + \frac{1}{4} \frac{\bar{\kappa}_\nu}{\kappa'_{\nu_{I,k}}} \vec{\nabla} \xi_{I,k} \cdot \vec{a}_{I,k} \quad (\text{B.57})$$

The dot products of the metrics with the cell face directed areas which appear in these coefficients are determined by the grid geometry. These can be written as follows:[99]

$$\begin{aligned} \vec{\nabla} \xi_{i,K} \cdot \vec{a}_{i,K} = & \left[\frac{V_{I,K}(\vec{a}_{i-1,K} + \vec{a}_{i,K}) + V_{I-1,K}(\vec{a}_{i,K} + \vec{a}_{i+1,K})}{4V_{I,K}V_{I-1,K}} \right] \cdot \vec{a}_{i,K} = \\ & \frac{V_{I,K}(a_{x_{i-1,K}}a_{x_{i,K}} + a_{z_{i-1,K}}a_{z_{i,K}} + a_{x_{i,K}}a_{x_{i,K}} + a_{z_{i,K}}a_{z_{i,K}})}{4V_{I,K}V_{I-1,K}} \\ & + \frac{V_{I-1,K}(a_{x_{i,K}}a_{x_{i,K}} + a_{z_{i,K}}a_{z_{i,K}} + a_{x_{i+1,K}}a_{x_{i,K}} + a_{z_{i+1,K}}a_{z_{i,K}})}{4V_{I,K}V_{I-1,K}} \end{aligned} \quad (\text{B.58})$$

$$\begin{aligned} \vec{\nabla} \xi_{I,k} \cdot \vec{a}_{I,k} = & \left[\frac{V_{I,K}(\vec{a}_{i,K-1} + \vec{a}_{i+1,K-1}) + V_{I,K-1}(\vec{a}_{i,K} + \vec{a}_{i+1,K})}{4V_{I,K}V_{I,K-1}} \right] \cdot \vec{a}_{I,k} = \\ & \frac{V_{I,K}(a_{x_{i,K-1}}a_{x_{I,k}} + a_{z_{i,K-1}}a_{z_{I,k}} + a_{x_{i+1,K-1}}a_{x_{I,k}} + a_{z_{i+1,K-1}}a_{z_{I,k}})}{4V_{I,K}V_{I,K-1}} \\ & + \frac{V_{I,K-1}(a_{x_{i,K}}a_{x_{I,k}} + a_{z_{i,K}}a_{z_{I,k}} + a_{x_{i+1,K}}a_{x_{I,k}} + a_{z_{i+1,K}}a_{z_{I,k}})}{4V_{I,K}V_{I,K-1}} \end{aligned} \quad (\text{B.59})$$

$$\begin{aligned} \vec{\nabla} \zeta_{i,K} \cdot \vec{a}_{i,K} = & \left[\frac{V_{I,K}(\vec{a}_{I-1,k} + \vec{a}_{I-1,k+1}) + V_{I-1,K}(\vec{a}_{I,k} + \vec{a}_{I,k+1})}{4V_{I,K}V_{I-1,K}} \right] \cdot \vec{a}_{i,K} = \\ & \frac{V_{I,K}(a_{x_{I-1,k}}a_{x_{i,K}} + a_{z_{I-1,k}}a_{z_{i,K}} + a_{x_{I-1,k+1}}a_{x_{i,K}} + a_{z_{I-1,k+1}}a_{z_{i,K}})}{4V_{I,K}V_{I-1,K}} \\ & + \frac{V_{I-1,K}(a_{x_{I,k}}a_{x_{i,K}} + a_{z_{I,k}}a_{z_{i,K}} + a_{x_{I,k+1}}a_{x_{i,K}} + a_{z_{I,k+1}}a_{z_{i,K}})}{4V_{I,K}V_{I-1,K}} \end{aligned} \quad (\text{B.60})$$

$$\begin{aligned} \vec{\nabla} \zeta_{I,k} \cdot \vec{a}_{I,k} = & \left[\frac{V_{I,K}(\vec{a}_{I,k-1} + \vec{a}_{I,k}) + V_{I,K-1}(\vec{a}_{I,k} + \vec{a}_{I,k+1})}{4V_{I,K}V_{I,K-1}} \right] \cdot \vec{a}_{I,k} = \\ & \frac{V_{I,K}(a_{x_{I,k-1}}a_{x_{I,k}} + a_{z_{I,k-1}}a_{z_{I,k}} + a_{x_{I,k}}a_{x_{I,k}} + a_{z_{I,k}}a_{z_{I,k}})}{4V_{I,K}V_{I,K-1}} \\ & + \frac{V_{I,K-1}(a_{x_{I,k}}a_{x_{I,k}} + a_{z_{I,k}}a_{z_{I,k}} + a_{x_{I,k+1}}a_{x_{I,k}} + a_{z_{I,k+1}}a_{z_{I,k}})}{4V_{I,K}V_{I,K-1}} \end{aligned} \quad (\text{B.61})$$

Equation B.48 is a matrix equation for the unknowns $\nu_{I,K}$ of the general form $A\vec{x} = \vec{b}$. The matrix A and the vector b are functions only of the geometry and the absorption and emission coefficients. The numerical solution of this type of equation can be obtained by a number of methods, including direct inversion of the matrix, and various relaxation methods such as point Jacobi, point Gauss-Seidel, line Jacobi or line Gauss-Seidel algorithms. The line Gauss-Seidel algorithm has been selected and applied along each normal grid line to capture the dominant gradients in the radiative properties. In this approach, all the ν terms along the I grid line are at the $n + 1$ time level, while all $I + 1$ terms are at the n time level. Terms with $I - 1$ are known at time level $n + 1$ from the solution of the previous line. The d coefficients, as mentioned above, are functions only of the geometry and the absorption coefficient. Since both these quantities are constant for a given transport solution, the d coefficients need only be calculated once.

The line Gauss-Seidel algorithm results in a tridiagonal matrix equation to be

solved for each normal grid line. The solution of such an equation can easily be obtained using the Thomas algorithm [100] with specification of appropriate boundary conditions as discussed below. To ensure convergence for this problem, which is a nonlinear, elliptic equation, underrelaxation is recommended. In fact it is found to be necessary in this application. It is introduced by defining a corrected value for the update of ν as

$$\nu_{I,K}^{n+1'} = \nu_{I,K}^n + r(\nu_{I,K}^{n+1} - \nu_{I,K}^n) = (1-r)\nu_{I,K}^n + r\nu_{I,K}^{n+1} \quad (\text{B.62})$$

where r is the relaxation parameter and is less than one for underrelaxation. The expression for $\nu_{I,K}^{n+1}$ is obtained by solving Eq. B.48. Incorporating this expression in Eq. B.62 and rearranging to the line Gauss-Seidel form results in

$$\begin{aligned} d_6 \frac{r}{d_5} \nu_{I,K-1}^{n+1} + \nu_{I,K}^{n+1'} + d_4 \frac{r}{d_5} \nu_{I,K+1}^{n+1} = (1-r)\nu_{I,K}^n - \frac{r}{d_5} \left(d_1 \nu_{I+1,K+1}^n + d_2 \nu_{I+1,K}^n \right. \\ \left. + d_3 \nu_{I+1,K-1}^n + d_7 \nu_{I-1,K+1}^{n+1} + d_8 \nu_{I-1,K}^{n+1} + d_9 \nu_{I-1,K-1}^{n+1} + 12\pi V_{I,K} \frac{j_{\nu_{I,K}}^e}{j_\nu} \right) \end{aligned} \quad (\text{B.63})$$

The selection of r is discussed in Sec. B.3 below.

B.2 Boundary Conditions

Figure B.2 shows the essential features of the radiation grid. Properties at any interior point (denoted by filled circles) can be obtained by the solution of Eq. B.63 above. The unfilled circles at the left represent “ghost” points for the symmetry boundary condition at the axis of symmetry. Symmetry boundary conditions also exist in and out of the page on the “pie slice” sides (see Fig. B.3), but these are

implicit in the axisymmetric formulation. The triangles along the upper edge of the grid represent the outermost grid cell which forms the freestream boundary. The downward-pointing triangles along the lower edge at right are “ghost” points for the outflow boundary. Finally, the barely visible unfilled squares along the lower edge of the grid represent the center of the surface elements. Each of these boundaries is discussed separately below.

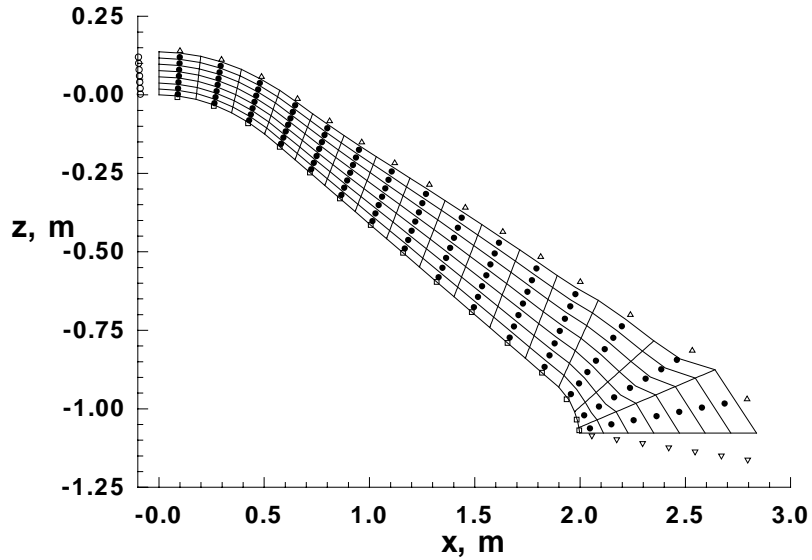


Figure B.2. Essential Features of Axisymmetric Radiation Grid

B.2.1 Axis of Symmetry Boundary

This is a symmetry boundary, at which reflection boundary conditions should apply. Therefore for the unfilled circles in Fig. B.2 along this boundary:

$$,_{\nu}(\text{ghost}, K) = ,_{\nu}(1, K) \quad (\text{B.64})$$

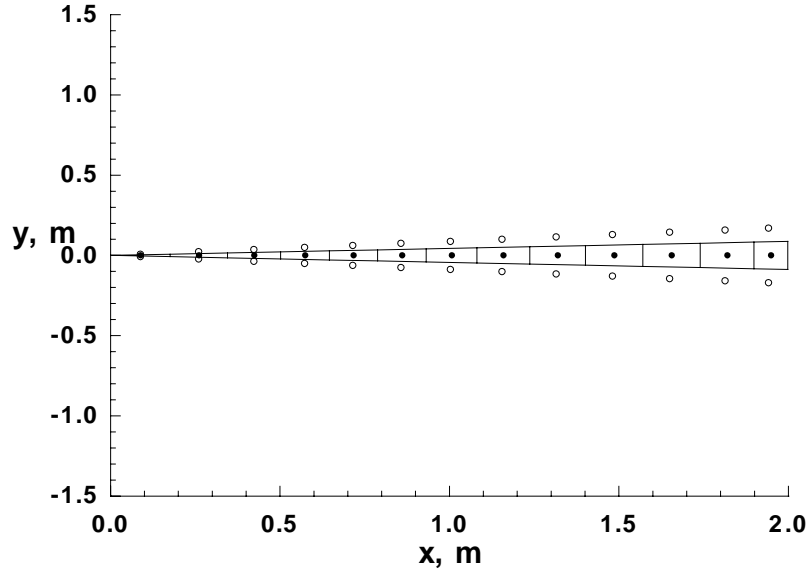


Figure B.3. Top View of Axisymmetric Radiation Grid

This boundary is a singularity in the computational grid, however, where one surface of a grid cell has zero area. Referring back to Eq. B.37, this means the term on the second line disappears. The two remaining ξ -derivative terms at the I grid line are replaced by first order backward differences to avoid differencing across the singularity[92]. Then

$$\frac{\partial, \nu}{\partial \xi}_{I,k+1} = \frac{1}{2} \left(, \nu_{I+1,K+1} - , \nu_{I,K+1} + , \nu_{I+1,K} - , \nu_{I,K} \right) \quad (\text{B.65})$$

$$\frac{\partial, \nu}{\partial \xi}_{I,k} = \frac{1}{2} \left(, \nu_{I+1,K} - , \nu_{I,K} + , \nu_{I+1,K-1} - , \nu_{I,K-1} \right) \quad (\text{B.66})$$

Substituting, Eq. B.47 becomes

$$\begin{aligned} & \frac{\bar{\kappa}_\nu}{\kappa'_{\nu_{i+1,K}}} \left[\vec{\nabla} \xi_{i+1,K} (, \nu_{I+1,K} - , \nu_{I,K}) \right. \\ & \left. + \vec{\nabla} \zeta_{i+1,K} \frac{1}{2} \left(\frac{ , \nu_{I+1,K+1} - , \nu_{I+1,K-1} }{2} + \frac{ , \nu_{I,K+1} - , \nu_{I,K-1} }{2} \right) \right] \cdot \vec{a}_{i+1,K} \end{aligned}$$

$$\begin{aligned}
& + \frac{\bar{\kappa}_\nu}{\kappa'_{\nu_{I,k+1}}} \left[\vec{\nabla} \xi_{I,k+1} \frac{1}{2} \left(\nu_{I+1,K+1} - , \nu_{I,K+1} + , \nu_{I+1,K} - , \nu_{I,K} \right) \right. \\
& \quad \left. + \vec{\nabla} \zeta_{I,k+1} (\nu_{I,K+1} - , \nu_{I,K}) \right] \cdot \vec{a}_{I,k+1} \\
& - \frac{\bar{\kappa}_\nu}{\kappa'_{\nu_{I,k}}} \left[\vec{\nabla} \xi_{I,k} \frac{1}{2} \left(\nu_{I+1,K} - , \nu_{I,K} + , \nu_{I+1,K-1} - , \nu_{I,K-1} \right) \right. \\
& \quad \left. + \vec{\nabla} \zeta_{I,k} (\nu_{I,K} - , \nu_{I,K-1}) \right] \cdot \vec{a}_{I,k} = V_{I,K} \left(3\bar{\kappa}_\nu \kappa'_{\nu} - 12\pi \frac{j_\nu^e}{j_\nu} \right)_{I,K} \quad (B.67)
\end{aligned}$$

Carrying out the dot products and collecting terms as before allows this equation to be put in the form of Eq. B.48, with

$$d_1 = \frac{1}{4} \frac{\bar{\kappa}_\nu}{\kappa'_{\nu_{i+1,K}}} \vec{\nabla} \zeta_{i+1,K} \cdot \vec{a}_{i+1,K} + \frac{1}{2} \frac{\bar{\kappa}_\nu}{\kappa'_{\nu_{I,k+1}}} \vec{\nabla} \xi_{I,k+1} \cdot \vec{a}_{I,k+1} \quad (B.68)$$

$$d_2 = \frac{\bar{\kappa}_\nu}{\kappa'_{\nu_{i+1,K}}} \vec{\nabla} \xi_{i+1,K} \cdot \vec{a}_{i+1,K} + \frac{1}{2} \frac{\bar{\kappa}_\nu}{\kappa'_{\nu_{I,k+1}}} \vec{\nabla} \xi_{I,k+1} \cdot \vec{a}_{I,k+1} - \frac{1}{2} \frac{\bar{\kappa}_\nu}{\kappa'_{\nu_{I,k}}} \vec{\nabla} \xi_{I,k} \cdot \vec{a}_{I,k} \quad (B.69)$$

$$d_3 = -\frac{1}{4} \frac{\bar{\kappa}_\nu}{\kappa'_{\nu_{i+1,K}}} \vec{\nabla} \zeta_{i+1,K} \cdot \vec{a}_{i+1,K} - \frac{1}{2} \frac{\bar{\kappa}_\nu}{\kappa'_{\nu_{I,k}}} \vec{\nabla} \xi_{I,k} \cdot \vec{a}_{I,k} \quad (B.70)$$

$$\begin{aligned}
d_4 = & \frac{1}{4} \frac{\bar{\kappa}_\nu}{\kappa'_{\nu_{i+1,K}}} \vec{\nabla} \zeta_{i+1,K} \cdot \vec{a}_{i+1,K} - \frac{1}{2} \frac{\bar{\kappa}_\nu}{\kappa'_{\nu_{I,k+1}}} \vec{\nabla} \zeta_{I,k+1} \cdot \vec{a}_{I,k+1} \\
& + \frac{\bar{\kappa}_\nu}{\kappa'_{\nu_{I,k+1}}} \vec{\nabla} \zeta_{I,k+1} \cdot \vec{a}_{I,k+1} \quad (B.71)
\end{aligned}$$

$$\begin{aligned}
d_5 = & -\frac{\bar{\kappa}_\nu}{\kappa'_{\nu_{i+1,K}}} \vec{\nabla} \xi_{i+1,K} \cdot \vec{a}_{i+1,K} - \frac{1}{2} \frac{\bar{\kappa}_\nu}{\kappa'_{\nu_{I,k+1}}} \vec{\nabla} \xi_{I,k+1} \cdot \vec{a}_{I,k+1} \\
& - \frac{\bar{\kappa}_\nu}{\kappa'_{\nu_{I,k+1}}} \vec{\nabla} \zeta_{I,k+1} \cdot \vec{a}_{I,k+1} + \frac{1}{2} \frac{\bar{\kappa}_\nu}{\kappa'_{\nu_{I,k}}} \vec{\nabla} \xi_{I,k} \cdot \vec{a}_{I,k} - \frac{\bar{\kappa}_\nu}{\kappa'_{\nu_{I,k}}} \vec{\nabla} \zeta_{I,k} \cdot \vec{a}_{I,k} \\
& - 3V_{I,K} \bar{\kappa}_\nu \kappa'_{\nu_{I,K}} \quad (B.72)
\end{aligned}$$

$$d_6 = -\frac{1}{4} \frac{\bar{\kappa}_\nu}{\kappa'_{\nu_{i+1,K}}} \vec{\nabla} \zeta_{i+1,K} \cdot \vec{a}_{i+1,K} + \frac{1}{2} \frac{\bar{\kappa}_\nu}{\kappa'_{\nu_{I,k}}} \vec{\nabla} \xi_{I,k} \cdot \vec{a}_{I,k} + \frac{\bar{\kappa}_\nu}{\kappa'_{\nu_{I,k}}} \vec{\nabla} \zeta_{I,k} \cdot \vec{a}_{I,k} \quad (B.73)$$

$$d_7 = 0 \quad (\text{B.74})$$

$$d_8 = 0 \quad (\text{B.75})$$

$$d_9 = 0 \quad (\text{B.76})$$

With the appropriate values of d_i along this boundary, then, it can be solved with the same method as the interior points.

B.2.2 Freestream Boundary

The freestream “boundary” is transparent to radiation, and only outgoing radiation is considered. The freestream is assumed to be non-emitting. With these assumptions, this boundary can be approximated as a cold wall with complete absorption ($\varepsilon_\nu = 1.0$). The modified differential approximation is essentially a P-1 method, for which cold wall boundary conditions can be obtained analytically. Modest suggests the use of Marshak’s boundary condition, which is

$$-2 \left[\frac{2}{\varepsilon_\nu} - 1 \right] \vec{q}_\nu \cdot \hat{n} + G_\nu = 0 \quad (\text{B.77})$$

where ε_ν is the spectral surface emissivity, and \hat{n} is the outward unit normal vector describing this boundary surface. Replacing \vec{q}_ν in this equation using Eq. B.2 leads to an equation containing only the one variable G_ν :

$$2 \left[\frac{2}{\varepsilon_\nu} - 1 \right] \frac{\vec{\nabla} G_\nu}{3\kappa'_\nu} \cdot \hat{n} + G_\nu = 0 \quad (\text{B.78})$$

Then dividing by $(\vec{j}_\nu \kappa_\nu)$ to obtain an equation for $,_\nu$ finally gives

$$2 \left[\frac{2}{\varepsilon_\nu} - 1 \right] \frac{\vec{\nabla},_\nu}{3\kappa'_\nu} \cdot \hat{n} + ,_\nu = 0 \quad (\text{B.79})$$

Expanding the gradient of ϵ_ν gives:

$$\frac{2}{3\kappa'_\nu} \left(\frac{2}{\epsilon_\nu} - 1 \right) \left[\vec{\nabla} \xi \cdot \hat{n} \frac{\partial \epsilon_\nu}{\partial \xi} + \vec{\nabla} \zeta \cdot \hat{n} \frac{\partial \epsilon_\nu}{\partial \zeta} \right] + \epsilon_\nu = 0 \quad (\text{B.80})$$

This can be differenced by expressing the derivatives of ϵ_ν using a central difference for the ξ -direction and a first-order backward difference for the ζ -direction. Denoting the freestream boundary grid cell by the subscript F , the result is

$$\frac{2}{3\kappa'_{\nu_{I,F}}} \left[\vec{\nabla} \xi_{I,F} \cdot \hat{n}_{I,F} \frac{\epsilon_{\nu_{I+1,F}} - \epsilon_{\nu_{I-1,F}}}{2} + \vec{\nabla} \zeta_{I,F} \cdot \hat{n}_{I,F} \left(\epsilon_{\nu_{I,F}} - \epsilon_{\nu_{I,F-1}} \right) \right] + \epsilon_{\nu_{I,F}} = 0 \quad (\text{B.81})$$

where the emissivity for the freestream boundary was set to 1.0 as mentioned above. Collecting terms and arranging them in the line Gauss-Seidel form, with the addition of underrelaxation, gives

$$\begin{aligned} & -2r \vec{\nabla} \zeta_{I,F} \cdot \hat{n}_{I,F} \epsilon_{\nu_{I,F-1}}^{n+1} + \left(2 \vec{\nabla} \zeta_{I,F} \cdot \hat{n}_{I,F} + 3\kappa'_{\nu_{I,F}} \right) \epsilon_{\nu_{I,F}}^{n+1} = \\ & \left(2 \vec{\nabla} \zeta_{I,F} \cdot \hat{n}_{I,F} + 3\kappa'_{\nu_{I,F}} \right) (1-r) \epsilon_{\nu_{I,F}}^n - r \vec{\nabla} \xi_{I,F} \cdot \hat{n}_{I,F} \left(\epsilon_{\nu_{I+1,F}}^n - \epsilon_{\nu_{I-1,F}}^{n+1} \right) \end{aligned} \quad (\text{B.82})$$

The dot product terms calculated in Eqs. B.59 and B.61 are at cell faces. To obtain the values at the cell center required in the above expression, an average at the two opposing faces of the cell is taken. Then

$$\vec{\nabla} \xi_{I,F} \cdot \hat{n}_{I,F} = \frac{\vec{\nabla} \xi_{I,f+1} \cdot \hat{n}_{I,f+1} + \vec{\nabla} \xi_{I,f} \cdot \hat{n}_{I,f} + \vec{\nabla} \xi_{I+1,f+1} \cdot \hat{n}_{I+1,f+1} + \vec{\nabla} \xi_{I+1,f} \cdot \hat{n}_{I+1,f}}{4} \quad (\text{B.83})$$

$$\vec{\nabla} \zeta_{I,F} \cdot \hat{n}_{I,F} = \frac{\vec{\nabla} \zeta_{I,f+1} \cdot \hat{n}_{I,f+1} + \vec{\nabla} \zeta_{I,f} \cdot \hat{n}_{I,f} + \vec{\nabla} \zeta_{I+1,f+1} \cdot \hat{n}_{I+1,f+1} + \vec{\nabla} \zeta_{I+1,f} \cdot \hat{n}_{I+1,f}}{4} \quad (\text{B.84})$$

where the subscript $f + 1$ denotes the freestream cell face.

For the freestream boundary at the axis of symmetry, the reflection boundary condition Eq. B.64 for $,_{\nu_{I-1,F}}$ is used. Using a first order backward difference at this point was found to lead to nonphysical results.

B.2.3 Outflow Boundary

Along the outflow “boundary”, $,_{\nu_{I+1,K}}$ in Eq. B.47 represents the “ghost” point and must be approximated. This is an arbitrary computational boundary through which radiating gas and radiation (inwardly and outwardly directed) both pass. The flowfield boundary condition used in LAURA is a zeroth order extrapolation (i.e., the derivatives of the flow variables are assumed to be zero across this boundary). This boundary condition is known to provide better stability than other possible formulations, and so can also be adopted for the radiation method. Therefore,

$$,_{\nu}(I + 1, K) \approx ,_{\nu}(I, K) \quad (\text{B.85})$$

One alternative possibility is to assume a constant slope at this boundary. To perform an extrapolation of the positive-definite variable $,_{\nu}$, a logarithmic extrapolation is indicated¹

$$,_{\nu}(I + 1, K) \approx \frac{,_{\nu}^2(I, K)}{,_{\nu}(I - 1, K)} \quad (\text{B.86})$$

This boundary condition was found to work well in some cases and to cause $,_{\nu}(I, K)$ to blow up in the shoulder region in others. This undesirable behavior results from

¹Suggested by Gnoffo

inaccuracies and lack of grid resolution near the shoulder of the body in the test cases. Logic was implemented to apply the logarithmic boundary condition except in cases where it would result in an increasing value of $\nu(I, K)$ around the shoulder. Those instances are treated with the zeroth order boundary condition to prevent the solution from blowing up. Even when the solution does blow up at the shoulder, much of the rest of the flowfield remains quite unaffected. This suggests that the solution method is robust.

B.2.4 Wall Boundary

For the medium only intensity, this boundary appears as a cold wall. The Marshak boundary condition (Eq. B.79) can be differenced at this boundary by recognizing that the grid lines are normal to the body surface (Fig. B.2 is not to scale). The term $\vec{\nabla} \nu \cdot \hat{n}$ is then simply the gradient of ν along the grid lines. This difference is best expressed in physical coordinates with a first order forward scheme as

$$\frac{\nu_{I,1} - \nu_{I,w}}{\Delta r} - \frac{3\kappa'_{\nu_{I,1}}}{2} \left(\frac{\varepsilon_{\nu_I}}{2 - \varepsilon_{\nu_I}} \right) \nu_{I,w} = 0 \quad (\text{B.87})$$

where the subscript w denotes a “ghost” point on the surface of the body, and

$$\Delta r = \sqrt{(x(I, 1) - x(I, w))^2 + (z(I, 1) - z(I, w))^2} \quad (\text{B.88})$$

In the Gauss-Seidel format, with the incorporation of underrelaxation, this becomes

$$\left[\frac{1}{\Delta r} + \frac{3\kappa'_{\nu_{I,1}}}{2} \left(\frac{\varepsilon_{\nu_I}}{2 - \varepsilon_{\nu_I}} \right) \right] \nu_{I,w}^{n+1'} - r \frac{1}{\Delta r} \nu_{I,1}^{n+1} = (1 - r) \left[\frac{1}{\Delta r} + \frac{3\kappa'_{\nu_{I,1}}}{2} \left(\frac{\varepsilon_{\nu_I}}{2 - \varepsilon_{\nu_I}} \right) \right] \nu_{I,w}^n \quad (\text{B.89})$$

B.2.5 Radiative Heat Flux to Wall

The radiative flux directed to the wall due to emission in the medium can then be found from solving Eq. B.2.

$$\vec{q}_\nu = \frac{-1}{3\kappa'_\nu} \vec{\nabla} G_\nu \quad (\text{B.90})$$

In this equation, G_ν is obtained from the solution of the finite volume problem, j_ν , multiplied by the normalizing factor $(\bar{j}_\nu \bar{\kappa}_\nu)$. To obtain the flux directed at the wall, the dot product of \vec{q}_ν with the wall-directed surface normal is required. Then

$$q_{w_\nu} = -\vec{q}_\nu \cdot \hat{n}_w = \frac{1}{3\kappa'_\nu} \vec{\nabla} G_\nu \cdot \hat{n}_w \quad (\text{B.91})$$

Again recalling that the grid lines are normal to the body surface, the gradient of G_ν can be expressed with a one-sided difference along the normal grid lines. As above, this is best done in physical coordinates.

$$q_{\nu_w} = \frac{1}{3\kappa'_\nu} \frac{G_{\nu_{I,2}} - G_{\nu_{I,1}}}{\Delta r} \quad (\text{B.92})$$

Alternately, a second order forward difference could be used to represent the gradient. The total heat flux to the wall at each grid location is then obtained by a numerical integration over the spectral result above. This closes the numerical problem.

B.3 Numerics and Convergence

B.3.1 Convergence Criterion

The numerical solution of this set of difference equations requires the selection of an appropriate criterion to test for convergence. Because the radiative properties vary

over many orders of magnitude, and because the grid introduces numerical errors, the usual definition of the L_2 norm for this purpose is not satisfactory. Instead, a local error function is defined:

$$L_{I,K} = \frac{|\nu_{I,K}^{n+1} - \nu_{I,K}^n|}{\text{mean}(\nu^n)} \quad (\text{B.93})$$

where the mean of ν^n is obtained as the average of the minimum and maximum values of $\nu_{I,K}^n$ for all I and K on the radiation grid. This definition reduces the value of $L_{I,K}$ in regions where $\nu_{I,K}^n$ is small, relative to the error that would be obtained from the L_2 norm. The result is that convergence is reached faster. Though convergence may not be entirely complete at those locations where $\nu_{I,K}^n$ is small, these locations contribute little to the coupling with the flowfield. Therefore, the lack of complete convergence at these locations is deemed acceptable to reduce the computation time.

The actual convergence is determined by the average value of $L_{I,K}$ over the radiation grid. When this average is less than some specified value, convergence is assumed to have been reached for that particular frequency ν . Each frequency is converged individually, since the rate of convergence depends on the magnitude of the optical depth and varies considerably with frequency. A typical convergence history for a single frequency is shown in Fig. B.4. Convergence may be faster or slower for the individual frequencies, depending at least partly on the magnitude of the optical depth at that frequency.

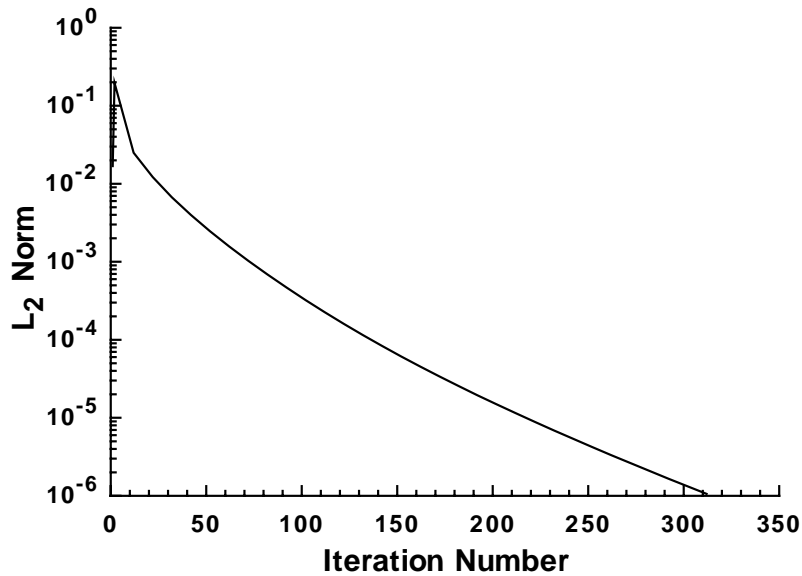


Figure B.4. Typical Convergence History for MDA Solution

B.3.2 Selection of Relaxation Parameter

The relaxation parameter required to obtain a stable solution varies with the magnitude of the optical depth of the flowfield. Very fast convergence can be obtained for optically thick spectral regions using $r=1$, meaning no underrelaxation. For optically thin regions on the other hand, the solution with $r=1$ is unstable. The value $r=0.5$ has been selected as a good compromise. In future, an algorithm might be developed to vary the underrelaxation parameter r as a function of the radiation properties in order to further accelerate the convergence of the complete transport solution.